이학박사 학위논문

Spin dynamics of Kitaev candidates in cobalt compounds

코발트 화합물에서 키타에프 후보군의 스핀 동역학

2023 년 8 월

서울대학교 대학원

물리천문학부 물리학전공

김 채 빈

Spin dynamics of Kitaev candidates in cobalt compounds

Chaebin Kim

Supervised by
Professor Je-Geun Park

A Dissertation submitted to the Faculty of Seoul National University in Partial Fulfillment of the Requirements for the Degree of Doctor of Philosophy
August 2023

Department of Physics and Astronomy
Graduate School
Seoul National University

Spin dynamics of Kitaev candidates in cobalt compounds

코발트 화합물에서 키타에프 후보군의 스핀 동역학

지도 교수 박 제 근

이 논문을 이학박사 학위논문으로 제출함
2023 년 8 월

서울대학교 대학원
물리천문학부
김 채 빈

김채빈의 이학박사 학위논문을 인준함
2023 년 6 월

위 원 장	박 철 환	(인)
부위원장	박 제 근	(인)
위 원	최 석 봉	(인)
위 원	민 홍 기	(인)
위 원	Martin Mourigal	(인)

Abstract

One of the ambitions in condensed matter physics is to discover new material with a quantum phase, which properties are governed by quantum fluctuations and entanglement. The quantum spin liquid (QSL) is one of such exotic phases because of the absence of magnetic order and hosting long-range entanglement between spins. Among the many theoretical models proposed so far, the Kitaev model is probably the best to realize QSL in real material. The reason is that it can be precisely solvable and theoretically proposed to realize in real material with relatively simple conditions.

To realize the Kitaev model in real compounds, we need two ingredients, spin-orbital entangled $J_{\mathrm{eff}} = 1/2$ state and an edge-sharing network of octahedrons. The entanglement between spin and orbital degree of freedom makes the exchange anisotropic and bond-dependent. Obviously, present studies about the Kitaev model have been based on the 4*d* and 5*d* transition metals because they have strong spin-orbit coupling. However, there were some limitations in 4*d* and 5*d* compounds, such as the lack of enough candidates and the existence of long-range magnetic order. Therefore, we need to investigate other possible candidates for realizing the Kitaev model in real materials. Recent theories suggest that 3d transition metals, such as cobalt, can also host $J_{\mathrm{eff}} = 1/2$ state despite small spin-orbit coupling.

In my dissertation, I studied the spin dynamics of cobalt Kitaev candidates with two different lattices, honeycomb and triangular, using inelastic neutron scattering (INS). First, I examined the evidence of spin-orbital entangled states in the three cobalt honeycomb compounds, $CoPS_3$, $Na_2Co_2TeO_6$ (NCTO), and $Na_3Co_2SbO_6$ (NCSO). Temperature dependence of magnetic excitations shows no signature of $J_{\mathrm{eff}} = 1/2$ state in the $CoPS_3$. However, the spin-orbit exciton, which certificates the spin-orbit entangled state, was observed in other honeycomb compounds NCTO and NCSO. The absence of spin-orbital entangled $J_{\mathrm{eff}} = 1/2$ state indicates $CoPS_3$ can be described by rather a simple spin $S = 3/2$ state and cannot have Kitaev-like bond-dependent anisotropy. Based on this observation, the spin-wave spectrum of $CoPS_3$ was analyzed by XXZ-like Hamiltonian with easy-axis single-ion anisotropy. The XXZ model with anisotropy factor $J_x/J_z = 0.6$ is the best ratio to explain the observed spectrum.

In the case of NCTO and NCSO, the spin-wave spectrum was analyzed based on two different Hamiltonian, XXZ model, and generalized Kitaev-Heisenberg model. Both compounds were well-explained by strong Kitaev interaction and other non-Kitaev interactions. One important feature is that the sign of the Kitaev term was positive, which was not discovered in present Kitaev candidates. Further magnetic phase diagram and two-magnon density-of-states were calculated to examine these Kitaev candidates comprehensively.

Second, I extended the idea of the Kitaev model to the triangular lattice, which gives geometrical frustration. The magnetic van der Waals cobalt triangular antiferromagnet CoI_2 fulfilled this condition. Using the Luttinger-Tisza method, we put forward two potential minimal models to unveil the magnetic structure of CoI_2. One of these models includes a Kitaev term, while the other omits it. Through INS measurements conducted during the paramagnetic phase, we confirmed that the minimal model incorporating bond-dependent anisotropy explains the characteristics of CoI_2. During the ordered phase, the observed spin-wave spectrum displayed significant linewidth broadening at the borad momentum space, suggesting magnon decay. To delve deeper into this decay process, we conducted an analysis utilizing the density of states for two-magnon interactions.

Keywords: quantum magnetism, spin-orbital entangled state, Kitaev model, inelastic neutron scattering, magnon decay

Student Number: 2018-28059

List of Tables

List of Figures

Chapter 1
Introduction

1.1 Kitaev model and Jackeli–Khaliullin mechanism

1.1.1 Kitaev model

Realizing quantum phases of matter, which stabilized from the quantum fluctuations and long-range entanglement, has become an important topic in condensed matter physics. One example is a quantum spin liquid (QSL), which has no magnetic order but exhibits long-range entanglement [Ref. 1.1]. The concept of realizing QSL was first suggested by P. Anderson based on a spin S = 1/2 system on a triangular lattice with isotropic antiferromagnetic interactions (see Fig. 1.1(a)) [Ref. 1.2]. The competition between the interactions of the two nearest bonds results in spin frustration because of geometry. Anderson suggests that the ground state of this system is the superposition of spin singlets and is called a resonant valence bond state [Ref. 1.2]. Although numerical calculations reveal that the ground state has a non-collinear 120° magnetic order, this concept was still examined in different geometrically frustrated lattices, such as kagome lattices or a triangular lattice with further interactions.

Despite tremendous progress and inputs, finding such quantum phases is still challenging because there is no exact solution for realizing such a state in any realistic model

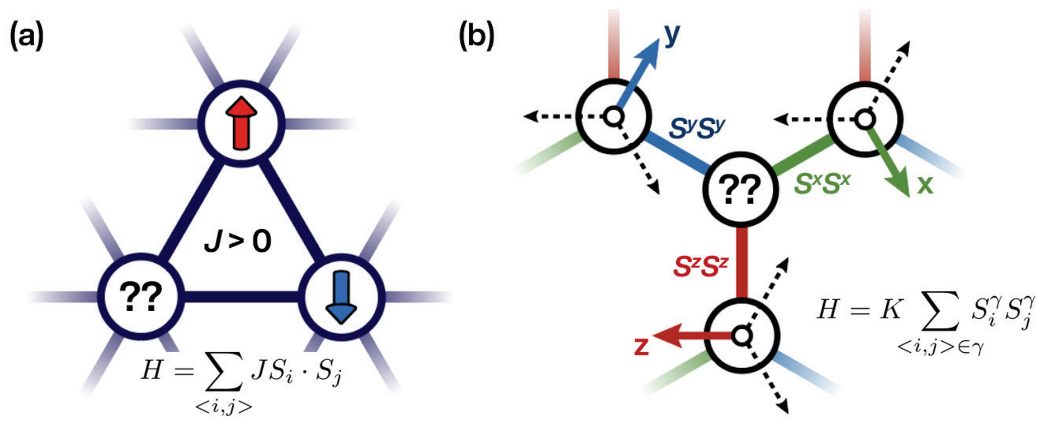

Figure 1.1 Schematic showing comparison between (a) geometric frustration and (b) Kitaev model.

Hamiltonian. However, Kitaev reported a significant breakthrough in 2006 by suggesting a simple model, namely the Kitaev model [Ref. 1.3], which is a spin $S = 1/2$ system on a honeycomb lattice that can be exactly solved with a QSL ground state. The Hamiltonian of the Kitaev model can be expressed as follows:

$$H = K \sum_{<ij>\in\alpha} S_i^\alpha S_j^\alpha, \tag{1.1}$$

where index α = x, y, z denotes the three nearest-neighbour bonding types in a honeycomb lattice (see Fig. 1.1(b)). Because the Ising axes of each nearest-neighbour bond are mutually orthogonal, the frustration of spins is observed. The QSL state of the Kitaev model can be understood as a quantum-mechanical superposition of an infinite number of classical spin configurations [Ref. 1.3,1.4]. Each classical spin configuration consists of one 'happy' pair and two 'unhappy' pairs; here 'happy' indicates that the two nearest neighbours align with the same Ising axis (see Fig. 1.2(b)). The Kitaev QSL state is distinguished by a local conserved quantity called the Z_2 flux operator $W = 2^6 S_1^z S_2^x S_3^y S_4^z S_5^x S_6^y$, around each honeycomb lattice with eigenvalues of ±1. The Kitaev model provides a unique route to

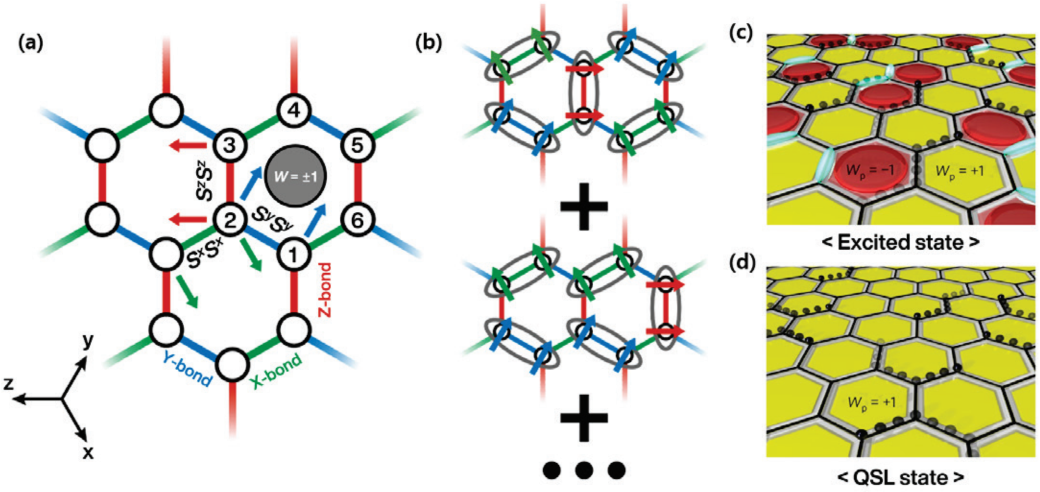

Figure 1.2 Schematic of the Kitaev model. (a) Illustration of bond-dependent anisotropic interactions in the Kitaev model and Z_2 flux W. (b) Examples of classical spin configuration of the ground state of the Kitaev model. The grey circle indicates the 'happy' pairs, which minimise the energy from Ktiaev interactions. The Kitaev QSL state is a quantum superposition of these configurations. (c-d) Schematic of the Kitaev model with an excited state and ground state (QSL) adapted from [Ref. 1.8].

realize a QSL state—exchange interactions in the Kitaev model are highly anisotropic Ising interactions, rather than Heisenberg interactions, which most importantly can be exactly solved for any K. The analytical solution of the Kitaev model can be derived by fractionalizing the spin S =1/2 operator into the four flavours of Majorana fermions as follows:

$$S_j^\gamma = \frac{i}{2} b_j^\gamma c_j, \tag{1.2}$$

where b_j^γ and cj are the four Majorana operators that satisfy the relation $b_j^x b_j^y b_j^z c_j = 1$. This constraint equation preserves the spin 1/2 algebra and local two-dimensional Hilbert space. With this fractionalization, we can rewrite the Hamiltonian with the following exact form:

$$H = -\frac{K}{4} \sum_{<i,j>\in\gamma} u_{ij}^{\gamma} c_i c_j, \tag{1.3}$$

where $u_{ij}^{\gamma} = b_i^{\gamma} b_j^{\gamma}$ are the bond operators with eigenvalues ±*I*, and their production around the honeycomb determines the Z_2 flux *W*.

1.1.2 Jackeli–Khaliullin mechanism

When proposed initially, the Kitaev model was considered just as a toy model because this strong Ising anisotropy is challenging to achieve in a pure spin $S = ½$ system. However, it was suggested that the model could be realized in real compounds if they satisfy a few necessary conditions. Jackeli and Khaliullin first microscopically verified Kitaev-like exchange interactions in a natural material, namely the Jackeli–Khaliullin (JK) mechanism [Ref. 1.5]. The first essential condition is a spin-orbital entangled state, which results in a common quantization axis between the spin and the orbital Hilbert space. This entanglement is usually attributed to spin–orbit coupling, and thus, a strong spin–orbit coupling is necessary to stabilize the spin-orbital entangled state [Ref. 1.5]. This condition can be attributed to the form of the Kitaev model because the direction of the spin must be specified based on the crystallographic axes. The JK mechanism requires a pseudospin $j_{\mathrm{eff}} = 1/2$ state, equivalent to a spin $S = 1/2$ doublet, except for its anisotropic spatial distribution. The wave function of the $j_{\mathrm{eff}} = 1/2$ state can be expressed as follows [Ref. 1.5]:

$$\left| j_{eff} = \frac{1}{2},\ j_{eff}^{z} = \pm\frac{1}{2} \right\rangle = \mp\frac{1}{\sqrt{3}}\left(|d_{xy}, \uparrow\downarrow\rangle \pm |d_{yz}, \downarrow\uparrow\rangle + i|d_{xz}, \downarrow\uparrow\rangle\right) \tag{1.4}.$$

where d_{xy}, d_{yz}, and d_{xy} are the three bases in the atomic t_{2g} orbitals. The direction of the spin is coupled with the orbital wave function. Therefore, this orbital dependence of the spin gives rise to anisotropic exchange interactions. The second condition is associated with the crystal structure. When the bonding angle between two ligands and a transition metal

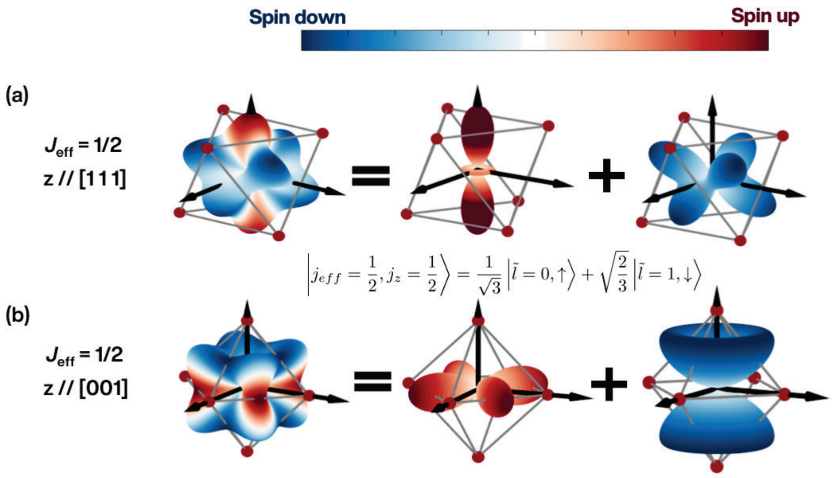

Figure 1.3 Real-space spin configuration of a spin-orbital entangled j_{eff} = 1/2 state with different quantisation axes. (a) z axis parallel to the [1, 1, 1] direction, which is useful for considering trigonal distortions. (b) z axis parallel to the [0, 0, 1] direction.

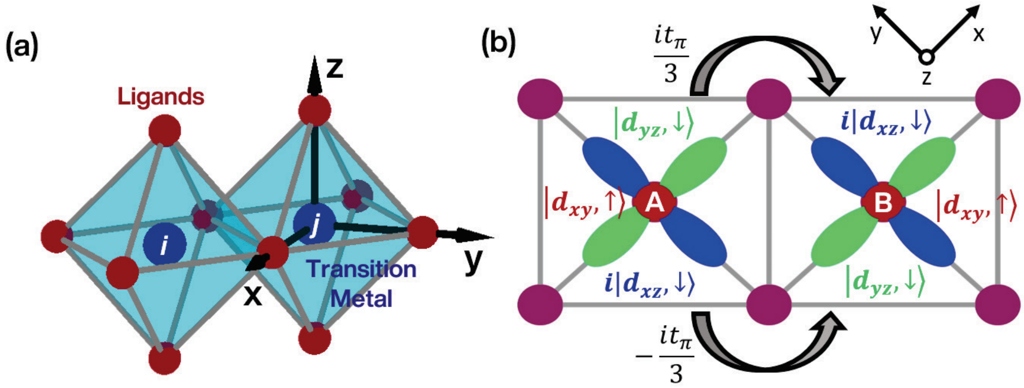

Figure 1.4 (a) Edge-sharing metal–ligand octahedra i and j; the blue and purple spheres depict the transition metal and ligands, respectively. (b) Schematic of destructive interference in an edge-sharing network.

becomes 90° degrees, Heisenberg interactions are eliminated because the two different exchange paths of the Heisenberg interactions destructively interfere (see Fig. 1.4). This type of geometry can be achieved using an edge-sharing network, in which two octahedrons are connected by their specific edges [Ref. 1.5].

1.2 Review of the present Kitaev candidates and their limitations

Based on the JK mechanism, numerous experimental studies have been conducted on Kitaev candidates, including 4*d* and 5*d* transition metal compounds. Ir^{4+} and Ru^{3+} ions satisfy the JK mechanism because they have a low-spin d^5 configuration and exhibit a strong spin–orbit coupling. Indeed, Jackeli and Khaliullin suggest the prototype Na_2IrO_3 as a Kitaev candidate [Ref. 1.5,1.6]. There are several variations of Na_2IrO_3, because the Na^+ ions can be replaced with Li^+ or Cu^+ ions [Ref. 1.4]. α-$RuCl_3$ exhibits the JK mechanism, similar to Na_2IrO_3, which is an ideal platform for exploring Kitaev physics [Ref. 1.7]. Among these candidates, α-$RuCl_3$ shows several distinct physical properties close to those of the Kitaev model. For example, several inelastic scattering measurements reveal the occurrence of fractionalized excitations in α-$RuCl_3$ [Ref. 1.7–1.9]. Moreover, the magnetic order in this material can be suppressed by applying an in-plane magnetic field (7–9 T) [Ref. 1.10]. Because of these exciting behaviours, various authors have extensively studied the field-induced behaviour of RuCl3 over the years. The recently demonstrated thermal Hall effect is a direct signature of half-quantized Kitaev QSL states [Ref. 1.11]. However, the half-quantized thermal Hall effect in α-$RuCl_3$ is still a controversial phenomenon. The recent findings on these Kitaev candidates are summarised in this review article [Ref. 1.4].

Conversely, the present Kitaev candidates exhibit several limitations. First, most of these candidates are magnetically ordered at a finite temperature of a few Kelvin [Ref. 1.4]. This magnetic order originates from non-Kitaev interactions, such as isotropic Heisenberg

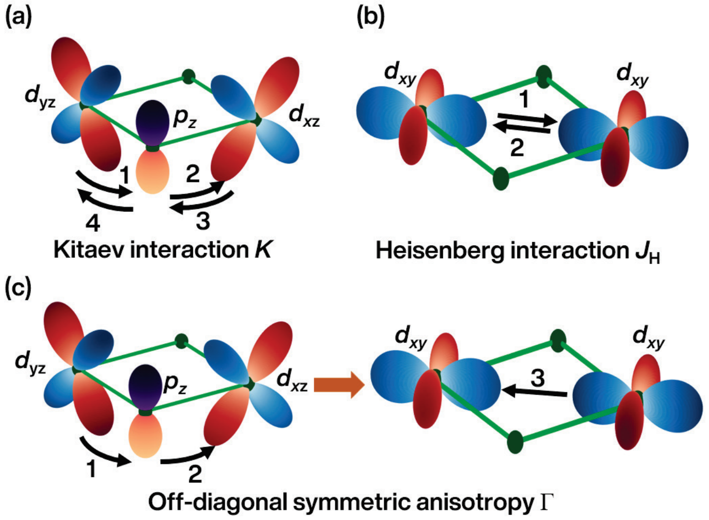

Figure 1.5 Schematic showing the exchange process in the *d*-electron case. (a) Indirect *d*–*p*–*d* hopping, which is considered in the JK mechanism. (b) Direct *d*–*d* hopping, which gives rise to Heisenberg interactions. (c) A mixture of indirect and direct hopping, which leads to an off-diagonal symmetric anisotropy.

interactions (J_H) or symmetrically allowed off-diagonal interactions (Γ). Non-Kitaev interactions are realistic because of two primary reasons. (i) The JK mechanism simplifies the path of the exchange interaction [Ref. 1.5]. Natural materials exhibit super-exchange interactions meditated by ligands and direct exchange interactions due to orbital overlapping [Ref. 1.12,1.13]. This extra exchange path gives rise to finite non-Heisenberg interactions (See Fig. 1.5). (ii) Real materials always have non-cubic distortions, because of which the angle of exchange path deviates from 90º; this deviation minimizes the destructive interference and thus leads to Heisenberg interactions [Ref. 1.13].

The second limitation is the negative sign of Kitaev interactions (i.e. ferromagnetic). In the pure Kitaev model, the sign of the Kitaev interaction does not affect the QSL ground state. Nonetheless, the robustness of the QSL state under an applied magnetic field is different

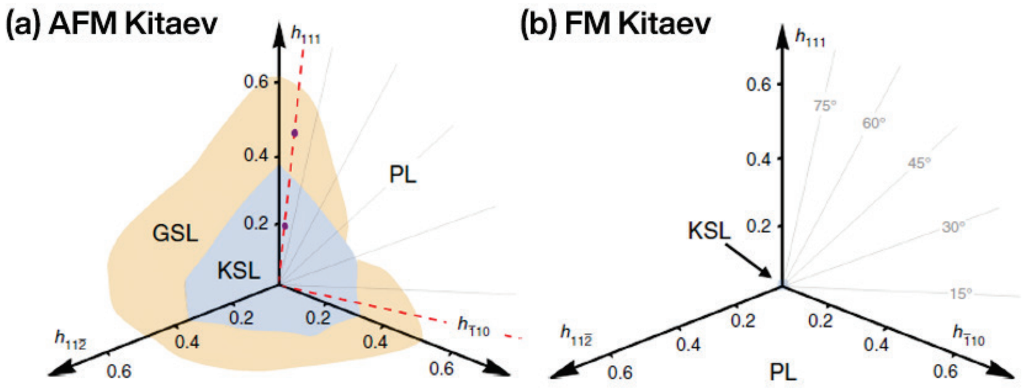

Figure 1.6 Phase diagrams in a unifrom magnetic field with (a) AFM Kitaev model and (b) FM Kitaev model. GSL incidates a gapless spin liquid, KSL is a gapped Kitaev spin liquid, and PL is the polarized state. The figures are adapted from [Ref. 1.14]

according to the sign of Kitaev interaction [Ref. 1.14]. In the case of $K < 0$, the QSL state is only a Z_2 gauge field whose stability can be easily perturbed by applying a magnetic field. In contrast, in the case of $K > 0$, the QSL state is more stable under an applied magnetic field. Moreover, the type of gauge field changes from Z_2 to $U(1)$ symmetry with the increasing magnetic field strength. This observation implies that the antiferromagnetic Kitaev model is a suitable platform for controlling the gaps of the QSL phase using an external variable. Therefore, a new candidate is required to examine real systems that exhibit Kitaev model characteristics through experiments.

1.3 Spin-orbital entangled $J_{\text{eff}} = 1/2$ state in cobalt compounds

After comprehensive studies on iridium and ruthenium-based Kitaev candidates, theorists are now trying to overcome the limitations of these candidates. Several studies have been reported on realising Kitaev interactions in different systems. In 2018, two papers introduced new candidates for realizing Kitaev interactions [Ref. 1.15,1.16]. The new

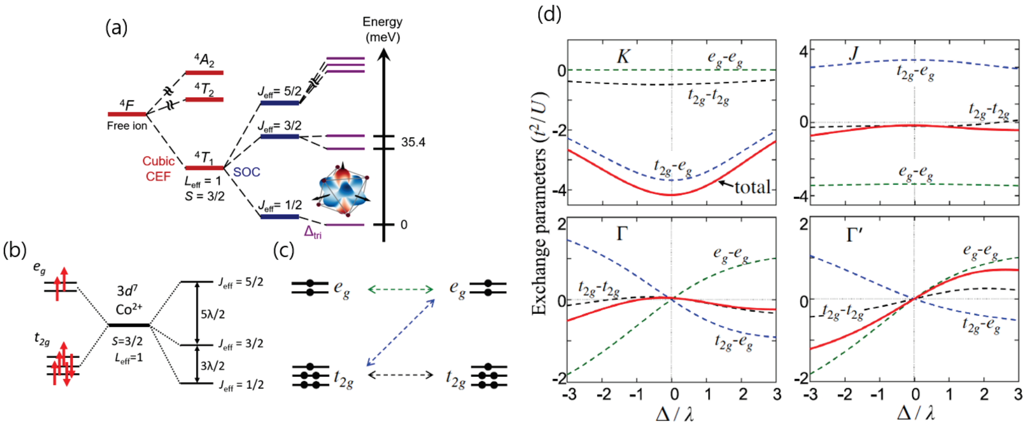

Figure 1.7 Spin-orbital entangled J_{eff} = 1/2 state in cobalt ions and exchange interactions. (a) Schematic of a spin-orbital entangled J_{eff} = 1/2 state in cobalt based on the multiplet basis. (b) Comparison of a single-electron basis (left) and multi-electron basis (right). (c) Possible exchange hopping process in a d^7 high-spin configuration. (d) Exchange parameters for the hopping process adapted from the [Ref. 1.17].

platform is a d^7 high-spin configuration, which can also host a spin-orbital entangled J_{eff} = 1/2 state. Under a cubic crystal electric field, the d^7 configuration has the lowest $^4T_1$ multiplet states with an S = 3/2 high-spin configuration and an unquenched angular momentum L = 1, even for a weak spin–orbit coupling (see Fig. 1.7(a-b)). Therefore, spin–orbit coupling acts on the multiplet states and stabilizes a spin-orbital entangled J_{eff} = 1/2 state. The wavefunction of the lowest J_{eff} = 1/2 state can be expressed based on the multi-electron picture as follows [Ref. 1.15,1.16]:

$$\left|J_{eff} = \pm\frac{1}{2}\right\rangle = \frac{1}{\sqrt{2}}\left|\mp 1, \pm\frac{3}{2}\right\rangle - \frac{1}{\sqrt{3}}\left|0, \pm\frac{1}{2}\right\rangle + \frac{1}{\sqrt{6}}\left|\pm 1, \mp\frac{1}{2}\right\rangle. \qquad (1.5)$$

where the basis is a multiplet state $|L, S\rangle$ (L and S indicate the sum of the orbital and spin states of 7 electrons in the d^7 configuration). This J_{eff} = 1/2 state contains additional spin-active e_g electrons and is thus different from the normal d^5 state. The presence of e_g

electrons opens up new exchange hopping paths, such as e_g–e_g and t_{2g}–e_g. Theoretical calculations indicate that the Heisenberg interaction J_H is eliminated because of the same magnitude and different signs of the t_{2g}–e_g and e_g–e_g hopping interactions (see Fig. 1.7(d)) [Ref. 1.17]. These results prompted investigations on cobalt compounds to realize ideal Kitaev models, whose characteristics are better than those of the previous candidates.

1.4 Outline of thesis

This thesis covers the spin dynamics of cobalt compound-based Kitaev candidates with two different lattices: honeycomb and triangular lattices. This chapter explains the concept of the Kitaev model and its realization in real materials.

Chapter 2 introduces the basic theory of spin-wave calculations using a rotational frame method used in Chapters 4–6. First, a general methodology to calculate spin waves in the non-interacting limit is described. Then, two possibilities of magnon decay in Kitaev-type materials are suggested.

Chapter 3 illustrates the experimental techniques used during the study. This chapter is divided into sample synthesis and inelastic neutron scattering. The sample synthesis section describes the standard solid-state reaction methods for synthesizing polycrystalline samples and the Bridgman method for fabricating single crystals. Next, the basics of the inelastic neutron scattering process and the principle of time-of-flight spectroscopy are introduced. Finally, details of the beamlines and multiple incident energy method are presented.

Chapter 4 verifies the presence of a $J_{\mathrm{eff}} = 1/2$ state in the van der Waals antiferromagnet $CoPS_3$. The temperature dependence of magnetic excitation implies that $CoPS_3$ is far from the spin-orbital entangled $J_{\mathrm{eff}} = 1/2$ state. The spin-wave excitation is analyzed using the XXZ-like Hamiltonian with the spin $S = 3/2$ model. We found that the spin-wave spectrum can be explained by considering a strong XXZ anisotropy factor with $\alpha = J_x/J_z = 0.6$.

Chapter 5 presents the spin dynamics of the cobalt honeycomb materials $Na_2Co_2TeO_6$ and $Na_3Co_2SbO_6$. Using the inelastic neutron scattering technique, we observed a spin–orbit exciton at 20–30 meV in both compounds, and the presence of this exciton indicates the presence of $J_{\mathrm{eff}} = 1/2$ ground states. Spin-wave analysis confirmed that both the compounds have finite Kitaev interactions but different signs ($K > 0$) compared to other reported candidates. We further analyzed the magnetic phase diagrams and performed two-magnon density-of-states (DOS) calculations to explain the magnetic nature of these compounds.

In Chapter 6, we demonstrate the first realization of Kitaev interactions on a triangular lattice with CoI_2. Using the Luttinger–Tisza method, we suggest two possible minimum models for explaining the magnetic structure of CoI_2: one with a Kitaev term and one without a Kitaev term. Inelastic neutron scattering at the paramagnetic phase confirms that the minimal model with a bond-dependent anisotropy can explain the nature of CoI_2. The spin-wave spectrum of the ordered phase shows significant linewidth broadening over the momentum space, indicating magnon decay. We further analyzed this magnon decay process using the two-magnon DOS.

References

[Ref. 1.1] Balents, L., Nature **464**, 199 (2010).

[Ref. 1.2] Anderson, P. W., Mater Res Bull **8**, 153 (1973).

[Ref. 1.3] Kitaev, A., Ann Phys (N Y) **321**, 2 (2006).

[Ref. 1.4] Takagi, H. et al., Nature Reviews Physics **1**, 264 (2019).

[Ref. 1.5] Jackeli, G. and G. Khaliullin, Phys Rev Lett **102**, 017205 (2009).

[Ref. 1.6] Choi, S. K. et al., Phys Rev Lett **108**, 127204 (2012).

[Ref. 1.7] Banerjee, A. et al., Nat Mater **15**, 733 (2016).

[Ref. 1.8] Do, S. H. et al., Nat Phys **13**, 1079 (2017).

[Ref. 1.9] Sandilands, L. J. et al., Phys Rev Lett **114**, 147201 (2015).

[Ref. 1.10] Banerjee, A. et al., NPJ Quantum Mater **3**, 8 (2018).

[Ref. 1.11] Kasahara, Y. et al., Nature **559**, 227 (2018).

[Ref. 1.12] Rau, J. G., E. K. H. Lee, and H. Y. Kee, Phys Rev Lett **112**, 077204 (2014).

[Ref. 1.13] Winter, S. M. et al., Journal of Physics: Condensed Matter **29**, 493002 (2017).

[Ref. 1.14] Hickey, C. and S. Trebst, Nat Commun **10**, 530 (2019).

[Ref. 1.15] Liu, H. and G. Khaliullin, Phys Rev B **97**, 014407 (2018).

[Ref. 1.16] Sano, R., Y. Kato, and Y. Motome, Phys Rev B **97**, 014408 (2018).

[Ref. 1.17] Liu, H., J. Chaloupka, and G. Khaliullin, Phys Rev Lett **125**, 047201 (2020).

Chapter 2
Theoretical background

2.1 General solution for the linear spin-wave theory

Spin wave is the collective excitation in an ordered magnetic structure. Equivalently, we can describe the spin wave in the view of quasiparticles, known as magnon. Since the magnetic Hamiltonian determines all the features of magnetic properties, we can calculate the magnon dispersion using the magnetic Hamiltonian. General spin Hamiltonian with exchange interactions can be written as follows:

$$\hat{H} = \sum_{m,n,i,j} S_{mi} \cdot J_{mi,nj} \cdot S_{nj} \tag{2.1}$$

where m,n are the indices of the unit cell, i, j are the indices of the magnetic moments within the unit cell, and J is the 3 × 3 exchange matrix between S_{mi} and S_{nj}.

2.1.1 Rotating frame method

The standard approach for calculating magnon dispersion with a collinear magnetic structure is to construct a magnetic supercell. In this case, the z-axis of the local coordinates is parallel to the spin polarisation direction. However, this approach cannot be used for an incommensurate magnetic order because it needs a large magnetic supercell for calculations. The rotating frame method can overcome this problem and be generalized in collinear or non-colinear orders [Ref. 2.1]. For example, we can transform lab coordinates to local coordinates via a rotation matrix, which can explain the magnetic structure. The rotating angle depends on the propagation vector of the magnetic order $\mathbf{Q}_m$ and the position of the magnetic cell $\mathbf{r}_n$:

$$\phi_n = \boldsymbol{Q}_m \cdot \boldsymbol{r}_n \tag{2.2}$$

Therefore, the transformation between to coordinates can be written as follows:

$$S_{i,lab} = \begin{pmatrix} S_i^{x0} \\ S_i^{y0} \\ S_i^{z0} \end{pmatrix}_{lab} = \hat{R}_i \begin{pmatrix} S_i^{x} \\ S_i^{y} \\ S_i^{z} \end{pmatrix}_{local} \tag{2.3}$$

$$S_{i,lab}^{\alpha} = \sum_{\mu} R_i^{\alpha\mu} \cdot S_{i,local}^{\mu} \tag{2.4}$$

where α and μ runs over the {x, y, z}. For the spiral order lying on the x-y plane, we can express the rotation matrix as

$$S_i = \begin{pmatrix} S_i^{x0} \\ S_i^{y0} \\ S_i^{z0} \end{pmatrix} = \begin{pmatrix} 0 & -sin\phi_i & cos\phi_i \\ 0 & cos\phi_i & sin\phi_i \\ -1 & 0 & 0 \end{pmatrix} \begin{pmatrix} S_i^{x} \\ S_i^{y} \\ S_i^{z} \end{pmatrix} \tag{2.5}$$

2.1.2 Holstein–Primakoff transformation

Spin operators can be expressed as bosonic operators using the Holstein–Primakoff transformation [Ref. 2.2]:

$$S_{mi}^{+} = \sqrt{2S - b_{mi}^{\dagger} b_{mi}}\, b_{mi},\ S_{mi}^{-} = b_{mi}^{\dagger} \sqrt{2S - b_{mi}^{\dagger} b_{mi}},\ S_{mi}^{z} = S - b_{mi}^{\dagger} b_{mi} \tag{2.6}$$

where $S_{mi}^{\pm} = S_{mi}^{x} \pm iS_{mi}^{y}$ and $b_{mi}\ (b_{mi}^{\dagger})$ is a magnon annihilation (creation) operator. By applying Eq. 2.4 and Eq. 2.6 to Eq. 2.1, the magnetic Hamiltonian can be expanded in the power of 1/S as follows [Ref. 2.3]:

$$H = H_0 + H_1 + H_2 + H_3 + O(S^{2-\left(\frac{m}{2}\right)}) \tag{2.7}$$

where H_m denotes the m^{th} power of the magnon operators b_i and $b_i^{\dagger}$. Physically, H_0 shows the classical ground state energy, and H_1 should vanish because it perturbs the ground state. The higher-order terms are expected to have a negligible effect for a large S case because $H_m \sim O(S^{(2-m/2)})$. However, these terms become significant at the quantum limit of S = 1/2.

2.1.3 Linear spin-wave theory

Non-interacting magnon can be calculated using only the quadratic term H_2 [Ref. 2.1]. In this case, it is useful to define two unit vectors:

$$z_i^\alpha = R_i^{\alpha x} + iR_i^{\alpha y} \tag{2.8}$$

$$v_i^\alpha = R_i^{\alpha z} \tag{2.9}$$

where v is a unit vector. The spin operators can be expressed with bosonic operators as follows:

$$S_{mi}^\alpha = \sqrt{\frac{S}{2}}\left(\bar{z}_i^\alpha b_{mi} + z_i^\alpha b_{mi}^\dagger\right) + v_i^\alpha\left(S - b_{mi}^\dagger b_{mi}\right) \tag{2.10}$$

Then, the Hamiltonian is given by:

$$H = \sum_{mn,ij,\alpha\beta}\left\{\sqrt{\frac{S}{2}}\left(\bar{z}_i^\alpha b_{mi} + z_i^\alpha b_{mi}^\dagger\right) + v_i^\alpha\left(S - b_{mi}^\dagger b_{mi}\right)\right\} J_{mi,nj}^{\alpha\beta}\left\{\sqrt{\frac{S}{2}}\left(\bar{z}_j^\beta b_{nj} + z_j^\beta b_{nj}^\dagger\right) + v_j^\beta\left(S - b_{nj}^\dagger b_{nj}\right)\right\} \tag{2.11}$$

After sorting to the quadratic order,

$$H_2 = \sum_{mn} x_m^\dagger h_{mn} x_m \tag{2.11}$$

where x_m is the basis vector of the magnon operator. The basis vector x_m is defined as:

$$x_m = \begin{bmatrix} b_{m1} \\ \vdots \\ b_{mN} \\ b_{m1}^\dagger \\ \vdots \\ b_{mN}^\dagger \end{bmatrix}, x_m^\dagger = \left[b_{m1}^\dagger, \dots , b_{mN}^\dagger, b_{m1}, \dots , b_{mN}\right] \tag{2.12}$$

where N is the number of magnetic atoms per unit cell.

To diagonalize H_2, one needs to express operators using reciprocal space representation with Fourier transform:

$$b_{mi} = \frac{1}{\sqrt{L}} \sum_{k \in B.Z.} b_i(k) e^{\boldsymbol{ik \cdot r}_m} \tag{2.13}$$

where L is the number of sites in the system. After Fourier transformation, the quadratic Hamiltonian can be rewritten as:

$$H = \sum_k X^\dagger(k) h_k X(k) \tag{2.14}$$

where X(k) is the Fourier transform of the magnon basis vector and is expressed as:

$$X(k) = \begin{bmatrix} b_1(k) \\ \vdots \\ b_N(k) \\ b_1^\dagger(-k) \\ \vdots \\ b_N^\dagger(-k) \end{bmatrix}, X^\dagger(k) = \left[b_1^\dagger(k), \dots , b_N^\dagger(k), b_1(-k), \dots , b_N(-k)\right] \tag{2.15}$$

We can solve this problem using the generalized Bogliubov transformation. First, we can define the commutation matrix *g* based on the property of bosonic operators:

$$\left[X, X^\dagger\right] = X(X^*)^T - (X^* X^T)T = \begin{pmatrix} I & 0 \\ 0 & -I \end{pmatrix} \equiv g \tag{2.16}$$

where I is an N × N identity matrix. The eigenvalues *d* and eigenvectors V of gh need to be calculated, where V constrains the eigenvectors as columns. The magnon dispersions are $\omega = g \cdot d$. Further, for each magnon energy, ω_i belongs to a linear combination of bosonic operators as $b_i' = \sum_j S_{ij} b_j$, where S can be calculated as

$$S = V \cdot (gV^T gV)^{-\frac{1}{2}} \tag{2.17}$$

This generalized solution of magnon dispersion with more than one magnetic sub-lattice is implemented in SpinW [Ref. 2.1], which has been widely used in the neutron scattering community, including this thesis.

2.1.4 Bond-dependent anisotropy with a non-collinear magnetic order

Interestingly, the generalized solution for the linear spin-wave theory (LSWT) simulation demonstrated in Chapter 2.1.3 can yield a wrong answer for some special cases. For instance, when the spin Hamiltonian undergoes a bond-dependent anisotropy exchange with the non-collinear magnetic order. However, it has been thoughtfully considered because most materials with bond-dependent anisotropy exchange have a collinear spin structure. This failure can be attributed to the assumption of periodicity in the spin Hamiltonian. Before we use the Fourier transform in Eq. 2.11, we assume that the exchange matrix J_{ij} is periodic as

$$J_{mi,nj}^{\alpha\beta} = J_{ij}^{\alpha\beta}(d) \tag{2.18}$$

where $d = r_n - r_m$ is the distance between the origin of 2 unit cells. This assumption is usually valid but fails in the presence of bond-dependent anisotropy. If the exchange matrix satisfies Eq. 2.18, then it only contains the $\phi_i - \phi_j = Q \cdot d$ term defined in Eq. 2.2. However, with the bond-dependent anisotropy, there is also an additional phase term: $\phi_i + \phi_j = 2Q \cdot r_i + Q \cdot d$. The position-dependent term $Q \cdot r$ cannot disappear for the non-collinear case. Therefore, Fourier transformation is required for a non-collinear magnetic order with bond-dependent anisotropy.

This is the case for CoI$_2$, which is discussed in Chapter 6. Here, we will briefly explain the LSWT calculations for bond-dependent anisotropy with a non-collinear order. In CoI$_2$, we can minimize the spin Hamiltonian on a triangular lattice as follows:

$$\begin{aligned} H = \sum_{<i,j>_n}^{n=1} & \{J_1[S_i^x S_j^x + S_i^y S_j^y + \Delta_1 S_i^z S_j^z] \\ & + 2J_{\pm\pm}[(S_i^x S_j^x - S_i^y S_j^y)\cos\phi_\alpha - (S_i^x S_j^y + S_i^y S_j^x)\sin\phi_\alpha]\} \\ & + \sum_{<i,j>_n}^{n=3} J_3[S_i^x S_j^x + S_i^y S_j^y + \Delta_3 S_i^z S_j^z] \end{aligned} \tag{2.20}$$

where $\phi_\alpha \in \left\{0, \pm\frac{2\pi}{3}\right\}$ is a bond-dependent phase factor for each bond. Using the rotation frame method with Eq. 2.5, we can express the quadratic order H_2 of the spin Hamiltonian as follows:

$$\begin{aligned} H = \sum_{<\mathrm{i,j}>} \Big[& J_1 \left\{\Delta_1 \tilde{S}_i^x \tilde{S}_j^x + \cos(\phi_i - \phi_j)\left(\tilde{S}_i^z \tilde{S}_j^z + \tilde{S}_i^y \tilde{S}_j^y\right)\right\} \\ & + 2J_{\pm\pm}\cos(\phi_\alpha + \phi_i + \phi_j)\left(\tilde{S}_i^z \tilde{S}_j^z - \tilde{S}_i^z \tilde{S}_j^z\right)\Big] \\ & + \sum_{<\mathrm{i,j}>_\mathrm{n}} J_n \left[\Delta_\mathrm{n} \tilde{S}_i^x \tilde{S}_j^x + \cos(\phi_i - \phi_j)\left(\tilde{S}_i^z \tilde{S}_j^z + \tilde{S}_i^y \tilde{S}_j^y\right)\right] \end{aligned} \tag{2.21}$$

In this case, the position-dependent phase terms become

$$\phi_i - \phi_j = (\boldsymbol{Q}\cdot\boldsymbol{r} + \phi_0) - (\boldsymbol{Q}\cdot(\boldsymbol{r} + \Delta\boldsymbol{r}) + \phi_0) = \boldsymbol{Q}\cdot\Delta\boldsymbol{r} \tag{2.22}$$

$$\phi_i + \phi_j = (\boldsymbol{Q}\cdot\boldsymbol{r} + \phi_0) + (\boldsymbol{Q}\cdot(\boldsymbol{r} + \Delta\boldsymbol{r}) + \phi_0) = 2\boldsymbol{Q}\cdot\boldsymbol{r} + 2\phi_0 + \boldsymbol{Q}\cdot\Delta\boldsymbol{r} \tag{2.23}$$

where ϕ_0 indicates the initial position. Using the Holstein–Primakoff transformation, the spin Hamiltonian can be expressed as

$$\begin{aligned} H = \sum_{<i,j>} \Bigg\{ & J\left[\frac{\Delta S}{2}(K_{ij} + P_{ij}) + \cos(Q\cdot\Delta r)\left(S^2 - b_i^\dagger b_i - b_j^\dagger b_j + \frac{S}{2}(K_{ij} - P_{ij})\right)\right] \\ & + 2J_{\pm\pm}\cos(\tilde{\phi}_p + 2Q\cdot r + Q\cdot\Delta r)\left(S^2 - b_i^\dagger b_i - b_j^\dagger b_j - \frac{S}{2}(K_{ij} - P_{ij})\right)\Bigg\} \end{aligned} \tag{2.24}$$

where $\tilde{\phi}_p = \phi_\alpha + 2\phi_0$ and $K_{\mathrm{ij}} = b_i b_j^\dagger + b_i^\dagger b_j$, $P_{\mathrm{ij}} = b_i b_j + b_i^\dagger b_j^\dagger$.

We can obtain the quadratic form of the magnetic Hamiltonian in the momentum space via inverse Fourier transform. However, in this case, due to the position-dependent phase $2Q \cdot r$, the bosonic operators depend on both k and $k \pm 2Q$. For example,

$$\sum_r \cos(2Q \cdot r)\, b_r b_{r+\Delta r} = \frac{1}{N} \sum_{r,k,k'} \cos(2Q \cdot r)\, e^{ik\cdot r} e^{ik'\cdot(r+\Delta r)}\, b_k b_{k'}$$

$$= \sum_{k,k'} \left[\frac{1}{N} \sum_r \cos(2Q \cdot r)\, e^{i(k+k')\cdot r} \right] e^{ik'\cdot\Delta r} b_k b_k'$$

$$= \frac{1}{2} \sum_{k,k'} [\delta(k + k' + 2Q) + \delta(k + k' - 2Q)] e^{ik'\cdot\Delta r} b_k b_{k'}$$

$$= \frac{1}{2} \sum_k \left[e^{-i(k+2Q)\cdot\Delta r} b_k b_{-(k+2Q)} + e^{-i(k-2Q)\cdot\Delta r} b_k b_{-(k-2Q)} \right] \tag{2.25}$$

This dependency increases the matrix size from 2 × 2 to 6 × 6. Subsequently, the model Hamiltonian with quadratic terms transforms to

$$H_2 = \sum_{\mathbf{k}} \hat{\boldsymbol{x}}_{\boldsymbol{k}}^\dagger \, \hat{\boldsymbol{H}}_{\boldsymbol{k}} \hat{\boldsymbol{x}}_{\boldsymbol{k}} \tag{2.26}$$

where $\hat{\boldsymbol{x}}_{\boldsymbol{k}}^\dagger = \left[b_{\boldsymbol{k}+2\boldsymbol{Q}}^\dagger, b_{\boldsymbol{k}}^\dagger, b_{\boldsymbol{k}-2\boldsymbol{Q}}^\dagger, b_{-\boldsymbol{k}-2\boldsymbol{Q}}, b_{-\boldsymbol{k}}, b_{-\boldsymbol{k}+2\boldsymbol{Q}} \right]$ is a vector of length 6, and $\hat{H}_k$ is a 6 × 6 matrix with

$$\hat{\boldsymbol{H}}_{\boldsymbol{k}} = \begin{pmatrix} 0 & C_2(\boldsymbol{k}) & 0 & 0 & D_1(\boldsymbol{k}) & 0 \\ C_2^*(\boldsymbol{k}) & A(\boldsymbol{k}) & C_1(\boldsymbol{k}) & D_1^*(\boldsymbol{k}) & B(\boldsymbol{k}) & D_2(\boldsymbol{k}) \\ 0 & C_1^*(\boldsymbol{k}) & 0 & 0 & D_2^*(\boldsymbol{k}) & 0 \\ 0 & D_1(\boldsymbol{k}) & 0 & 0 & C_2(\boldsymbol{k}) & 0 \\ D_1^*(\boldsymbol{k}) & B(\boldsymbol{k}) & D_2(\boldsymbol{k}) & C_2^*(\boldsymbol{k}) & A(\boldsymbol{k}) & C_1(\boldsymbol{k}) \\ 0 & D_2^*(\boldsymbol{k}) & 0 & 0 & C_1^*(\boldsymbol{k}) & 0 \end{pmatrix}$$

$$A(\mathbf{k}) = \frac{S}{2} \sum_{\Delta \mathrm{r}} J_{\Delta r} [\varDelta_{\mathrm{n}} - \cos(\boldsymbol{Q} \cdot \boldsymbol{\Delta r})] \cos(\boldsymbol{k} \cdot \boldsymbol{\Delta r}) - S \sum_{\Delta \mathrm{r}} J_{\Delta r} \cos(\boldsymbol{Q} \cdot \boldsymbol{\Delta r})$$

$$B(\mathbf{k}) = \frac{S}{2}\sum_{\Delta r} J_{\Delta \mathrm{r}}[\mathit{\Delta}_{\mathrm{n}} + \cos(\boldsymbol{Q}\cdot\boldsymbol{\Delta r})]\cos(\boldsymbol{k}\cdot\boldsymbol{\Delta r})$$

$$C_1(\boldsymbol{k}) = -\frac{S}{4}\sum_{\Delta r} e^{-i(\phi_\alpha + 2\boldsymbol{Q}\cdot\boldsymbol{\Delta r})}\cos(\boldsymbol{Q}\cdot\boldsymbol{\Delta r}) - \frac{S}{8}\sum_{\Delta r} e^{-i(\phi_\alpha + 3\boldsymbol{Q}\cdot\boldsymbol{\Delta r} - \boldsymbol{k}\cdot\boldsymbol{\Delta}\mathbf{r})}$$

$$C_2(\boldsymbol{k}) = -\frac{S}{4}\sum_{\Delta r} e^{-i(\phi_\alpha + 2\boldsymbol{Q}\cdot\boldsymbol{\Delta r})}\cos(\boldsymbol{Q}\cdot\boldsymbol{\Delta r}) - \frac{S}{8}\sum_{\Delta r} e^{-i(\phi_\alpha + 3\boldsymbol{Q}\cdot\boldsymbol{\Delta r} + \boldsymbol{k}\cdot\boldsymbol{\Delta}\mathbf{r})}$$

$$D_1(\boldsymbol{k}) = \frac{S}{8}\sum_{\Delta r} e^{-i(\phi_\alpha + 3\boldsymbol{Q}\cdot\boldsymbol{\Delta r} + \boldsymbol{k}\cdot\boldsymbol{\Delta r})},\quad D_2(\mathbf{k}) = \frac{S}{8}\sum_{\Delta r} e^{-i(\phi_\alpha + 3\boldsymbol{Q}\cdot\boldsymbol{\Delta r} - \boldsymbol{k}\cdot\boldsymbol{\Delta r})}$$

The eigenvectors are obtained by diagonalizing $\hat{\boldsymbol{g}}\widehat{\boldsymbol{H}}_{\boldsymbol{k}}$ using the diagonalization method demonstrated in Eq. 2.17.

2.2 Magnon decay due to multi-magnon Continuum

2.2.1 Three-boson interaction and its origin

During the interaction, a magnon can decay into multiple magnons or other types of quasiparticles. However, the decay only occurs when the magnon can satisfy a kinematic condition, in which both momentum and energy should be conserved. Therefore, searching the area where the kinematic constraint holds will guide us to the possible magnon decay region. Fig. 2.1 shows a schematic example of magnon decay with a multi-particle continuum. The area where the decay occurs is continuous in the energy–momentum space and is thus called a multi-particle continuum. When a magnon branch enters a continuum, its lifetime becomes finite, and its energy is renormalized.

Considering spin-wave expansion with the Holstein–Primakoff transformation, the higher-order terms (m > 2 in Eq. 2.7) indicate magnon decay into multiple magnon modes. For

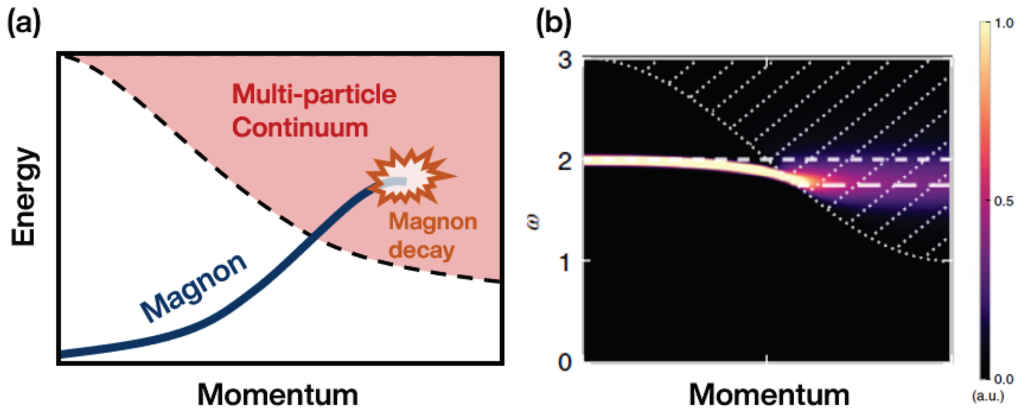

Figure 2.1 (a) General schematic of magnon decay due to a multi-particle continuum. (b) Calculated quasiparticle decay with interaction between a bare state and the continuum state, adapted from [Ref. 2.13]. The dashed area indicates the multi-particle continuum.

example, the leading order among the higher orders is H_3 and can be generalized as follows [Ref. 2.3]:

$$H_3 = \sum_{1-3} V_3^{(1)} b_1^\dagger b_2^\dagger b_3 \delta(k_1 + k_2 - k_3) + H.c. \tag{2.27}$$

where $V_3^{(1)}$ is the vertex function related to the decay process of one magnon into two magnons. This three-boson term leads to magnon decay into two magnons with kinematic constraints. They originate from the coupling of the local S^z and $S^{x(y)}$ spin components, which is evident from the form of the Holstein–Primakoff transformation ($S^z \sim O(b^2)$, $S^{x(y)} \sim O(b)$). Therefore, coupling between transverse and longitudinal spin fluctuations is essential to induce a spontaneous magnon decay from magnon–magnon interactions.

Traditionally, a non-collinear magnetic structure is utilized to achieve the transverse–longitudinal coupling. Based on the isotropic Heisenberg model (Eq. 2.5), the spin Hamiltonian can be written as follows [Ref. 2.3]:

$$H = \sum_{<i,j>} J_{ij} \left\{ S_i^x S_j^x + \cos\phi_{i-j} \left(S_i^z S_j^z + S_i^y S_j^y \right) + \sin\phi_{i-j} \left(S_i^z S_j^y - S_i^z S_j^y \right) \right\} \quad (2.28)$$

where $\phi_{i-j} = \phi_i - \phi_j$. With Holstein–Primakoff transformation, we can express this spin Hamiltonian in terms of bosonic operators as shown in Eq. 2.7. Then, the cubic terms (m = 3) in this relationship can be expressed as follows [Ref. 2.3]:

$$H_3 = J \sqrt{\frac{S}{2}} \sum_{i,j} sin\phi_{i-j} \left[b_i^\dagger b_i \left(b_j^\dagger + b_j \right) - b_j^\dagger b_j \left(b_i^\dagger + b_i \right) \right] \quad (2.29)$$

We can find that this term becomes zero in the collinear magnetic structure because $sin\phi_{i-j} \equiv 0$.

Another route to coupling the two orthogonal spin fluctuations is bond-dependent anisotropy [Ref. 2.4–2.6]. In this case, the terms like $S^x S^z$ solely originate from the low symmetry of the spin Hamiltonian. For example, the H_3 term with the bond-dependent anisotropy $J_{\pm\pm}$ term for a triangular lattice can be expressed as follows:

$$H_3 = -2J_{\pm\pm} \sqrt{\frac{S}{2}} \sum_{<i,j>} \sin\left(\phi_\alpha + \phi_i + \phi_j \right) \left[b_i^\dagger b_i \left(b_j^\dagger + b_j \right) - b_j^\dagger b_j \left(b_i^\dagger + b_i \right) \right] \quad (2.30)$$

where $\phi_\alpha \in \left\{ 0, \pm\frac{2\pi}{3} \right\}$ is a bond-dependent phase factor for each bond. In this case, H_3 term is non-zero regardless of magnetic order, and therefore, a bond-dependent anisotropy allows magnon decay even in a collinear magnetic structure [Ref. 2.4–2.6].

With Fourier transform, the general three-boson terms can be expressed in the momentum space as [Ref. 2.3,2.7]:

$$H_3 = \sum_{\mathbf{k},\mathbf{q}} \left(\frac{1}{2!} \Gamma_1(\mathbf{q}, \mathbf{k}-\mathbf{q}; \mathbf{k})\, b_{\mathbf{q}}^\dagger b_{\mathbf{k}-\mathbf{q}}^\dagger b_{\mathbf{k}} + \frac{1}{3!} \Gamma_2(\mathbf{q}, -\mathbf{k}-\mathbf{q}, \mathbf{k}) b_{\mathbf{q}}^\dagger b^\dagger_{-\mathbf{k}-\mathbf{q}} b_{\mathbf{k}}^\dagger + \mathrm{H.c.} \right), \quad (2.31)$$

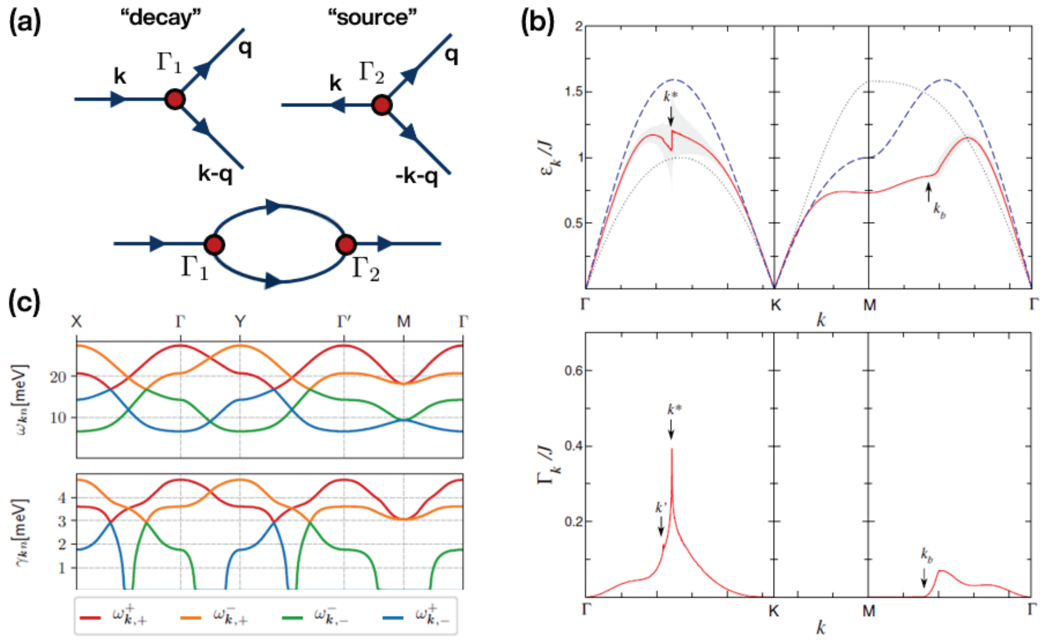

Figure 2.2 (a) Feynman diagrams of two vertices in H_3, magnon 'decay' (left upper) and 'source'; the lower part shows the magnon self-energy from a pair of decay vertex. (b) Energy renormalisation (upper) and decay rate (lower) of magnons in an S = 1/2 TLAF, with a magnetic order of 120°, calculated using the 1/S correction. (c) Energy calculated using the LSWT and decay rate of magnons in the Kitaev material RuCl$_3$ based on the constant matrix element iDE approximation. Each colour coding in the decay rate is the same as that for the magnon energy. (b)-(c) are adapted from [Ref. 2.3,2.4].

where Γ_1 and Γ_2 are the magnon decay and source vertices, respectively, which are derived from the eigenvector components of the non-interacting magnons (S_{ij} in Eq. 2.17; a complete description of these vertices is reported in [Ref. 2.3]. These vertices contribute to magnon self-energy, whose imaginary (real) part describes the decay (renormalization) of non-interacting magnons. Fig. 2.2(b),(c) show the LSWT calculation results and magnon self-energy of an S = 1/2 triangular lattice antiferromagnet (TLAF), with a magnetic order of 120° [Ref. 2.3], and the Kitaev material RuCl$_3$ [Ref. 2.4]. As expected, the calculated

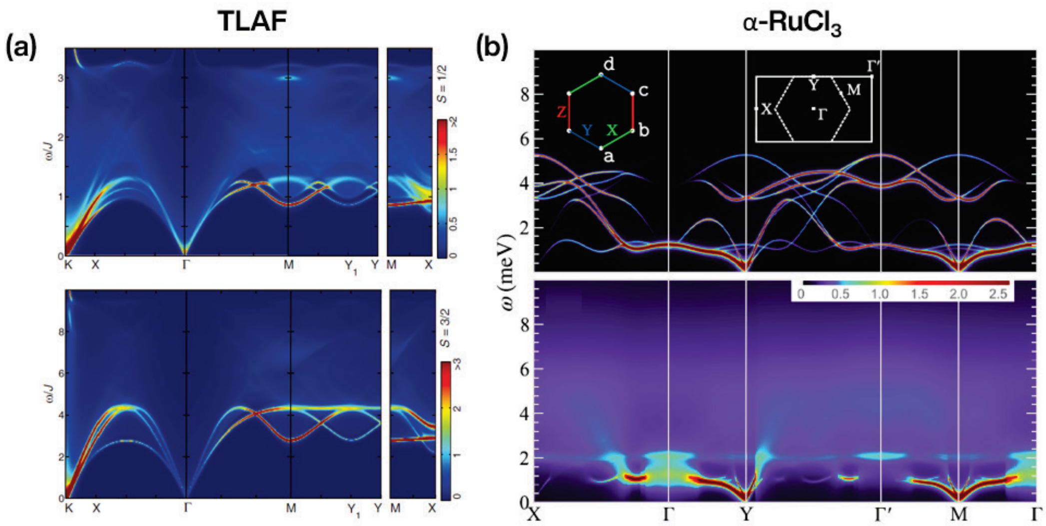

Figure 2.3 (a) Intensity of the dynamical structure factors of $S = 1/2$ (upper) and $S = 3/2$ (lower) TLAFs with a magnetic order of 120°, calculated using the 1/S correction. (b) Dynamical structure factor of $RuCl_3$ calculated using LSWT (upper) and including magnon decay (lower). The figures are adapted from [Ref. 2.5,2.8]

dynamical structure factor reveals a broadening of magnon intensity in both systems, as shown in Fig. 2.3 [Ref. 2.5,2.8].

2.2.2 Continuum of the two-magnon density of states

In Chapter 2.2.1, it is evident that calculating the decay rates of magnons resulting from two-magnon processes requires complex computations, even though the concept is straightforward. In contrast, the density of states (DOS) of a two-magnon continuum offers a simple yet effective measure for comprehending the characteristics of the Continuum [Ref. 2.9–2.12]. For example, the two-magnon Continuum DOS (D_m) at ($\mathbf{q}$, E) can be calculated using the following expressions:

$$D_m(\mathbf{q},E) = \frac{1}{N}\sum_{i,j}\sum_{\mathbf{k}}\delta(E - E_{\mathbf{k},i} - E_{\mathbf{q-k},\mathrm{j}}), \tag{2.31}$$

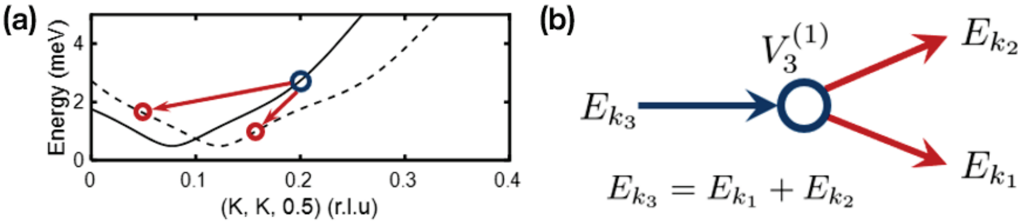

Figure 2.4 Schematic of the two-magnon scattering process and three-boson terms. (a) the two-magnon decay of a single magnon with kinematic constraints. The magnon dispersion in (a) originates from CoI_2 (see Chapter 6). (b) Corresponding Feynman diagram of the vertex of the three-boson term.

where $E_{\mathrm{k},i}$ and $\epsilon_{\mathbf{k},j}$ denote the energy of the i^{th} magnon modes, **k** is a three-dimensional momentum grid over the first Brillouin zone, and N is the normalization constant. Fig. 2.4 demonstrates that the Continuum DOS for each channel corresponds to the number of decay channels that fulfil the kinematic condition at (q, E). Hence, this quantity is relevant to the decay rate and is employed for comparing magnon damping. Such a quantity plays an essential role in explaining the magnon damping in $Na_3Co_2SbO_6$, $Na_2Co_2TeO_6$ (Ch. 5) and CoI_2 (Ch. 6) because calculating the decay rates for these compounds need tremendous theoretical inputs.

References

[Ref. 2.1] Toth, S. and B. Lake, Journal of Physics: Condensed Matter **27**, 166002 (2015).

[Ref. 2.2] Holstein, T. and H. Primakoff, Physical Review **58**, 1098 (1940).

[Ref. 2.3] Chernyshev, A. L. and M. E. Zhitomirsky, Phys Rev B **79**, 144416 (2009).

[Ref. 2.4] Smit, R. L. et al., Phys Rev B **101**, 054424 (2020).

[Ref. 2.5] Maksimov, P. A. and A. L. Chernyshev, Phys Rev Res **2**, 033011 (2020).

[Ref. 2.6] Winter, S. M. et al., Nat Commun **8**, 1152 (2017).

[Ref. 2.7] Zhitomirsky, M. E. and A. L. Chernyshev, Rev Mod Phys **85**, 219 (2013).

[Ref. 2.8] Mourigal, M. et al., Phys Rev B **88**, 094407 (2013).

[Ref. 2.9] Kim, T. et al., J Physical Soc Japan **88**, 081003 (2019).

[Ref. 2.10] Oh, J. et al., Phys Rev Lett **111**, 257202 (2013).

[Ref. 2.11] Oh, J. et al., Nat Commun **7**, 13146 (2016).

[Ref. 2.12] Park, P. et al., Phys Rev Lett **125**, 027202 (2020).

[Ref. 2.13] Verresen, R., R. Moessner, and F. Pollmann, Nat Phys **15**, 750 (2019).

Chapter 3

Experimental techniques

3.1 Sample synthesis

Material synthesis is the primary step towards investigating new materials. This section introduces the methods for synthesizing polycrystalline $CoPS_3$, $Na_2Co_2TeO_6$, $Na_3Co_2SbO_6$, and single-crystal CoI_2.

3.1.1 Solid-state reaction method

The solid-state reaction is the most widely used method for preparing polycrystalline solids from a mixture of solid starting materials [Ref. 3.1]. First, raw chemicals must be prepared to match the chemical formula and stoichiometry. An excess amount of raw materials is required if the chemical is volatile. These chemicals are evenly mixed and ground by agate mortar, usually at a rate of 30 min per gram. After grounding, the mixed chemicals are pressed into pellets. This pelletization is crucial because it reduces the distance between the chemicals and boosts the reaction during sintering. Depending on the chemical, the pressed pellet should be used with an appropriate crucible (aluminium or platinum) due to the possible reaction between the pellet and the crucible. Finally, the pellet is heated at a high temperature for a couple of days to form the target materials. After sintering, the sintered pellets are ground into powder or broken into small pieces for characterization. Usually, a mono-phase sample is obtained after several sintering processes. In this study, three high-quality polycrystalline samples, $CoPS_3$, $Na_3Co_2SbO_6$, and $Na_2Co_2TeO_6$ (see Fig. 3.1 for the

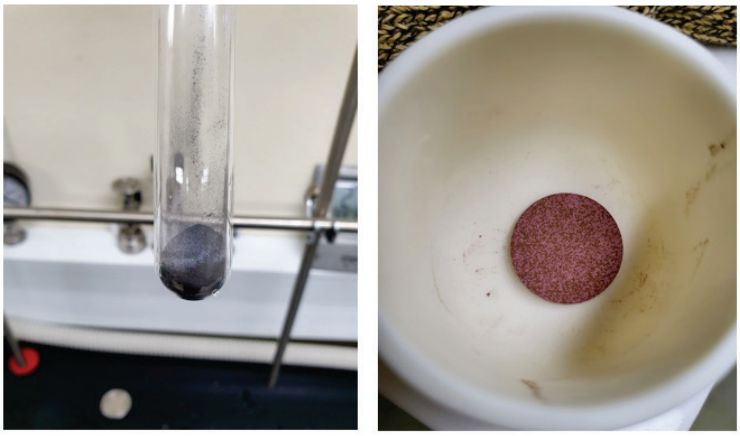

Figure 3.1 Picture of prepared polycrystalline samples. Left side is $CoPS_3$; right side is $Na_3Co_2SbO_6$.

picture of samples), were prepared.

Polycrystalline samples of $CoPS_3$ were synthesized with stoichiometric quantities of cobalt, phosphorus, and sulphur. These chemicals were placed in a quartz ampoule inside a glove box under an Ar atmosphere. The total mass of the chemicals was 2 g, and their purity was better than 99.99 %. The ampoule was sealed under 5 Torr of argon gas. After sealing, the sealed ampoule was heated in a tube furnace. The temperature was raised to 530 °C in 6 h and held at this value for two days.

Polycrystalline $Na_2Co_2TeO_6$ was prepared by a solid-state reaction method. First, Na_2CO_3 (Alfa, 99.997 %), Co_3O_4 (Alfa, 99.7 %), and TeO_2 (Alfa, 99.99 %) were mixed in a stoichiometric molar ratio with 5 % excess Na_2CO_3 and fully ground; afterwards the mixture was loaded in an alumina crucible and sintered at 850 °C for 40 h in air.

The polycrystalline $Na_3Co_2SbO_6$ sample was prepared by a conventional two-step solid-state reaction. First, stoichiometric amounts of Sb_2O_3 (99.6 %, Alfa Aesar), Co_3O_4 (99.9 %, Sigma Aldrich), and 5 % excess of Na_2CO_3 (99.9 %, Merck) were ground together and annealed at 800 °C for 15 h in air. After cooling to room temperature, the mixture was ground again, pressed into a pellet, and annealed at 980 °C for 40 h in air, followed by quenching in air.

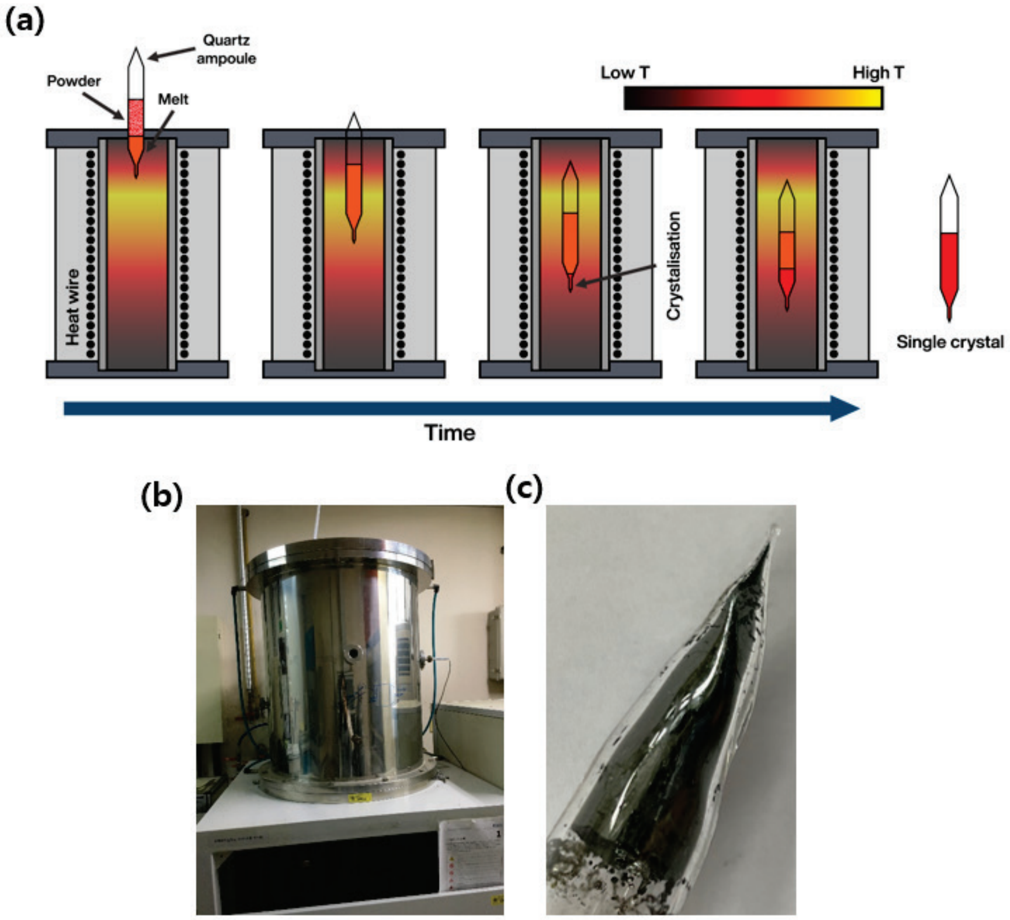

Figure 3.2 Illustration of the Bridgman technique. (a) Schematic of the Bridgman method. (b) Customised Bridgman furnace for CoI_2 synthesis. (c) Single crystal of CoI_2 prepared using a Bridgman furnace.

3.1.2 Bridgman method

Bridgman method (or Bridgman–Stockbarger method) is a crystal growth method used to produce large single crystals with controlled compositions and a high crystalline quality [Ref. 3.1]. Fig. 3.2 illustrates the Bridgman technique, which involves melting a precursor material in a crucible and slowly pulling it out of a temperature gradient furnace while maintaining a constant temperature gradient. As the crucible is slowly withdrawn, the molten material solidifies into a single crystal along the withdrawal direction. For growing a high-crystalline sample, one needs to prepare a quartz ampoule with a sharp end, which can act as a seed.

Single crystals of CoI_2 were synthesized using a customized Bridgman furnace, and 5 g of anhydrous CoI_2 powder (Alfa Aesar, 99.999 % purity) was used as the starting material. The CoI_2 powder was sealed in an evacuated silica tube (14 mm diameter, 1 mm wall thickness) under a pressure of $\sim 10^{-4}$ Torr. The sealed tube was then heated to 535 °C for 6 h and held at 535 °C for 110 h. The tube was pulled down at 535 °C with a growth rate of $0.5\ \mathrm{mm \cdot h^{-1}}$. The resulting single crystal was 2–30 mm long and 14 mm in diameter with a shiny black colour.

3.2 Inelastic neutron scattering

In condensed matter experiments, the focus is on measuring the four fundamental degrees of freedom: lattice, charge, spin, and orbital. Each of these degrees of freedom is studied using various experimental techniques. Among these techniques, (inelastic) neutron scattering is arguably the most powerful method for investigating the spin degree of freedom, specifically magnetism. This section introduces the experimental and theoretical foundations of (inelastic) neutron scattering.

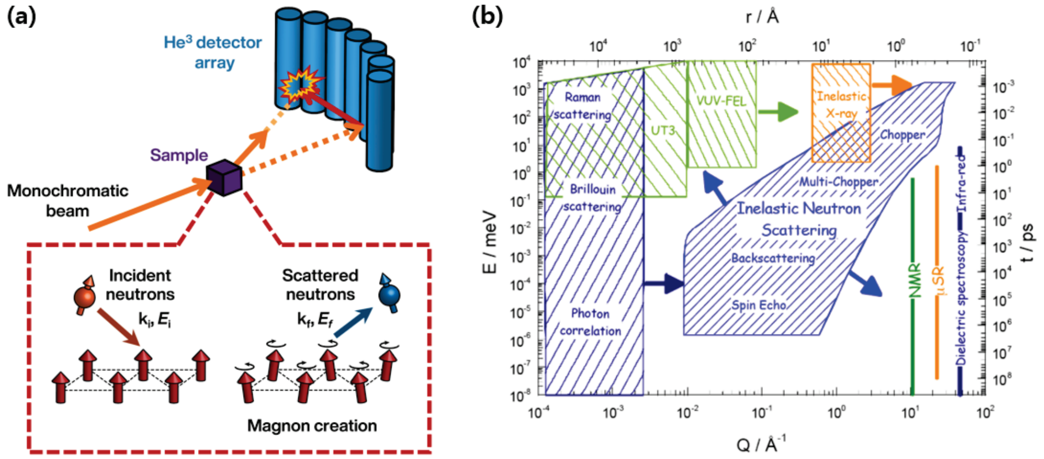

Figure 3.3 Basic of the neutron scattering process. (a) A general geometry of a neutron scattering measurement set-up, including illustration of how neutrons interact with magnons. (b) Energy–momentum convergence of the INS technique and comparison with other experimental techniques adapted from [Ref. 3.15].

3.2.1 Basic principle

Inelastic neutron scattering (INS) is a novel technique used for examining the physical properties of a material by detecting the neutrons scattered from it. Since neutron has spin, we can probe the spin degrees of freedom via the dipole–dipole interactions between the magnetic moments of the material and those of the neutrons [Ref. 3.2]. Moreover, neutron scattering can also probe phonons because neutrons can penetrate solids and approach close to the nuclei.

The general neutron scattering process with a direct geometry is shown in Fig. 3. 3(a). A monochromatic beam with fixed incident energy (E_i) and momentum (k_i) is scattered by a target sample. After the scattering process, the neutron with final energy (E_f) and momentum (k_f) is detected by an array of detector tubes filled with ^{3}He gas [Ref. 3.2]. During the scattering process, both energy and momentum conservation laws must be satisfied as follows:

$$\boldsymbol{Q} = \boldsymbol{k}_f - \boldsymbol{k}_i,$$

$$E_f - E_i = \hbar\omega = \frac{\hbar^2}{2m_n}\left(\boldsymbol{k}_f^2 - \boldsymbol{k}_i^2\right),$$

where m_n is the mass of the neutron. Thus, we can observe the dynamical magnetic response of a sample with transferred neutrons (E, Q) using the INS technique.

The neutron scattering cross-section can be theoretically expressed using Fermi's golden rule [Ref. 3.2]:

$$\frac{d^2\sigma}{d\Omega dE} = \left(\frac{\mathrm{m}}{2\pi\hbar^2}\right)^2 \frac{|\mathrm{k_f}|}{|k_i|} \sum_{\lambda_i,\sigma_i} \sum_{\lambda_f,\sigma_f} p_{\lambda_i} p_{\sigma_i} \left|\langle \mathbf{k}_f, \boldsymbol{\sigma}_f, \lambda_f \middle| \hat{U} \middle| \mathbf{k}_i, \boldsymbol{\sigma}_i, \lambda_i \rangle\right|^2 \delta\left(E + E_i - E_f\right), \quad (3.3)$$

where p_α is the thermal population factor of a state $|\alpha\rangle$, and U is the interaction operator between the neutron and the sample, depending on the specific scattering process. If we change U as a dipole–dipole interaction, then we can rewrite the differential cross-section as follows:

$$\frac{d^2\sigma}{d\Omega d\omega} = (\gamma r_0)^2 \frac{k'}{k} N \left(\frac{1}{2} g F_{mag}(Q)\right)^2 e^{-2W} \sum_{\alpha,\beta} \left(\delta_{\alpha\beta} - \hat{Q}_\alpha \hat{Q}_\beta\right) S^{\alpha\beta}(Q,\omega)$$

where γ is the gyromagnetic ratio; r_0 is the classical electron radius; N is the number of unit cells in the crystal; g is the Lande splitting factor; $F_{mag}(Q)$ is the magnetic form factor, i.e. the Fourier transform of the magnetization distribution of a single magnetic atom; and $S^{\alpha\beta}(Q,\omega)$ is the dynamical structure factor, which provides information on the spin–spin correlation in the momentum and energy space. Therefore, we can directly observe the correlation of the spins in a sample by counting the scattered neutrons [Ref. 3.2].

Fig. 3. 3(b) compares the measurable area between the INS and other techniques in both momentum and energy ranges. Usually, optical techniques (infrared or Raman spectroscopy) can only be used to measure the inelastic signal with nearly zero momentum transfer. However, because of a large detector in real space, the INS method can be employed to measure the inelastic signal with a wide momentum range. Because of the recent developments in inelastic X-ray scattering, this method can now be used to observe a magnetic signal similar to the INS technique; however, observing the excitations with the exact resolution obtained using the INS method is still a considerable challenge. Therefore, INS is the best technique to explore the magnetic response of condensed matter with a comprehensive energy and momentum space.

3.2.2 Time-of-flight (ToF) technique

As highlighted in the previous section, the INS method facilitates the observation of elementary quasiparticles in a high resolution with a broad momentum and energy (Q, E) range. This study employed a time-of-flight (ToF) spectrometer for the INS experiment. Fig. 3.4 shows a schematic of the ToF spectrometer [Ref. 3.2]. Because the velocities of the neutrons used in a scattering experiment are typical of the order of a few hundred or thousand metres per second, their energy can be determined by measuring their flight time (t) over a distance (d ~ few metres). First, the neutron beam pulse originating from a spallation source travels through a guide and is then monochromatized by a disc chopper or a Fermi chopper [Ref. 3.3]; this monochromatization process allows us to select the desired incident energy. Then, the energy transfer (Q, E) and momentum of the detected

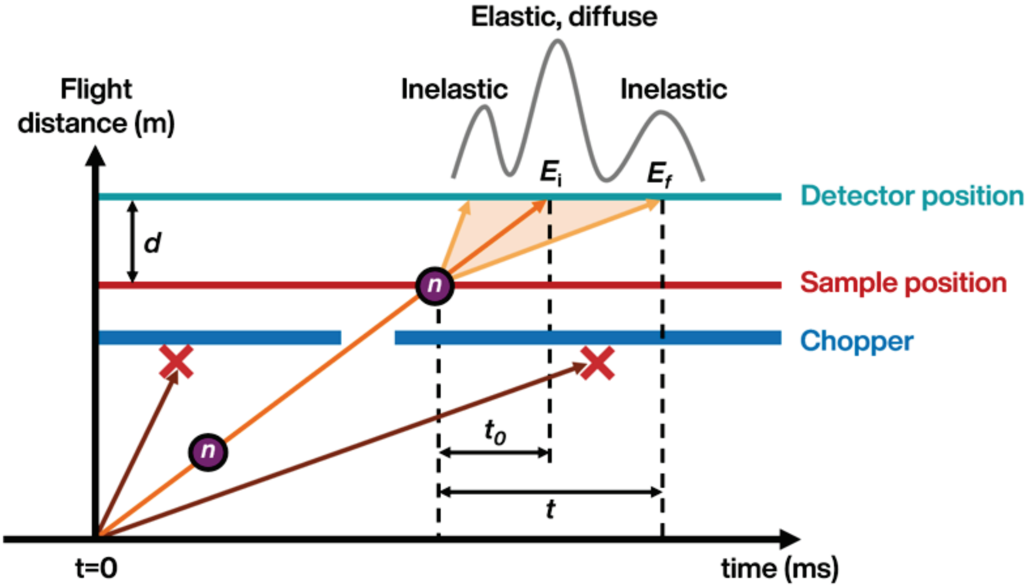

Figure 3.4 Schematic of the ToF INS measurement set-up

neutron can be determined as follows.

$$E_f - E_i = \hbar\omega = \frac{m_n}{2} d^2 \frac{t^2 - t_0^2}{t^2 t_0^2}$$

$$Q = \frac{m_n}{\hbar} d \sqrt{\frac{t^2 + t_o^2 - 2t_0 t cos(2\theta)}{t_0^2 t^2}}$$

where *d* is the distance between the sample position and the detector array, and t_0 and t are the ToF of the scattered neutrons with E_i and E_f, respectively. Without energy loss, we can detect the static spin–spin correlations. Therefore, the ToF technique facilitates neutron diffraction (elastic, diffuse) and inelastic measurements. After the measurements, we obtain a massive amount of four-dimensional (one for energy, three for momentum space) datasets over a wide range; the dataset size is usually a few hundred gigabytes. For the analysis, we used specialized software, such as Mantid [Ref. 3.4], Horace [Ref. 3.5], and Utusemi [Ref. 3.6].

3.2.3 INS experiment at the HRC, J-PARC

To measure the spin-wave spectra of three materials, viz. $CoPS_3$, $Na_3Co_2SbO_6$, and $Na_2Co_2TeO_6$, we used the HRC ToF spectrometer installed in the Japan Proton Accelerator Research Complex (J-PARC), Japan [Ref. 3.7]. The HRC spectrometer is designed to deliver high-resolution and relatively high-energy neutrons. It covers a wide energy transfer range (E_i) from 1 meV to 2 eV and shows a high resolution with $\frac{\Delta E}{E_i} = 1\text{–}2$ %. The overall schematic of the HRC is displayed in Fig. 3.5. Because the target incident energy of the HRC is significantly large, the HRC spectrometer uses a curved Fermi chopper to monochromatize fast neutrons [Ref. 3.8].

For $CoPS_3$ measurement, we placed 2 g of this polycrystalline sample on an aluminium holder. We measured the INS data at temperatures of 8, 35, 60, 85, 110, and 200 K. An incident energy of E_i = 71.3 and 30.4 meV with a Fermi chopper frequency of f = 200 Hz was used. We also measured the background at room temperature for performing background subtraction at each incident energy.

In the case of $Na_3Co_2SbO_6$ and $Na_2Co_2TeO_6$, these polycrystalline samples were also placed in aluminium holders. The INS data of $Na_3Co_2SbO_6$ were measured at T = 3, 15, and 50 K with incident energies of E_i = 7.14, 12.19, 16.54, 35.61, 50.9, and 122.6 meV. In contrast, the INS data of $Na_2Co_2TeO_6$ were measured at T = 3, 10, 20, 30, 50, and 95 K with E_i = 11.44, 16.54, 50.9, and 122.6 meV.

3.2.4 INS experiment at AMATERAS, J-PARC

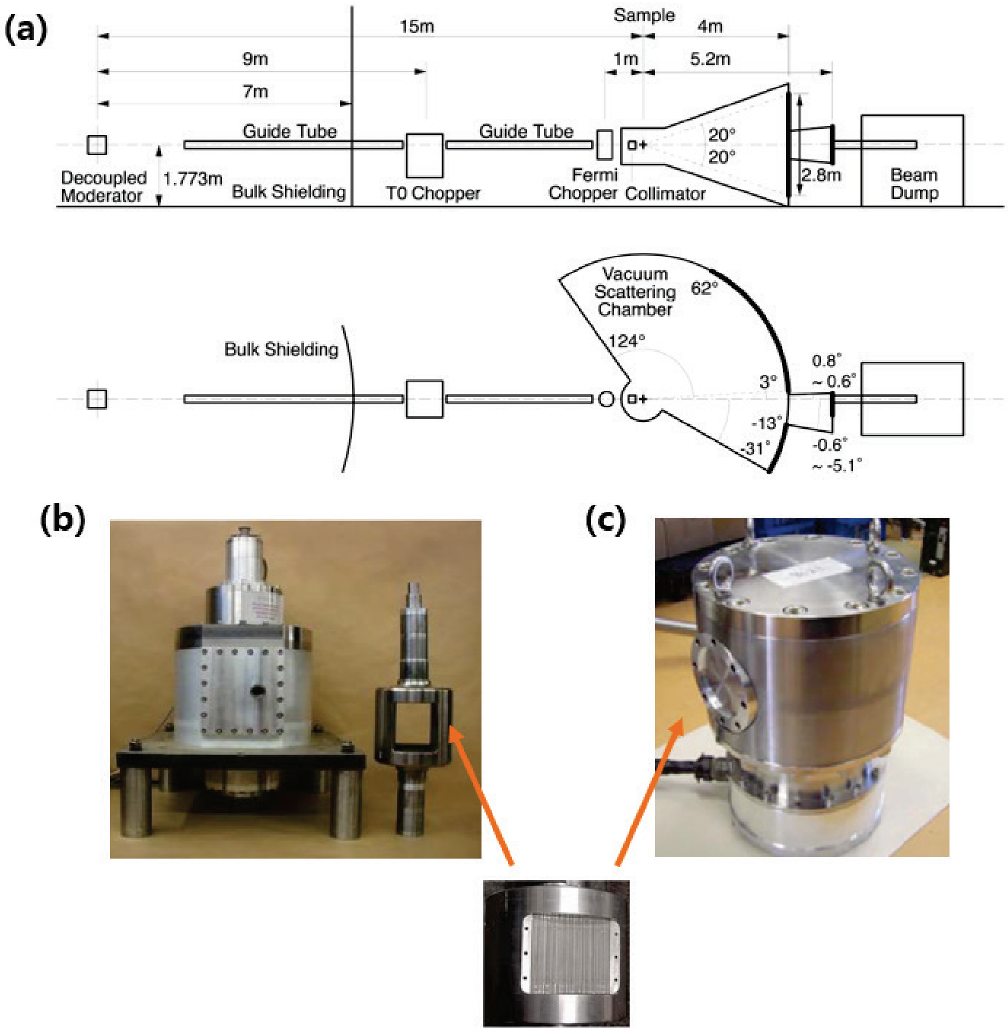

Figure 3.5 Details of the HRC spectrometer. (a) Schematic of the HRC spectrometer. (b) Picture of a typical Fermi chopper used in ISIS, UK [Ref. 3.16]. (c) Curved Fermi chopper installed in the HRC beamline [Ref. 3.17]. The bottom picture shows the slit set installed in both the Fermi choppers.

The INS measurements of single-crystal CoI_2 were performed using the AMATERAS ToF spectrometer in J-PARC, Japan (see Fig. 3.6) [Ref. 3.9]. AMATERAS is a disc-chopper-type spectrometer designed for achieving high-intensity and high-energy resolution at low

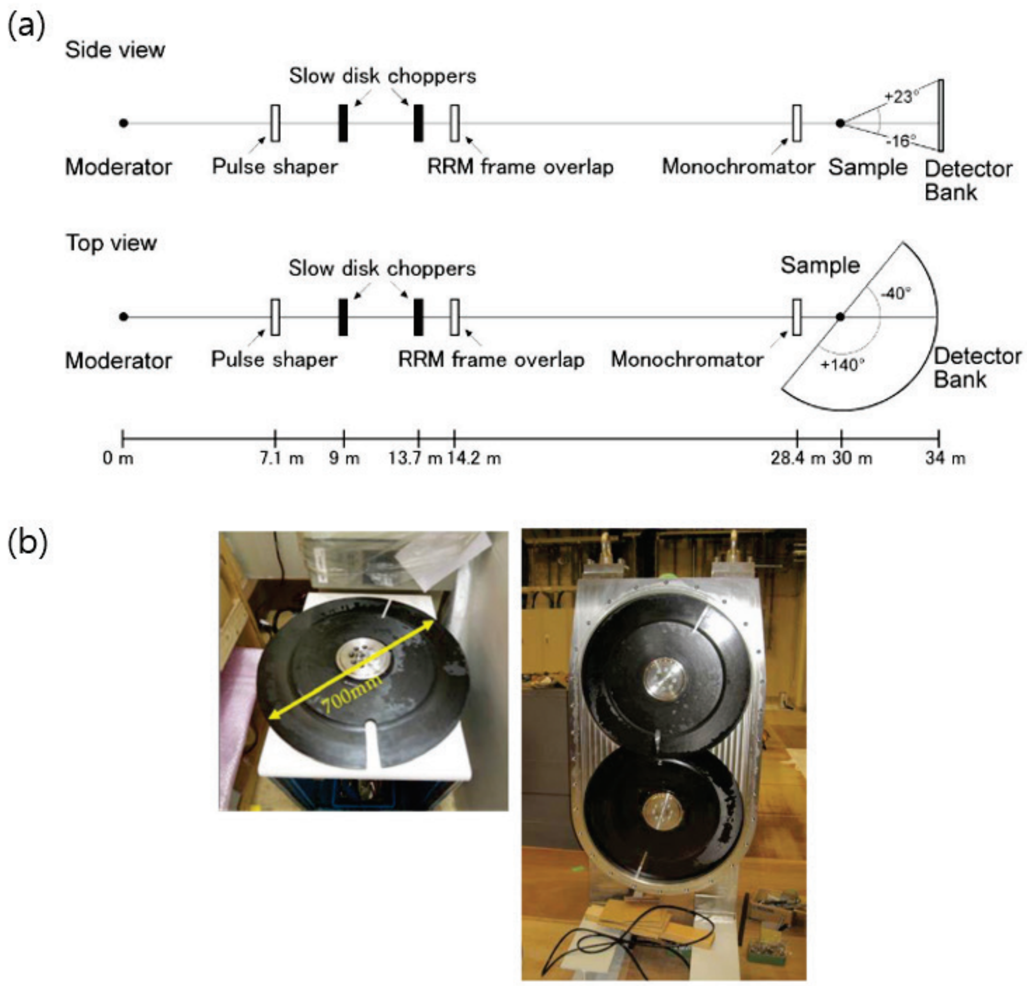

Figure 3.6 Details of the AMATERAS spectrometer. (a) Schematic view of AMATERAS. (b) Installed disc (left) and inside view (right) of the third fast disc chopper (used for monochromatisation) in AMATERAS [Ref. 3.17].

incident energies. Moreover, the AMATERAS beamline provides a high resolution and beams with multiple incident energies and high-resolution profiles in a single measurement.

We prepared a CoI_2 single crystal weighing 5 g for the experiment. Because CoI_2 is exceptionally hygroscopic, the sample has to be coated with the hydrogen-free glue

CYTOP to prevent degradation due to air exposure. The crystal was then securely mounted onto an aluminium holder and sealed using an aluminium can and indium wires for protection. The a-b plane of the crystal was oriented parallel to the horizontal scattering plane. Subsequently, the sample was cooled in a closed-circle refrigerator capable of bottom-loading for measurements at 4 and 13 K (ordered and paramagnetic phases of the sample, respectively). We used three different incident beam energies at the given temperature: E_i = 52.43, 17.26, and 8.48 meV. Our experimental data were obtained using two different configurations: for the 4 K data, and the sample was rotated from -90° to 90° in steps of 0.5°, whereas the angular coverage for the 13 K data was reduced from -90° to 30° in steps of 0.5°. To estimate the broadened magnon energy linewidth and accurately capture the quasi-elastic peaks' characteristics, we performed magnon peak fitting using a Lorentzian function convolved with a Gaussian function.

3.2.5 Multi-E_i measurements at J-PARC beamlines

One problem in the ToF spectrometer with a pulsed neutron source is time inefficiency. Because the frequency of the chopper rotation (f_ch) is usually 100 to 600 Hz, it is typically much faster than the pulsed neutron source f_p = 25 Hz in the J-PARC facility [Ref. 3.10]. Therefore, if we measure a single incident energy, then the utilized ToF region of the INS measurement will be less than 10 % of the period of the pulse source. To overcome this dead-time problem, neutron scientists developed a novel measurement technique called the repetition rate method (RRM) [Ref. 3.11] or Multi-E_i method [Ref. 3.10]. All the ToF spectrometers in J-PARC use this multiple incident energy method to measure multiple incident energies in a single measurement. Notably, the RRM and Multi-E_i methods are slightly different [Ref. 3.10]; in the case of the RRM, more than two choppers are required to prevent contamination of slow neutrons and produce a symmetric pulse shape. The RRM

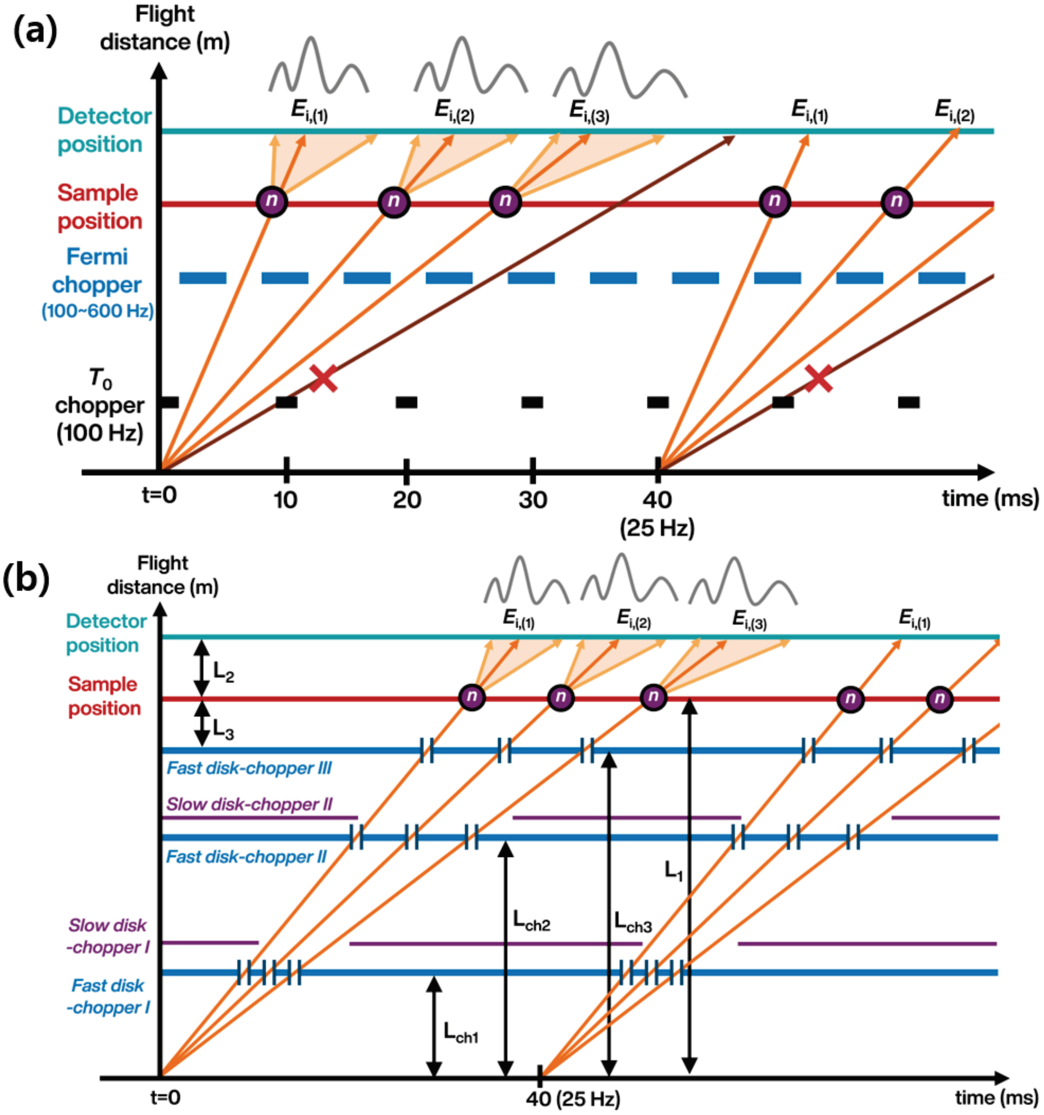

Figure 3.7 Schematic of the RRM set-up in the HRC and AMATERAS. (a) RRM set-up in the HRC using a Fermi chopper. (b) RRM set-up in the AMATERAS using a multiple disc chopper.

is widely used in several ToF beamlines, such as the HRC, AMATERAS, and others in ISIS, UK [Ref. 3.12]. Conversely, the Multi-E_i method uses only one Fermi chopper with straight and wide slits. This remodelled Fermi chopper can exhibit a high transmission of neutrons with a wide E_i range compared to the typical curved ones. This Multi-E_i set-up is installed in the 4SEASONS spectrometer in J-PARC, Japan [Ref. 3.10,3.13].

The RRM set-ups in the HRC and AMATERAS are shown in Fig. 3.7. Because the type of choppers in both the beamlines is different, the ToF diagram for the RRM is also different for these two beamlines. In the case of the HRC, the condition of multiple incident energy is controlled by the frequency ratio of a T_0 chopper and the Fermi chopper. Usually, a T_0 chopper is used to remove high-speed neutrons after the neutron pulse is generated. In the HRC, the T_0 chopper also works as a stopper for slow neutrons and aids in achieving multiple incident energies [Ref. 3.7]. In the AMATERAS, three fast disc choppers and two slow disc choppers cooperate to generate beams with multiple incident energies and high-resolution profiles [Ref. 3.12]. The main disc chopper is the third fast disc chopper, which monochromatizes the neutrons. The other two fast discs, i.e. the first and second discs, work as pulse shapers and tail removers. Slow disc choppers are usually used to prevent frame overlapping or band definition. The possible combinations of incident energies can be simulated at the homepage of each spectrometer [Ref. 3.14].

References

[Ref. 3.1] Hur, N.-J., Journal of the Korean Magnetics Society **21**, 108 (2011).

[Ref. 3.2] Furrer, A., J. Mesot, and T. Strässle, *Neutron Scattering in Condensed Matter Physics*, Vol. 04 (WORLD SCIENTIFIC, 2009).

[Ref. 3.3] Fermi, E., J. Marshall, and L. Marshall, Physical Review **72**, 193 (1947).

[Ref. 3.4] Arnold, O. *et al*., Nucl Instrum Methods Phys Res A **764**, 156 (2014).

[Ref. 3.5] Ewings, R. A. *et al*., Nucl Instrum Methods Phys Res A **834**, 132 (2016).

[Ref. 3.6] Inamura, Y. *et al*., J Physical Soc Japan **82**, SA031 (2013).

[Ref. 3.7] Itoh, S. *et al.*, Nucl Instrum Methods Phys Res A **631**, 90 (2011).

[Ref. 3.8] Itoh, S., K. Ueno, and T. Yokoo, Nucl Instrum Methods Phys Res A **661**, 58 (2012).

[Ref. 3.9] Nakajima, K. *et al.*, J Physical Soc Japan **80**, SB028 (2011).

[Ref. 3.10] Nakamura, M. *et al.*, J Physical Soc Japan **78**, 093002 (2009).

[Ref. 3.11] Russina, M. and F. Mezei, Nucl Instrum Methods Phys Res A **604**, 624 (2009).

[Ref. 3.12] Nakamura, M. *et al.*, Journal of Neutron Research **15**, 31 (2007).

[Ref. 3.13] Kajimoto, R. *et al.*, J Physical Soc Japan **80**, SB025 (2011).

[Ref. 3.14] *Https://Sites.Google.Com/View/t-Nakajima-Group/Tools/Accessible-q-e-Range*.

[Ref. 3.15] Bone, F. *et al.*, *Neutron Scattering and Complementary Experimental Techniques*, in *The ESS Project, Volume II, Chapter 5* (2002).

[Ref. 3.16] Bewley, R. I. *et al.*, Physica B Condens Matter **385–386**, 1029 (2006).

[Ref. 3.17] Sakasai, K. *et al.*, Quantum Beam Science **1**, 10 (2017).

Chapter 4

Magnetic excitation of van der Waals XXZ-type cobalt honeycomb antiferromagnet $CoPS_3$

4.1 Introduction

The $TMPS_3$ family, comprising Mn, Fe, Co and Ni, has drawn particular attention as a class of antiferromagnetic two-dimensional van der Waals (vdW) materials [Ref. 4.1]. In this family, 2+ covalent transition metal ions form a layered honeycomb lattice with sulphur ligand ions. All the elements have the same monoclinic structure with the space group C 2/m, where layers on the *ab*-plane are weakly coupled along the *c*-axis [Ref. 4.1,4.2]. Owing to the dependence of the magnetic structure and exchange interactions on transition metal (TM) elements, this family offers an excellent platform to experimentally validate the spin dynamics theory in low dimensions [Ref. 4.3]. For example, $FePS_3$ is an ideal Ising antiferromagnet [Ref. 4.4,4.5], while $MnPS_3$ and $NiPS_3$ are examples of the Heisenberg model [Ref. 4.4,4.6,4.7]. Among these materials, $NiPS_3$ exhibits a magnetic order close to the XY-type [Ref. 4.8]. Furthermore, extensive research has been conducted on the influence of their thickness on their physical and magnetic properties [Ref. 4.9].

Compared to other $TMPS_3$ materials, $CoPS_3$ has received less attention due to challenges in synthesizing high-purity samples [Ref. 4.10]. Below the Néel temperature (T_N) of 120 K, $CoPS_3$ exhibits antiferromagnetic order and a zig-zag magnetic structure with the propagation vector $Q_m = (0,1,0)$, as depicted in Fig. 4.1. The spins of the Co sites are

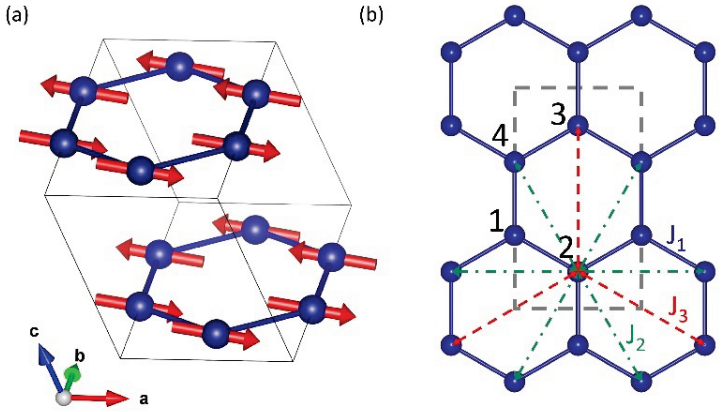

Figure 4.1 (a) Magnetic structure of $CoPS_3$. Red arrows indicate the spin of Co^{2+} ion. (b) Exchange interaction path of Co^{2+} ions in $CoPS_3$.

primarily aligned along the *a*-axis with a slight canting towards the *c*-axis [Ref. 4.10]. The magnetic susceptibility of $CoPS_3$ exhibits a difference between H//ab and H//c in the paramagnetic region, demonstrating XY-like anisotropy and signifying the presence of anisotropic magnetic interactions that depend on the magnetic moment direction [Ref. 4.10].

The underlying spin Hamiltonian needs to be analyzed to understand the magnetism in $CoPS_3$ comprehensively. Although the magnetic structure provides some information about the spin Hamiltonian, it is insufficient for accurately determining it. For example, the magnetic ground states of the XY model ($J_x = J_y$, $J_z = 0$) and the isotropic Heisenberg model ($J_x = J_y = J_z$) with easy-plane anisotropy can be the same. However, their magnon spectra cannot be assumed identical, as their Hamiltonians have different symmetries. To determine the type of spin Hamiltonian and the strength of the exchange interactions, inelastic neutron scattering (INS) is the most powerful technique for measuring spin dynamics. Using INS, the existence of the spin-orbital entangled $J_{\mathrm{eff}} = 1/2$ state can be determined by observing the excitation from the $J_{\text{eff}} = 1/2$ to $J_{\text{eff}} = 3/2$ states; it should appear around 20–30 meV and is considered as the characteristic signature of the J_{eff} = 1/2 ground state in cobalt compounds [Ref. 4.11–4.13].

4.2 Magnetic excitations of $CoPS_3$

4.2.1 Absence of spin-orbit exciton

Fig. 4.2 displays the temperature-dependent magnon dispersion with an incident neutron energy of $E_i = 71.3$ meV. The phonon contamination was removed from the data using the technique used to analyze the 8 K data. As illustrated in Fig. 4.2(a–f), the intensity of the magnon modes gradually decreases with increasing temperature and dramatically decreases near the Néel temperature T_N = 120 K. However, no other excitations above the Néel temperature were observed in our data, such as the dispersionless spin-orbit excitons corresponding to the transition from the $J_{\text{eff}} = 1/2$ state to the $J_{\text{eff}} = 3/2$ state. This excitation

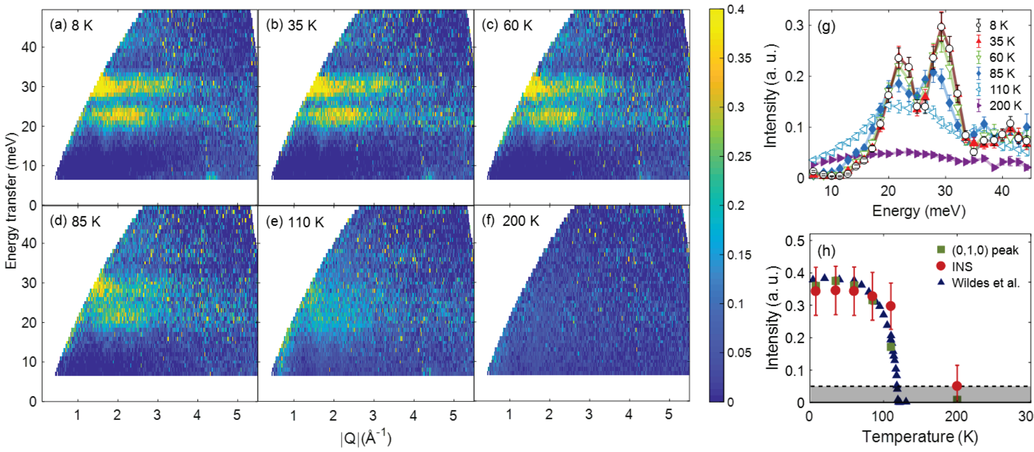

Figure 4.2 (a–f) Temperature dependence of the magnetic excitation in $CoPS_3$. (g) Integrated intensity of magnetic excitations over the momentum range of Q = [0.3, 4] $Å^{-1}$ with temperature. (h) Overall integrated magnon intensity and (0,1,0) elastic peak for the given temperatures. The blue triangles depict the integrated intensity of the (0,1,0) magnetic peak in [Ref. 4.10], the red circles depict the magnon spectrum, and the green squares depict the (0,1,0) magnetic peak of our data.

stems from crystal field splitting, so it should remain above the Neel temperature. The absence of such excitations indicates that $CoPS_3$ has a spin $S = 3/2$ ground state instead of the spin-orbital entangled $J_{\mathrm{eff}} = 1/2$ ground state. Thus, the interaction between spin waves and spin-orbit coupling, such as the multi-level spin-wave theory, typically employed to mix spin-orbit levels or Kitaev interaction, does not apply to this system. Therefore, in the subsequent analysis, $CoPS_3$ is considered as a spin $S = 3/2$ state in the conventional linear spin-wave theory calculation.

4.2.2 Spin-wave spectrum

Fig 4.3 presents the spin waves observed at 8 K using an incident neutron energy of $E_i =$ 71.3 meV and the corresponding linear spin-wave theory calculations. The experimental data demonstrate dispersive magnons with a significant spin gap of approximately 13 meV. Additionally, another gap is present around 25 meV, leading to two magnon modes: a flat upper band and a lower dispersive band.

Previous studies on honeycomb lattice systems have predominantly employed isotropic Heisenberg models. However, for $CoPS_3$, this model is inadequate, and thus, an XXZ-type (anisotropic Heisenberg) Hamiltonian with a single-ion anisotropy is employed in this study:

$$\mathrm{H} = \sum_{n=1}^{3} J_n \sum_{<i,j>_n} \left[\boldsymbol{S}_i^x \boldsymbol{S}_j^x + \boldsymbol{S}_i^y \boldsymbol{S}_j^y + \alpha \boldsymbol{S}_i^z \boldsymbol{S}_j^z \right] + K \sum_i (\hat{x} \cdot \boldsymbol{S}_i)^2, \quad (1)$$

where $\alpha \in [0,1]$ is an anisotropy factor that spans from the *XY* model ($\alpha = 0$) to the isotropic Heisenberg model ($\alpha = 1$), K is the easy-axis single-ion anisotropy, and J_n is the strength of the exchange interaction till the third nearest neighbours. The inter-layer interaction is neglected in the analysis due to the weak vdW force. To determine the spin-wave dispersion

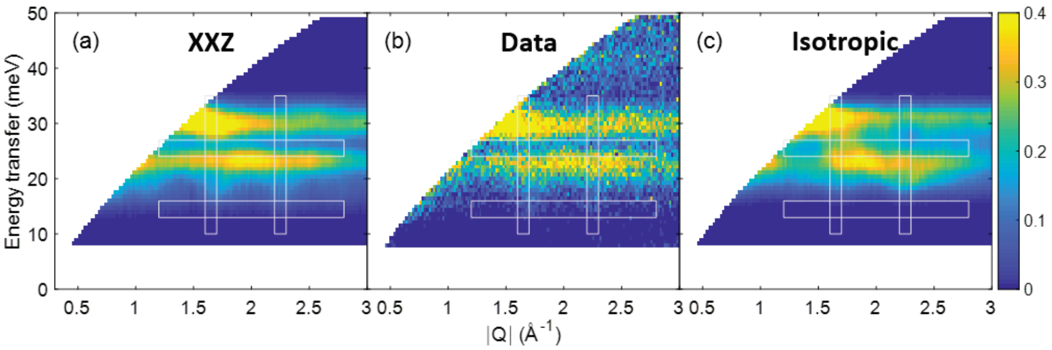

Figure 4.3 (a) Best-fit powder-averaged spin-wave spectrum with the XXZ model. (b) Experimental INS data of $CoPS_3$ (c) Best-fit magnon spectra with the isotropic Heisenberg model.

and powder-averaged neutron cross-section, both the SpinW package and our own analytical solutions are employed. The analysis is limited to the data up to Q = 2.5 Å^{-1}, and the elastic scattering below E = 8 meV is excluded. The particle swarm optimization algorithm is used to obtain the best fit, which is well suited for searching the global minima in large parameter spaces.

The simulated powder-averaged INS cross-section for the XXZ-type and isotropic Heisenberg models are presented in Fig. 4.3(a) and 4.3(c), using the best-fit parameters and convoluting with an instrumental resolution of 3 meV. The best-fit parameters of the XXZ-type Heisenberg model signify the ferromagnetic exchange interactions for the first and second nearest neighbours, $J_1 = -2.08$ meV and $J_2 = -0.26$ meV, respectively, and a significant antiferromagnetic third nearest neighbour exchange interaction, $J_3 = 4.21$ meV. In addition, a strong easy-axis single-ion anisotropy $K = -2.06$ meV and a planar-type spin anisotropy factor $\alpha = J_z/J_x$ (0.6) are necessary to account for the large lower spin gap observed in the experiments. Moreover, the best-fit parameters of the isotropic Heisenberg model exhibit the same sign for the exchange parameters as the XXZ model but with

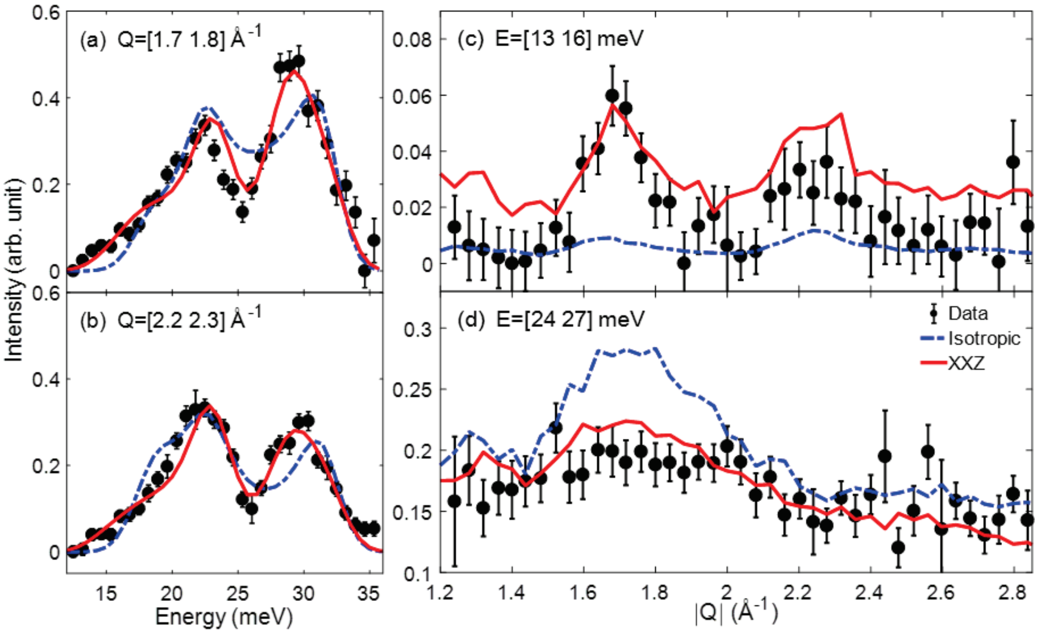

Figure 4.4 (a,b) Constant momentum cut in the range of Q = [1.7 1.8] and Q = [2.2 2.3] Å^{-1} for the measured data with the best fit simulations. (c,d) Constant energy cut in the range of E = [13 16] and E = [24 27] meV.

slightly different values: $J_1 = -2$, $J_2 = -0.65$, $J_3 = 3.51$ and $K = -3.62$ meV. The other key difference is the expression of the spin gaps at the zone centre. The spin gaps for the isotropic Heisenberg model (E_{iso}) and the XXZ-like model (E_{XXZ}) are as follows:

$$E_{iso} = 2S\sqrt{-K(-K + J_1 + 4J_2 + 3J_3)},$$

$$E_{XXZ} = 2S\sqrt{-K\left(-K + \frac{3\alpha - 1}{2}J_1 + (3\alpha + 1)J_2 + \frac{3\alpha + 3}{2}J_3\right)},$$

Fig. 4.4 comprehensively compares the XXZ-type and isotropic Heisenberg models by plotting the constant momentum and energy cuts integrated over specific ranges. As shown in Fig. 4.4(a) and 4.4(b), the isotropic Heisenberg model does not match the observed low energy gap and the additional gapped spectra at 24–27 meV. The best-fit single-ion anisotropy parameter of K = −3.62 meV overestimates the low energy gap for the isotropic model. This inconsistency is further highlighted in Fig. 4.4(c), wherein the isotropic Heisenberg model predicts a very low intensity in the energy range from 13 to 16 meV around Q = 1.7 and 2.2 Å^{-1}. In contrast, it predicts significant intensity between 24 and 27 meV. In contrast, the INS and the simulation data from the XXZ model exhibit the gapped feature in the same energy range.

A considerable fraction of the initial spectral weights persists above the Neel temperature due to over-damped spin waves from the critical fluctuations, as depicted in Fig. 4.2(a–f). To better illustrate this observation, the temperature dependence of the integrated intensity is displayed across the extensive range of Q = 0.3–4 Å^{-1} in Fig. 4.2(g and h), wherein the contributions arising from the high-temperature spin fluctuations are depicted as the shaded area.

4.3 Discussion

Fig. 4.5 illustrates the anticipated dispersion of $CoPS_3$ spin waves with the high symmetry directions in the Brillouin zone using the most suitable parameters for the isotropic Heisenberg and XXZ models obtained through the best-fit approach. Due to the spin anisotropy, the magnon branches in the XXZ model are split more than those in the isotropic Heisenberg model. Additionally, most magnon modes in the XXZ model are divided into two parts, yielding a different spin gap at 24–27 meV, as shown in Fig. 4.3(a). Furthermore, except for C–Y, the number of magnon branches over the high symmetry lines in the XXZ model is double, indicating the absence of mode degeneracy for most positions in the momentum space. The non-degenerated magnon branch with the lowest energy at 14 meV well corresponds to the measured low-energy gap.

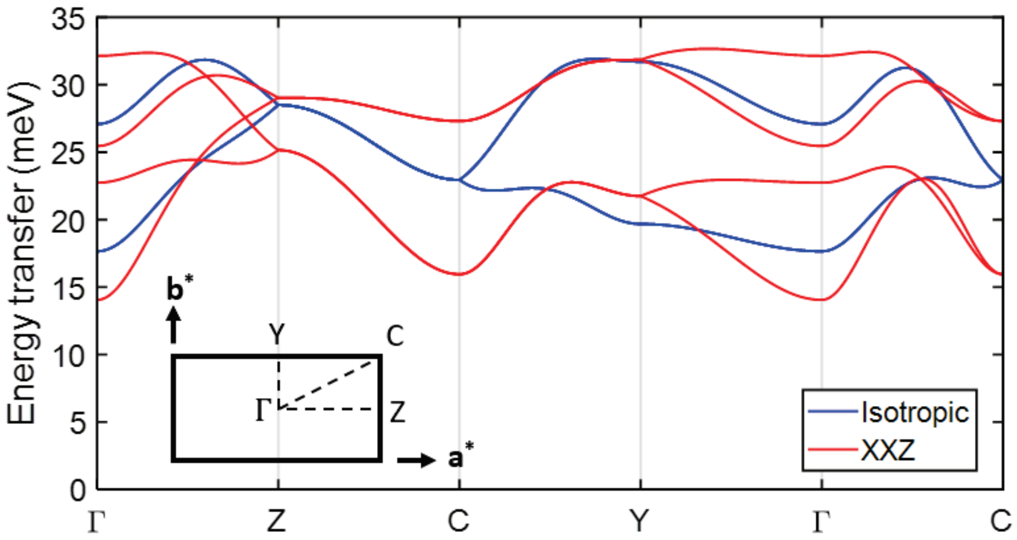

Figure 4.5 The spin-wave dispersion of the isotropic Heisenberg model and the XXZ model, indicating the high-symmetric points of the Brillouin zone. The spin-wave trajectories are displayed for the crystallographic unit cell, while the relevant positions and the Brillouin zone are presented in the insert.

Table 4.1 summarises the magnetic exchange parameters experimentally measured for the TMPS$_3$ family like CoPS$_3$, using the self-consistent method defined in Eq. (1) [Ref. 4.5–4.7]. Although the TMPS$_3$ family has the same crystal structure and similar antiferromagnetic order, the parameters significantly vary depending on the magnetic TM ion. Additionally, the second nearest neighbour exchange interaction is generally small for all TMPS$_3$, consistent with the density functional theory calculations [Ref. 4.14].

Next, the best-fit parameters are examined by considering the magnetic properties. Using the mean-field theory, the Neel temperature T_N and the Curie–Weiss temperature Θ_{CW} are estimated as follows:

	$MnPS_3$	$FePS_3$	$CoPS_3$ (this work)	$NiPS_3$
S	5/2	2	3/2	1
T_N (K)	78	120	120	155
J_1 (meV)	1.54	−2.96	−2.04	−3.8
J_2 (meV)	0.14	0.08	−0.26	0.1
J_3 (meV)	0.36	1.92	4.21	13.8
α	1	∞	0.6	1
K (meV)	−0.0086	−2.66	−2.06	−0.3
θ (°)	51.67	51.28	51.38	51.05

Table 4.1 Summary of the magnetic exchange parameters of the magnetic vdW *TM*PS_3 (TM = Mn, Fe, Co, Ni) family. The angle between the c* axis and the vector that joins the TM ion and sulphur ligand is defined as θ. θ is 54.7° for an ideal octahedron.

$$k_B\Theta_{CW} = -\frac{1}{3}S(S+1)(3J_1 + 6J_2 + 3J_3),$$

$$k_B T_N = -\frac{1}{3}S(S+1)(J_1 - 2J_2 - 3J_3).$$

The temperatures obtained using our best-fit parameters are $\Theta_{CW} = -43.5$ K and $T_N = 188.5$ K. Considering the overestimation of T_N from the mean-field theory in a low-dimensional system, these values are in good agreement with the reported value of $\Theta_{CW} = -35.4$ K [Ref. 4.10] and $T_N = 120$ K. Moreover, this parameter set also stabilizes the zig-zag magnetic order. Hence, the obtained results further verify that the obtained parameters are rational and consistent with the magnetic properties of the bulk sample.

The electronic ground state of $CoPS_3$ is an interesting aspect to consider. While many cobalt compounds exhibit a flat-like spin-orbit exciton, $CoPS_3$ does not [Ref. 4.11–4.13]. The local environment of Co^{2+} in $CoPS_3$ is a distorted octahedron, similar to that of other cobalt compounds. The main difference between $CoPS_3$ and other cobalt compounds is the type of ligand used, which for $CoPS_3$ is sulphur. Therefore, the absence of the spin-orbital entangled state in $CoPS_3$ could be due to the physical effect of sulphur, such as the charge-transfer effect [Ref. 4.15]. Notably, in $NiPS_3$, different charge-transfer physics have been found to yield novel phenomena called spin-charge coupling and quantum-entangled magnetic exciton [Ref. 4.15,4.16].

The planar type of spin anisotropy in $CoPS_3$ stems from the electronic configuration of Co^{2+} within a trigonally distorted octahedron. Table 4.1 shows that each $TMPS_3$ compound has a distinct spin-anisotropy factor α. However, the angle θ, denoting the strength of trigonal distortion in the *TM*PS_3 family, remains relatively consistent at 51°. The only difference is the type of *TM* element present, which leads to variations in the electronic configuration and occupancy of orbital states. These factors influence the super-exchange process between *TM*s, thereby impacting the origin of the easy-plane spin anisotropy, which is closely tied to the electronic configuration of Co^{2+} and the orbital splitting induced by the trigonal distortion.

4.4 Summary

Powder INS was used to determine the magnetic exchange parameters and the single-ion anisotropy of $CoPS_3$. The results show that Co^{2+} in $CoPS_3$ possesses a spin $S = 3/2$ state rather than a spin-orbital entangled $J_{\mathrm{eff}} = 1/2$ ground state. The anisotropic XXZ-type J_1–J_2–J_3 Heisenberg Hamiltonian was used to fit the magnon spectra, which signified a significant easy-axis single-ion anisotropy of the S = 3/2 state. Our best-fit analysis demonstrated the presence of the ferromagnetic exchange interactions J_1 and J_2 and an antiferromagnetic J_3 exchange interaction for the first, second and third nearest neighbours in the XXZ model. Moreover, an XXZ-type interaction was observed in a honeycomb lattice with an easy-plane spin anisotropy of $\alpha = 0.6$, which signifies that $CoPS_3$ is an XXZ-type honeycomb antiferromagnet. The analysis also showed a large spin gap of ~13 meV, which requires a sizable single-ion anisotropy of $K = -2.06$ meV. Overall, $CoPS_3$ presents an excellent opportunity for exploring low-dimensional magnetism with magnetic vdW materials.

References

[Ref. 4.1] Brec, R., Solid State Ion **22**, 3 (1986).

[Ref. 4.2] Ouvrard, G., R. Brec, and J. Rouxel, Mater Res Bull **20**, 1181 (1985).

[Ref. 4.3] Burch, K. S., D. Mandrus, and J. G. Park, Nature **563**, 47 (2018).

[Ref. 4.4] Joy, P. A. and S. Vasudevan, Phys Rev B **46**, 5425 (1992).

[Ref. 4.5] Lançon, D. *et al.*, Phys Rev B **94**, 214407 (2016).

[Ref. 4.6] Wildes, A. R. *et al.*, Journal of Physics: Condensed Matter **10**, 6417 (1998).

[Ref. 4.7] Lançon, D. *et al.*, Phys Rev B **98**, 134414 (2018).

[Ref. 4.8] Kim, K. *et al.*, Nat Commun **10**, 345 (2019).

[Ref. 4.9] Kuo, C.-T. *et al.*, Sci Rep **6**, 20904 (2016).

[Ref. 4.10] Wildes, A. R. *et al.*, Journal of Physics: Condensed Matter **29**, 455801 (2017).

[Ref. 4.11] Wallington, F. *et al.*, Phys Rev B **92**, 125116 (2015).

[Ref. 4.12] Tomiyasu, K. *et al.*, Phys Rev B **84**, 054405 (2011).

[Ref. 4.13] Sarte, P. M. *et al.*, Phys Rev B **98**, 224410 (2018).

[Ref. 4.14] Chittari, B. L. *et al.*, Phys Rev B **94**, 184428 (2016).

[Ref. 4.15] Kim, S. Y. *et al.*, Phys Rev Lett **120**, 136402 (2018).

[Ref. 4.16] Kang, S. *et al.*, Nature **583**, 785 (2020).

Chapter 5

Spin dynamics of cobalt Kitaev honeycomb candidates $Na_3Co_2SbO_6$ and $Na_2Co_2TeO_6$

5.1 Introduction

Bond-dependent anisotropic interactions rely on the entanglement of the spin and orbital sectors. Therefore, most research has been dedicated to the 4*d*- and 5*d*-electron systems with strong spin-orbit coupling (SOC), such as Na_2IrO_3 [Ref. 5.1]and α-$RuCl_3$ [Ref. 5.2], which exhibit ferromagnetic (FM) Kitaev interactions. However, realising Kitaev quantum spin liquids (KQSLs) has been challenging. This is because a long-range magnetic order inevitably emerges at higher temperatures due to non-negligible Heisenberg interactions for all candidates. Furthermore, although several systems with FM Kitaev interactions have been experimentally discovered [Ref. 5.2,5.3], no antiferromagnetic (AFM) Kitaev systems have been reported. Of further interest, recent theories predict that AFM Kitaev materials can stabilise new classes of KQSL owing to the $U(1)$ gauge field. FM Kitaev systems only have the usual Z_2 gauge field [Ref. 5.4]. Therefore, it is essential to find AFM Kitaev materials.

$Na_3Co_2SbO_6$ (NCSO) and $Na_2Co_2TeO_6$ (NCTO) are honeycomb-layered cobaltates that have been theoretically proposed as KQSL candidates [Ref. 5.5,5.6]. NCSO and NCTO possess a honeycomb layer of edge-sharing CoO_6 octahedra with SbO_6 and TeO6 octahedra located at the honeycomb centre, respectively (Fig. 5.1). Both materials exhibit zig-zag magnetic ordering, with NCSO having a Neel temperature of $T_N = 8$ K and a magnetic

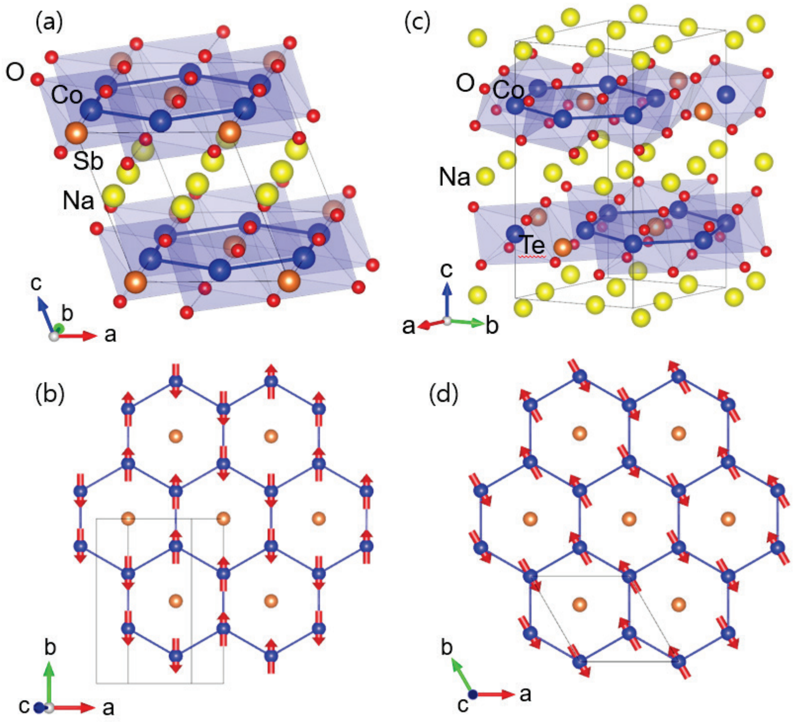

Figure 5.1 (a–b) Crystal structure of $Na_3Co_2SbO_6$ and its magnetic structure. (c–d) Crystal structure of $Na_2Co_2TeO_6$ and its magnetic structure

propagation vector of $Q_m = (1/2, 1/2, 0)$ [Ref. 5.6,5.7] and NCTO having $T_N = 27$ K and $Q_m = (1/2, 0, 0)$ [Ref. 5.5,5.8]. To experimentally verify the theoretically proposed KQSL, the strength and sign of the Kitaev coupling and non-Kitaev interactions need to be determined. This information will enable the exploration of novel ways for realising the KQSL phase by tuning external parameters.

5.2 Magnetic excitations of NCSO and NCTO

5.2.1 Spin-orbit exciton

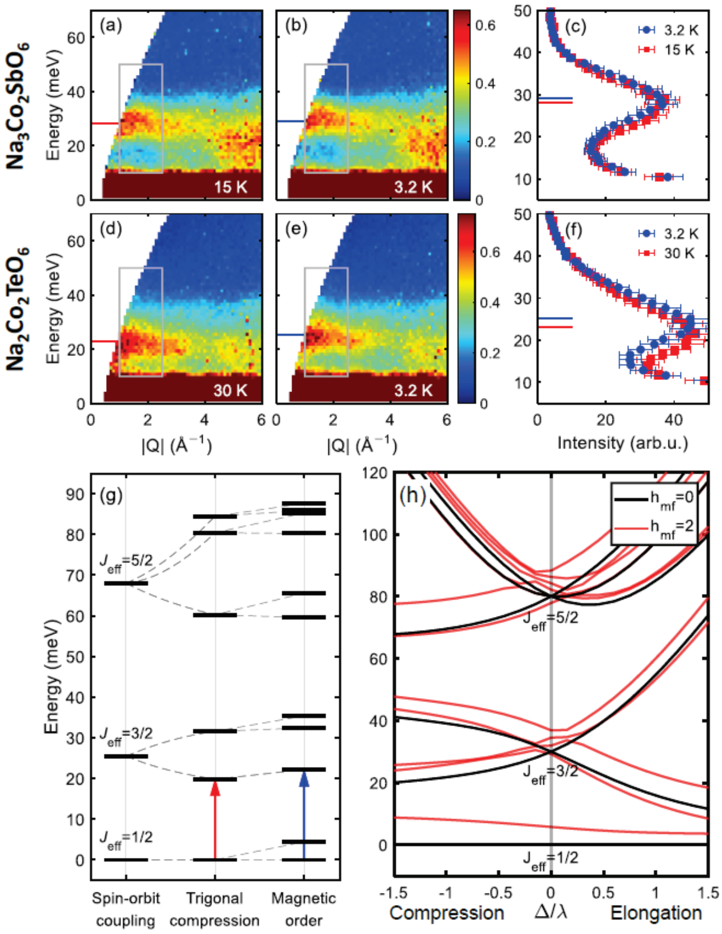

Figure 5.2 The spin-orbit exciton of (a-c) $Na_3Co_2SbO_6$ and (d-f) $Na_2Co_2TeO_6$ with respect to the temperature. Constant-Q cuts in (c,f) is integrated intensity of grey boxes in (a,b,d,e). (g) Deviation of the spin-orbital entangled states by trigonal distortion and magnetic order. (h) Splitting of crystal field levels with function of trigonal distortion (black) and finite effective zeeman field from magnetic order (red).

Spin-orbit excitons, excitation between the $J_{\mathrm{eff}} = 1/2$ ground state and excited states, are commonly observed for cobalt compounds supporting the spin-orbit-entangled state for Co^{2+} ions [Ref. 5.9,5.10]. In the presence of a trigonal distortion of octahedra, the excited $J_{\mathrm{eff}} = 3/2$ state splits into two levels, and the lowest exciton energy stems from the interplay

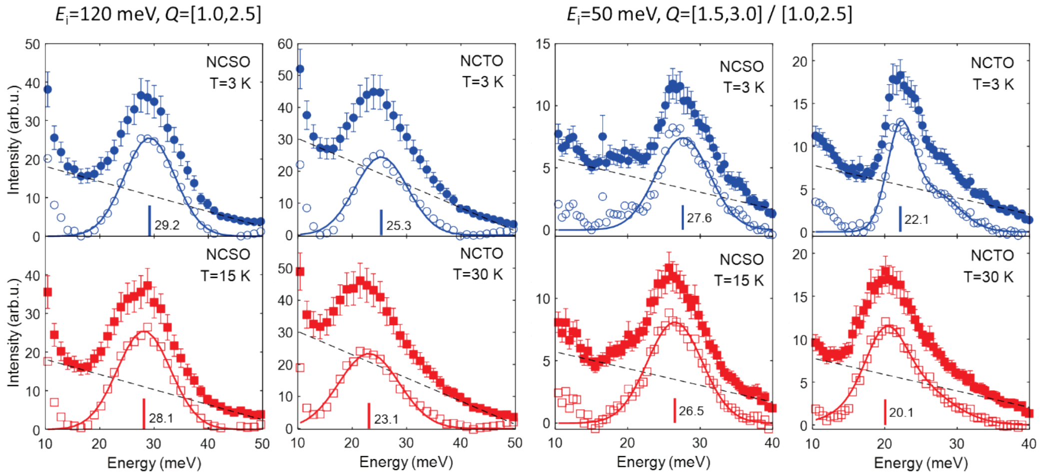

Figure 5.3 Peak profiles of the spin-orbit excitons. The parameter set from fitting was used for the crystal field analysis.

between SOC (λ) and trigonal crystal field (Δ). The temperature-dependent behaviour of spin-orbit excitons in NCSO and NCTO is shown in Fig. 5.2. The energy of the exciton for NCSO is observed to be 28.1 meV (above T_N), and its position slightly increases by 1.1 meV below T_N. Similarly, for NCTO, the energy of the exciton is located at 23.1 meV and shifts to 25.3 meV upon entering the magnetic ordering. The energy shift of the spin-orbit exciton through T_N can be attributed to the Zeeman splitting caused by the molecular field of the magnetic order, as illustrated in Fig. 5.2(g). The data obtained at $\mathrm{E_i} = 50$ and 100 meV are used to determine the exciton energy, as shown in Fig. 5.3. To accurately understand the shift of this spin-orbit excitation, the following single-ion Hamiltonian is used:

$$H = H_{\mathrm{SO}} + H_{\mathrm{tri}} + H_{MF} = \lambda L \cdot S + \Delta\left(L_{\hat{n}}^2 - \frac{2}{3}\right) + h_{\mathrm{mf}} S_{\hat{b}}\ ,$$

where λ indicates the SOC strength, Δ is the crystal electric field from the trigonal distortion, and h_mf denotes the effective Zeeman field from the zig-zag magnetic order. Note that the

$\hat{n}$ vector is given along the [1 1 1] direction for the local frame. The parameters in the Hamiltonian can be experimentally determined by measuring various crystal field excitations, as shown in Fig. 5.3. A magnetic ordering induces a change in the transition energy through the molecular magnetic field, exhibiting a clear difference based on the Δ sign. Specifically, for $\Delta > 0$, the energy of the lowest spin-orbit exciton increases upon the onset of magnetic ordering. Conversely, for $\Delta < 0$, it splits into two modes, with the lower one slightly shifting towards lower energies (Fig. 5.2(h)). The positive energy shift observed in the data indicates that both our samples have a positive sign of trigonal distortion. The optimal fitting of the observed energy shift can be achieved with $\lambda = 25$ meV, $\Delta = 12$ meV and $h_{mf} = 0.4$ meV for NCSO and $\lambda = 21$ meV, $\Delta = 13$ meV and $h_{mf} = 0.6$ meV for NCTO.

5.2.2 Spin-wave spectrum

The magnon spectra of NCSO and NCTO are measured at $T = 3$ K with a neutron incident energy of $E_i = 16.54$ meV; the results are shown in Fig. 5.4(a–b). To eliminate the effect of the background and phonon contamination, the high-temperature data obtained well above T_N are employed: 50 K for NCSO and 95 K for NCTO. Although NCSO and NCTO have similar atomic and magnetic structures, their magnon dispersions exhibit striking differences. In NCSO, a pronounced upturn-shaped dispersion is observed at low $Q < 1$ Å^{-1} and E ~ 1–3 meV, accompanied by a small gap of 0.6 meV. In contrast, the high energy data display a weak arch-shaped dispersion that persists up to 8 meV. Conversely, NCTO exhibits a flat excitation at ~7 meV and strong triangular-like dispersions below ~3 meV with a gap of 0.4 meV.

To explain the spin-wave spectrum, the generalised Kitaev–Heisenberg (GKH) Hamiltonian with pseudospin a $\tilde{S} = 1/2$ is used:

$$
\begin{aligned}
H = \sum_{n=1,3} J_n \sum_{<i,j>_n} \tilde{\boldsymbol{S}}_i \cdot \tilde{\boldsymbol{S}}_j \\
&+ \sum_{<i,j>\in\alpha\beta(\gamma)} \Big[K\tilde{S}_i^\gamma \tilde{S}_j^\gamma + \Gamma\left(\tilde{S}_i^\alpha \tilde{S}_j^\beta + \tilde{S}_i^\beta \tilde{S}_j^\alpha\right) \\
&+ \Gamma'\left(\tilde{S}_i^\alpha \tilde{S}_j^\gamma + \tilde{S}_i^\gamma \tilde{S}_j^\alpha + \tilde{S}_i^\beta \tilde{S}_j^\gamma + \tilde{S}_i^\gamma \tilde{S}_j^\beta\right)\Big], \qquad \ldots(1)
\end{aligned}
$$

where J_n is a Heisenberg interaction between the nth nearest neighbours, K is a Kitaev interaction, and Γ/Γ’ denotes a symmetrically allowed off-diagonal interaction. For the first nearest neighbour bonding, an easy-axis γ can be distinguished, with the bond labelled $\alpha\beta(\gamma)$. In the analysis, only the first and third nearest-neighbour Heisenberg interactions are considered since it is widely acknowledged that the second nearest-neighbour interaction is generally small in honeycomb compounds.

To validate the GKH model, comparisons are performed with a simple anisotropic Heisenberg (XXZ) model. The XXZ model is frequently utilised to describe the spin dynamics of cobalt honeycomb compounds. For consistency with the reported magnetic

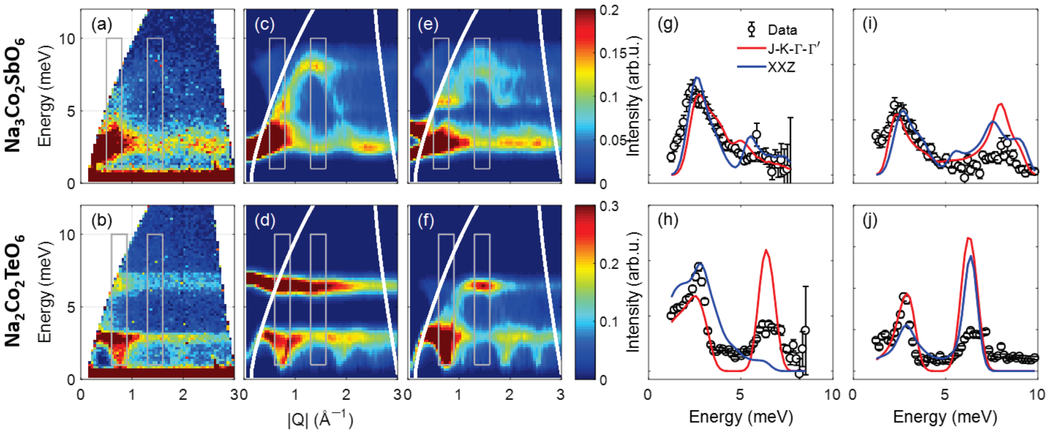

Figure 5.4 (a–b) Spin-wave spectrum of NCSO and NCTO at T = 3.2 K. (c–d) Simulated powder-averaged spectrum with the generalized Kitaev–Heisenberg model. (e–f) Simulated with the XXZ model. (g–h) Constant Q cuts with left grey boxes in (a–f). (i–j) Constant Q cuts with right grey boxes in (a–f)

structure and spin gap, ‘phenomenological’ single-ion anisotropy is introduced to the XXZ model to ensure the alignment of spins orthogonal to the propagation vector. The XXZ model used herein is

$$\mathrm{H} = \sum_{n=1,3} J_n \sum_{<i,j>_n} \left[\boldsymbol{S}_i^x \boldsymbol{S}_j^x + \boldsymbol{S}_i^y \boldsymbol{S}_j^y + \alpha \boldsymbol{S}_i^z \boldsymbol{S}_j^z \right] + D \sum_i (\hat{e} \cdot \boldsymbol{S}_i)^2 \ ,$$

where $\alpha \in [0, 1]$ is the anisotropy factor between the in-plane and out-of-plane directions, D is the easy-axis single-ion anisotropy, and J_n is the Heisenberg interaction with the first and third nearest neighbours. $\hat{e}$ is a unit vector orthogonal to the propagation vector. The best-fitting parameters are as follows: for NCSO $J_1 = -3.6$, $J_3 = 1.9$, $\alpha = 0.8$ and $D = -0.7$ meV; for NCTO $J_1 = -2.1$, $J_3 = 2.1$, $\alpha = 0.95$ and $D = -0.1$ meV.

The optimal parameters for our models are determined by conducting an extensive search in the parameter space, as summarised in Table 5.1. The resulting powder-averaged magnon spectra, calculated using Eq. (1) with the optimal parameters, are shown in Fig. 5.4(c and d) for NCSO and NCTO, respectively. The optimal parameters for the anisotropic Heisenberg (XXZ) Hamiltonian with a single-ion anisotropy term are also determined, which support the reported magnetic structure and the magnon gap, as shown in Fig. 5.4(e and f). A detailed comparison between the two models is conducted by employing constant Q cuts integrated over the Q range, as indicated by the vertical boxes in Fig. 5.4(a–d). As depicted in Fig. 5.4(g–j), the GKH model exhibits the best agreement with an AFM Kitaev coupling of several meV. Although the simpler XXZ model reproduces some of the basic shapes of the measured dispersions, it lacks consistency in the detailed features. Thus, the GKH model is the most suitable for both systems.

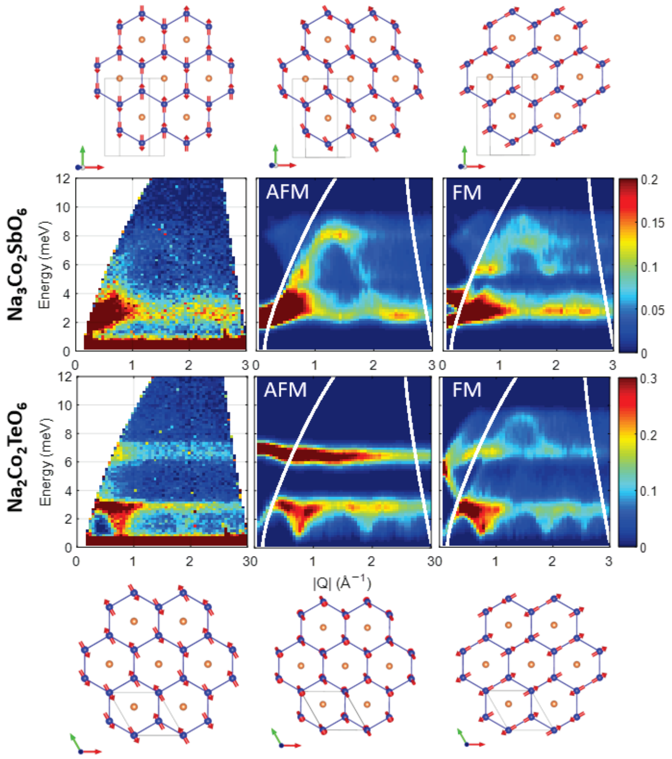

Figure 5.5 Comparison of the measured spin-wave (left) and simulated powder-averaged spectrum with the AFM and FM Kitaev models (right).

Based on recent theoretical predictions [Ref. 5.11,5.12], the possibility of an FM Kitaev coupling (K<0) as an alternative model is investigated for the observed spin-wave spectra. Fig. 5.5 illustrates the computed powder-averaged spin-wave spectra and the optimised magnetic structures using the best-fitting FM Kitaev parameters for NCSO and NCTO.

Although the FM Kitaev model seems to provide a similar degree of agreement

Table 5.1 Best parameter set with the GKH model

	J_1 (meV)	J_3 (meV)	K (meV)	Γ (meV)	Γ' (meV)
NCSO	−4.70(5)	0.95(1)	3.60(4)	1.30(5)	−1.40(4)
NCTO	−1.50(5)	1.50(2)	3.30(10)	−2.80(5)	2.10(7)

with the data as the AFM Kitaev model, the magnetic structures optimised for each model within the spin-wave calculations differ, particularly in the direction of the magnetic moments. For NCTO, the optimised magnetic structures of the AFM and FM Kitaev models do not precisely match the reported data. Still, the magnetic structures obtained with the AFM Kitaev model are much closer to the reported data than that obtained with the FM Kitaev model [Ref. 5.5]. On the other hand, for NCSO, the calculated magnetic structure of our parameter set exhibits excellent agreement with the reported neutron diffraction data [Ref. 5.7]. However, the optimised magnetic structure of our parameter set with NCTO has an additional out-of-plane canting, which is absent in the reported neutron diffraction data.

5.2.3 Magnon damping effect

Although the AFM Kitaev model employed herein captures the essential characteristics of the measured magnon spectra, it overestimates the intensity at high energies. Furthermore, a similar phenomenon of damped magnon dispersions is observed at high energies for α-$RuCl_3$ [Ref. 5.13,5.14]. According to a widely accepted view, the damping effect can be attributed to a two-magnon process and the renormalisation effect of the Kitaev interaction. To qualitatively test this hypothesis, a custom-built code tailored to the GKH model with the best-fitting parameters is used to calculate the two-magnon density of state (DOS).

To evaluate the magnon decay, the two-magnon DOS is calculated using

$$\mathrm{D}(\mathrm{q}, E) = \frac{1}{N}\sum_{i,j}\sum_{k}\delta(E - E_{k,i} - E_{q-k,j}) ,$$

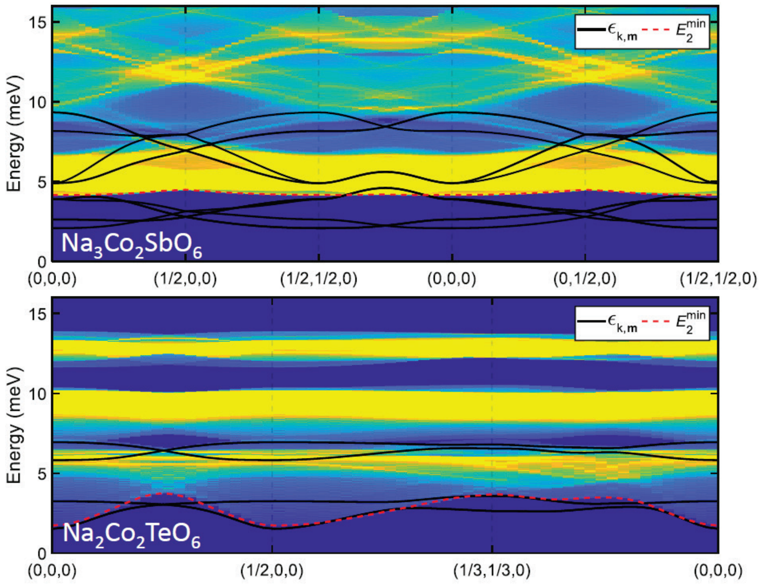

Figure 5.6 Two-magnon DOS calculation based on our best-fitting parameters. The one-magnon dispersion $\varepsilon_{k,m}$ (black line) is displayed with the two-magnon DOS. The lower bound of the two-magnon continuum is indicated by a red dashed line.

where k is the equally spaced q point over the first Brillouin zone, $E_{k,i}$ is the i^{th} magnon energy dispersion, and N is a normalisation factor. The number of possible decay channels, D(q, E_q), denotes the decay of a single magnon at (q, Eq) into two magnons with the constraint of $E_q = E_k - E_{k-q}$. Additionally, D(q, E_q) is a good approximation for the damping. Fig 5.6 displays the two-magnon DOS for NCSO and NCTO along the high symmetry lines. The strong two-magnon DOS overlaps with the upper modes of the single magnons for NCSO, accurately describing the highly damped high-energy spectra between 4 and 8 meV in our data. In contrast, for NCTO, the two-magnon DOS is present at 5–6 meV, which is just below the flat spectra close to 7 meV. These results show that the high-energy damping observed in the magnon spectra stems from the two-magnon decay process. Similar behaviour has been observed in systems with a strong anisotropic exchange, such as the Kitaev coupling and off-diagonal symmetric anisotropy terms [Ref. 5.13,5.14].

5.3. Discussion

5.3.1 Magnetic phase diagram with GKH model

To verify the direction of the magnetic moment in the GKH model, the matrix diagonalisation is calculated for both the FM and AFM Kitaev interaction models. With zig-zag magnetic order, the direction of the magnetic moment is only determined by the anisotropic interactions corresponding to the eigenvector of the matrix M [Ref. 5.1]:

$$\mathrm{M} = \begin{pmatrix} 2K & -\Gamma + 2\Gamma' & \Gamma \\ -\Gamma + 2\Gamma' & 2K & \Gamma \\ \Gamma & \Gamma & 0 \end{pmatrix}$$

With diagonalisation, the following eigenvalues are obtained:

$$\mathrm{E_p} = \Gamma - 2\Gamma' + 2\mathrm{K}$$

$$\mathrm{E}_{\pm} = \Gamma' - \frac{\Gamma}{2} + K \pm \frac{A}{2}$$

$$\text{where } A = \sqrt{9\Gamma^2 + 4\Gamma^2 + 4K^2 - 4\Gamma\Gamma' - 4K\Gamma + 8K\Gamma'}$$

In the monoclinic frame, the eigenfunction of each eigenvalue is given as follows:

$$\mathrm{v_p} = (0,1,0)$$

$$\mathrm{v}_{\pm} = \left(-\frac{\sqrt{2}}{8}\frac{7\Gamma + 2\Gamma' + 2K \pm 3A}{\Gamma' - \Gamma + K}, 0, 1\right)$$

If the minimal eigenvalue is $\mathrm{E_p}$, the magnetic moments are aligned along the bond direction and lie on the ab-plane. For $E_{\pm}$, the magnetic moments are aligned orthogonal to the bond direction and can align in the out-of-plane direction (Fig. 5.7).

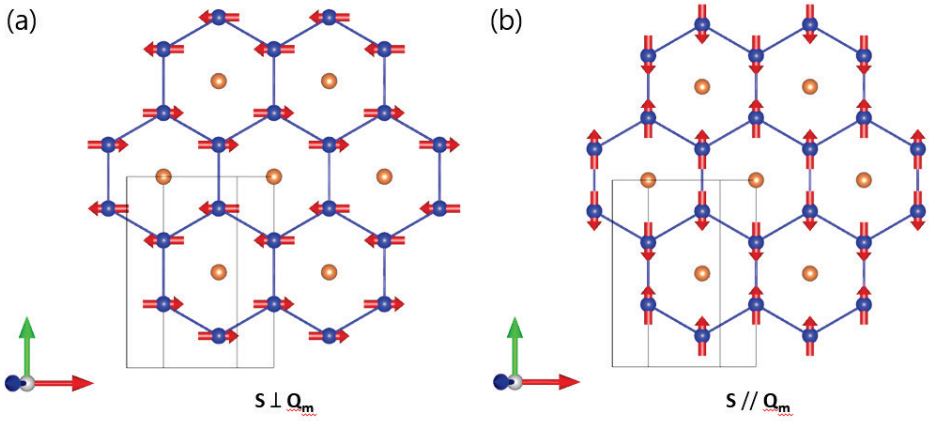

Figure 5.7 Optimized magnetic structures of zig-zag order with GKH model. (a) Eigenstate of $E_{\pm}$, wherein spins are aligned orthogonal to the bond direction. (b) Eigenstate of E_p, wherein spins are aligned along the bond direction.

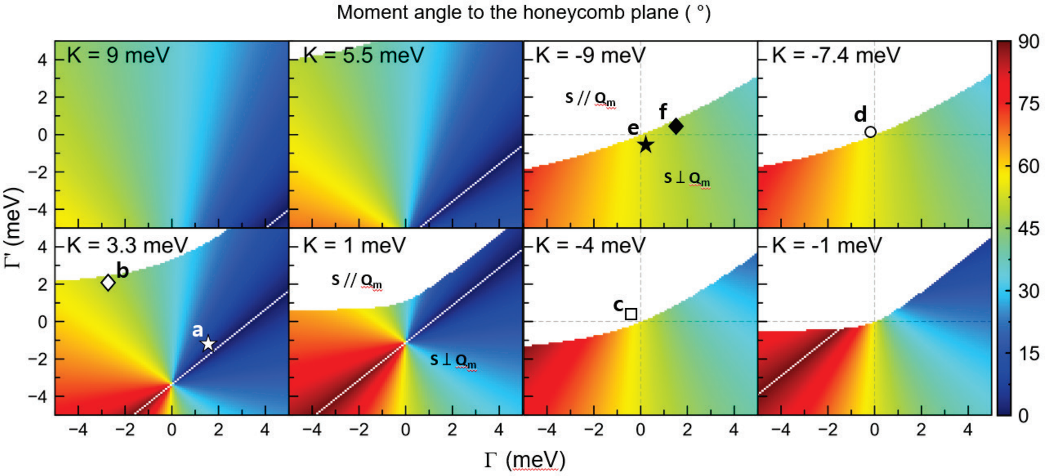

Figure 5.8 Phase diagram of the angle of out-of-plane magnetic moment in the K–Γ–Γ' space. For NCSO, (a) is the best parameter set with AFM Kitaev, (c) FM Kitaev and (e) parameter set from Ref. For NCTO, (b) is our best parameter set with AFM Kitaev, (d) FM Kitaev and (f) parameter set from [Ref. 5.15]

Fig. 5.8 displays the out-of-plane angle of the magnetic moment in the K–Γ–Γ' parameter space. In the figure, the white area represents a magnetic structure with moments parallel to the bond direction. In contrast,the coloured area represents a magnetic structure with spin orthogonal to the bond direction. The analysis shows that the AFM Kitaev interaction easily accesses the in-plane moment configuration. In contrast, the magnetic moment is mostly canted to the *c*-axis with the FM Kitaev interaction. The spin configurations of previous studies are primarily situated on the ab-plane. Thus, the counteractive trend observed with regard to the Kitaev interaction's sign implies that the AFM Kitaev model is better suited than the FM Kitaev models for elucidating the magnetic structure and spin-wave behaviour of NCSO and NCTO.

The calculated magnetic structure of our best-fitted model is located in the phase diagram of Fig. 5.8. However, although the angles of the magnetic moment of the proposed AFM Kitaev model and M. Songvilay's FM Kitaev model [Ref. 5.15] are similar, but the signs of the angles are different. Additionally, recent research suggests that the magnetic structure of NCTO may be a triple-Q zig-zag order rather than a simple single-Q zig-zag order with three equivalent domains [Ref. 5.16]. The conflicting reports on the magnetic ground state of NCTO highlight the need for further investigation to establish a reliable magnetic Hamiltonian.

5.3.2 Comparison with single-crystal data

To compare the spin waves of various models, the magnon dispersion curves for NCSO and NCTO are computed using the reported parameters and the potential impact of the domain structures on the observed spin waves is considered. Fig. 5.9 presents the spin-wave spectra of NCSO and NCTO along the high-symmetry line of the Brillouin zone for different models, with three magnetic domains indicated by different colours. For NCTO, the most striking feature of the AFM Kitaev model is the absence of any band crossing between the lower and higher magnon branches, whereas other models display such crossing through the high-symmetry lines.

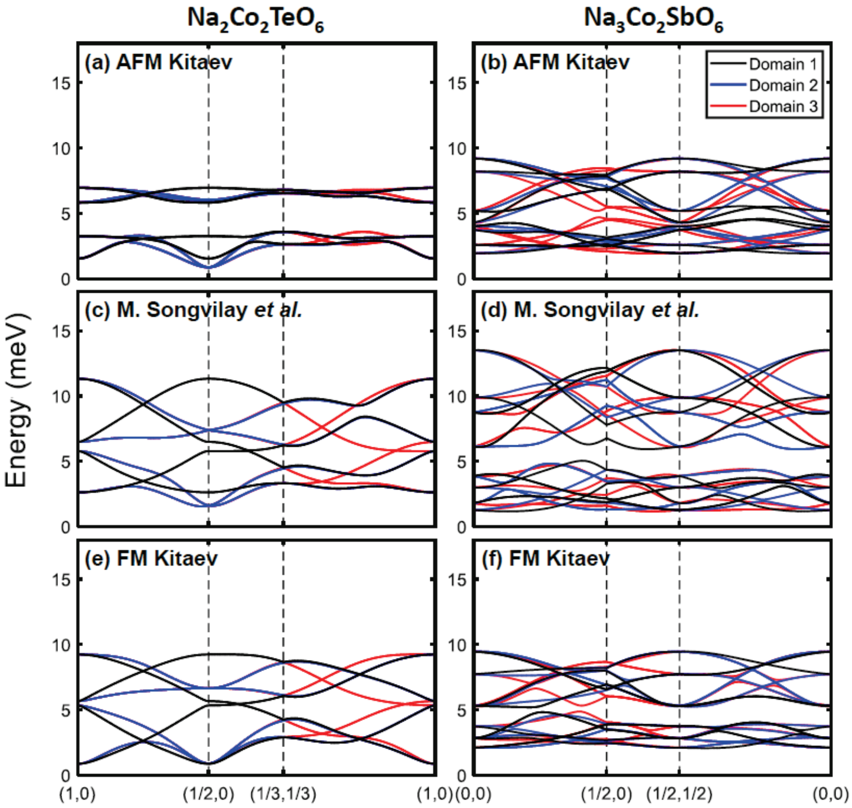

Figure 5.9 Calculated spin-wave dispersion along the high-symmetric points at the Brillouin Zone. The different color of dispersion indicates possible domains with 120° rotation.

Notably, the gapped-like feature of the spin wave manifests differently in NCSO. Specifically, NCSO's two-magnon parts are very close to each other with the AFM Kitaev model, while the branches are gapped with the FM Kitaev model [Ref. 5.15]. This characteristic gapped feature provides valuable insights and assists in selecting the appropriate magnetic Hamiltonian when analysing the single-crystal data.

5.4 Summary

This study utilised inelastic neutron scattering to measure the magnetic excitations in two potential KQSL candidates, NCSO and NCTO, containing Co ions. The temperature-dependent spin-orbit exciton observed in both compounds was attributed to the crystal field excitation between the SOE $J_{\mathrm{eff}} = 1/2$ ground state and $J_{\mathrm{eff}} = 3/2$ excited state, which stems from a positive trigonal distortion. A considerable AFM Kitaev interaction was identified using both the spin-wave spectrum and magnetic structure, with the size of Heisenberg and off-diagonal anisotropy exchange interactions. Additionally, strong magnon decay was found in the high-energy spectra, which was interpreted as the two-magnon process being enhanced by anisotropic exchanges. These results provide experimental evidence for AFM Kitaev interactions in real materials and pave the way for further exploration towards KQSL in practical applications.

References

[Ref. 5.1] Chaloupka, J. and G. Khaliullin, Phys Rev B **94**, 064435 (2016).

[Ref. 5.2] Sears, J. A. et al., Nat Phys **16**, 837 (2020).

[Ref. 5.3] Choi, S. K. et al., Phys Rev Lett **108**, 127204 (2012).

[Ref. 5.4] Hickey, C. and S. Trebst, Nat Commun **10**, 530 (2019).

[Ref. 5.5] Lefrançois, E. et al., Phys Rev B **94**, 214416 (2016).

[Ref. 5.6] Wong, C., M. Avdeev, and C. D. Ling, J Solid State Chem **243**, 18 (2016).

[Ref. 5.7] Yan, J. Q. et al., Phys Rev Mater **3**, 074405 (2019).

[Ref. 5.8] Yao, W. and Y. Li, Phys Rev B **101**, 085120 (2020).

[Ref. 5.9] Wallington, F. et al., Phys Rev B **92**, 125116 (2015).

[Ref. 5.10] Ross, K. A. et al., Phys Rev B **95**, 144414 (2017).

[Ref. 5.11] Liu, H., J. Chaloupka, and G. Khaliullin, Phys Rev Lett **125**, 047201 (2020).

[Ref. 5.12] Liu, H. and G. Khaliullin, Phys Rev B **97**, 014407 (2018).

[Ref. 5.13] Maksimov, P. A. and A. L. Chernyshev, Phys Rev Res **2**, 033011 (2020).

[Ref. 5.14] Winter, S. M. et al., Nat Commun **8**, 1152 (2017).

[Ref. 5.15] Songvilay, M. et al., Phys Rev B **102**, 224429 (2020).

[Ref. 5.16] Chen, W. et al., Phys Rev B **103**, L180404 (2021).

Chapter 6

Magnon breakdown in the cobalt Kitaev triangular antiferromagnet CoI_2

6.1 Introduction

Quantum spin liquids are a unique form of magnetic matter, proposed initially by Anderson for a triangular-lattice network of quantum spins. However, discovering materials that meet Anderson's criteria remains a considerable challenge. One successful approach uses geometrical frustration from non-bipartite lattices like triangular, Kagome, and pyrochlore spin networks [Ref. 6.1]. Another recent strategy involves utilizing bond-dependent anisotropic exchange, also known as 'exchange frustration'. [Ref. 6.2]. Kitaev's groundbreaking work demonstrated that when such interactions are applied to a honeycomb structure, it becomes exactly solvable. This solution leads to a quantum spin liquid that hosts both fractional Majorana and gauge field excitations, representing a new field of magnetism. Since the discovery of the Kitaev model and its unique properties, researchers have continuously endeavoured to realize such a model in real materials. One promising approach involves utilizing spin-orbital entangled $J_{\mathrm{eff}} = 1/2$ magnetic moments in an edge-sharing network of ligand octahedrons [Ref. 6.3].

The manifestation of Kitaev physics in geometrically frustrated systems, such as triangular-lattice antiferromagnets (TLAFs) and pyrochlore-lattice systems, has received less attention, but we decided to choose it as the focus of this research for the following reasons. Although a few 5*d* compounds, such as triangular-lattice $Ba_3IrTi_2O_9$ [Ref. 6.4]and

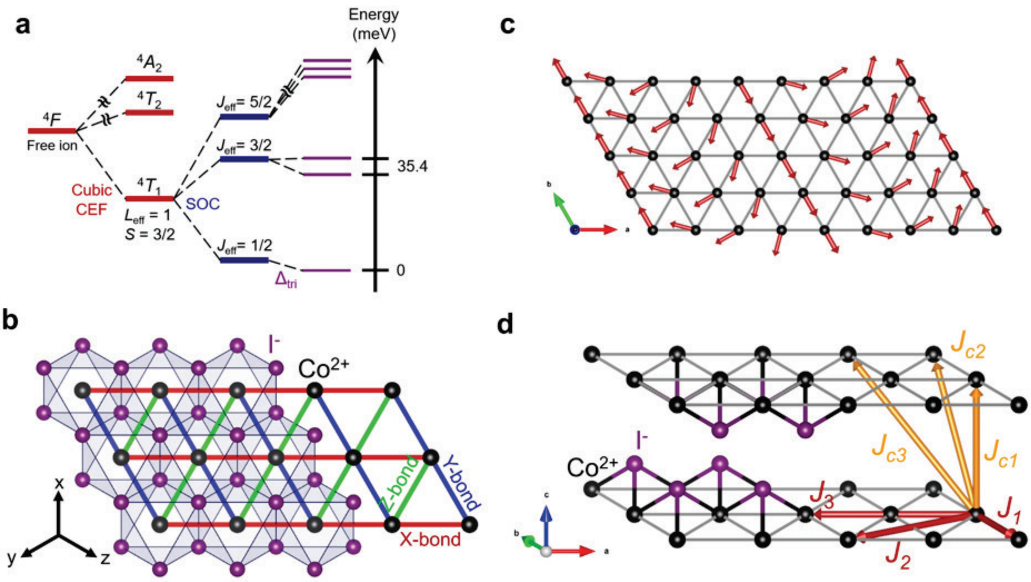

Figure 6.1 (a) Single-ion picture of Co^{2+} ions in CoI_2. (b) Schematic of Kitaev interactions in a triangular lattice. (c) Magnetic structure of CoI_2 (d) Crystal structure of CoI_2 and the path of magnetic exchange interaction. The red arrows indicate intra-layer coupling, and the yellow arrows indicate inter-layer coupling.

pyrochlore-lattice $La_2(Mg/Zn)IrO_6$ [Ref. 6.5], have been proposed for realizing this physics, they lack the edge-sharing network of ligands, a characteristic of Kitaev materials. As a result, synthesizing single crystals of such 5*d* compounds for spectroscopic probes remains a challenging task. Thus, identifying a genuine example of Kitaev physics in geometrically frustrated lattices is crucial.

The non-collinear magnetic order and quantum fluctuations of TLAFs are expected to generate significant quantum effects on magnetic excitations. One such effect is magnon decay, wherein magnons can break down into multiple magnons or other types of quasiparticles [Ref. 6.6]. While this effect typically results in spectral line broadening, in the strong interaction limit, magnons can undergo avoided decay transitions [Ref. 6.7,6.8]

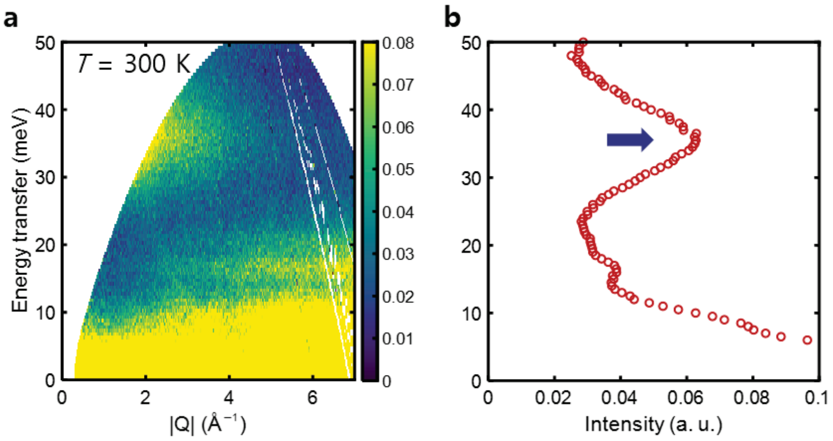

Figure 6.2 (a) Spin–orbit exciton at room temperature. The power-averaged data were measured using the incident energy E_i = 52 meV. (b) Constant-momentum cut of power-averaged data. The data were integrated using: Q = [1, 4] Å^{-1}

or be deconfined into spinons [Ref. 6.9]. Although only a few experimental observations of such spontaneous quasiparticle breakdown have been reported to date (e.g. $Ba_3CoSb_2O_9$, $BiCu_2PO_6$) [Ref. 6.7–6.11], it is crucial to determine the spin dynamics in the case of the exotic S = 1/2 Kitaev system with a triangular lattice.

Here, we introduce the spin dynamics of the first ever reported example of a triangular-lattice Kitaev system—CoI_2, which is a member of the van der Waals triangular lattice TMX_2 (TM = Transition metal, X = Halide) family [Ref. 6.12]. CoI_2 comprises layers of CoI_6 octahedrons that are connected in an edge-sharing network and form a triangular lattice (Fig. 6.1b) and is thus an ideal starting system to search for Kitaev interactions. Our inelastic neutron scattering data show a distinct signature of a spin–orbit exciton at 35.4 meV, corresponding to a transition between the J_{eff} = 3/2 and 1/2 multiplets of the spin–orbit entangled $3d^7$ manifold (See Fig. 6. 2). The large gap between these excitations indicates that we can model the J_{eff} = 1/2 states without considering the higher-J states in the low-energy Hamiltonian. CoI_2 orders antiferromagnetically at T_N = 9 K, where the J_{eff} = 1/2 moments form a long-period commensurate spiral order in the *ab* plane and are coupled antiferromagnetically between the planes with a propagation vector $\mathbf{Q}_m$ = (1/8, 0, 1/2) (Fig. 6.1(c)) [Ref. 6.12].

6.2 Minimal Hamiltonian for CoI_2

Before verifying the nature of CoI_2, we need to minimize the magnetic Hamiltonian based on the observed magnetic structure. We first redraw the magnetic phase diagram of the J_1–J_2–J_3 model using the classical Luttinger–Tisza (LT) method [Ref. 6.13]. This model was suggested in a previous study in which ferromagnetic J_1 was used [Ref. 6.12]. This phase diagram shows the competition between the further nearest neighbour interactions and yields various types of magnetically ordered phases. In this model, the observed propagation vector Q_m = (1/8, 0, 0) is stabilized with the following constraints: $2\sqrt{2}J_3 + \left(1+\sqrt{2}\right)J_2 + J_1 = 0$, which further requires a comparable size of antiferromagnetic J_2 with respect to J_1. However, this scenario is in stark contrast to the results obtained in most experimental studies on cobalt edge-sharing materials, which show a small or negligible J_2 and sizable third-nearest neighbour interaction J_3 [Ref. 6.14,6.15].

To resolve this inconsistency, we used another simplified model with a bond-dependent anisotropy, i.e. the J_1–$J_{\pm\pm}$–J_3 model. Because CoI_2 satisfies the condition for realizing a bond-dependent anisotropy, which is allowed by crystal symmetry, the implication of this model is reasonable. Based on the symmetry analysis [Ref. 6.16,6.17], we can use the magnetic Hamiltonian as follows:

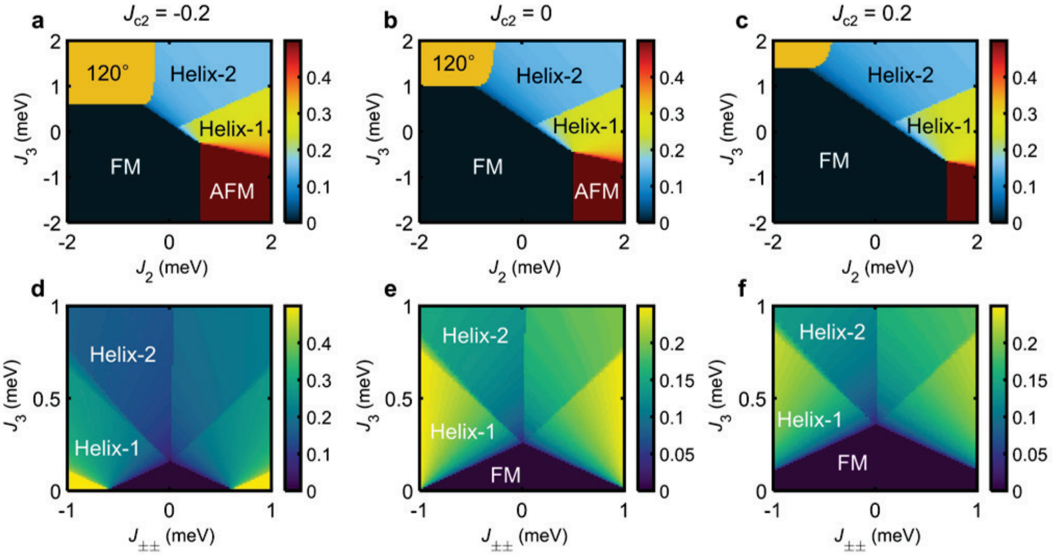

Figure 6.3 (a-c) Magnetic phase diagram of the J_1–J_2–J_3 model with a finite second nearest neighbour intra-layer coupling J_{c2}. (d-f) Magnetic phase diagram of the J_1–$J_{\pm\pm}$–J_3 model with a finite J_{c2}. The coloured map in the figure indicates the length of the magnetic propagation vector Q_m.

$$\begin{aligned} H = \sum_{<i,j>_n}^{n=1} & \Big\{ J_1\left[S_i^x S_j^x + S_i^y S_j^y + \Delta_1 S_i^z S_j^z\right] \\ & + 2J_{\pm\pm}\left[\left(S_i^x S_j^x - S_i^y S_j^y\right)\cos\phi_\alpha - \left(S_i^x S_j^y + S_i^y S_j^x\right)\sin\phi_\alpha\right] \\ & + J_{z\pm}\left[\left(S_i^y S_j^z + S_i^y S_j^z\right)\cos\phi_\alpha - \left(S_i^x S_j^z + S_i^z S_j^x\right)\sin\phi_\alpha\right]\Big\} \\ & + \sum_{<i,j>_n}^{n=3} J_3\left[S_i^x S_j^x + S_i^y S_j^y + \Delta_3 S_i^z S_j^z\right] \\ & + \sum_{<i,j>_n}^{n=2,c_1,c_2} J_n\left[S_i^x S_j^x + S_i^y S_j^y + S_i^z S_j^z\right], \end{aligned}$$

with the bond-dependent phase factor $\phi_\alpha \in \left\{0, \frac{2\pi}{3}, -\frac{2\pi}{3}\right\}$, and each phase factor represents the *X*-, *Y*-, and *Z*-bonds (Fig. 6.1(b) and (d)). In the following, we neglect the allowed $J_{z\pm}$ anisotropy because the magnetic moments in CoI$_2$ are aligned in the *ab*-plane [Ref. 6.12].

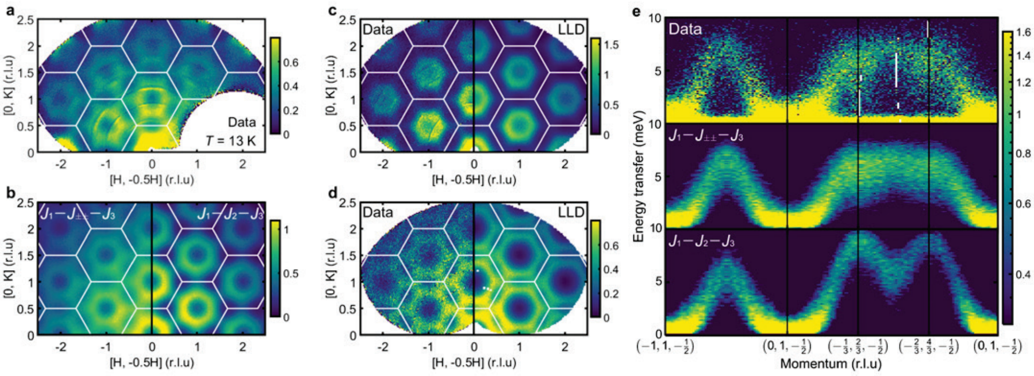

Figure 6.4 (a) Paramagnetic inelastic neutron signal measured at $T = 13$ K by integrating the energy transfer E = [1, 7] meV and that measured along the L-direction with L = [-0.7, 0.7] r.l.u. (b) Comparison of the J_1–$J_{\pm\pm}$–J_3 and J_1–J_2–J_3 (dominant) models using the LLD (c-d) Comparison of the constant-E cuts between the experimental data and LLD simulation of J_1–$J_{\pm\pm}$–J_3 at E = [1, 3] meV and [4, 7] meV for (c), (d), respectively. (e) Energy–momentum resolved scattering intensity along the high-symmetric points in the BZ with E_i = 17 meV and comparison with model data. The data were integrated with 0.2 Å^{-1} for the L direction and 0.036 Å^{-1} for the in-plane direction.

We also neglect the inter-layer coupling and anisotropic factor Δ_3 for simplicity. Using the LT method with the J_1–$J_{\pm\pm}$–J_3 model, we find that the $J_{\pm\pm}$ term is essential to stabilize the observed propagation vector (see Fig. 6.3). This implies that a bond-dependent anisotropy is crucial for explaining the magnetic order of CoI$_2$. In the general case, we can stabilize the observed magnetic order using a single equation: $2\sqrt{2}J_3 + (1+\sqrt{2})J_2 + |J_{\pm\pm}| + J_1 - 2J_{c2} = 0$.

6.3 Magnetic excitations of CoI$_2$

6.3.1 Paramagnetic excitation

To gain insight into the exchange constants of CoI$_2$, we analyze the magnetic scattering data obtained in the paramagnetic regime, where magnetic order is absent and only shortrange correlations are present. This approach facilitates a more reliable estimation of the exchange parameters because the influence of quantum fluctuations is expected to be minimal in the paramagnetic state and thus result in a semi-classical behaviour of the spin dynamics. Fig. 6.4 illustrates the diffuse scattering pattern of CoI_2 at a temperature of 13 K in the paramagnetic state. The energy-integrated diffuse scattering pattern has a hexagonal shape, which is aligned with the boundaries of the Brillouin Zone (BZ), and the hexagons at the K points in the BZ are connected by lines. An analysis of the energy and momentum-resolved cuts along the high-symmetry momentum directions of the BZ reveals highly dispersive signals of paramagnetic scattering just above the Néel temperature (Fig. 6.4e). This observation is consistent with our expectations of pronounced magnetic correlations and fluctuations in this system.

Identifying an appropriate exchange model becomes crucial when examining the energy-resolved paramagnetic excitations. Accordingly, we utilized the Landau–Lifshitz dynamics (LLD) [Ref. 6.18] to simulate the paramagnetic excitations for two minimal intra-layer coupling models: the J_1–J_2–J_3 and J_1–$J_{\pm\pm}$–J_3 models. For the J_1–J_2–J_3 model, we utilized the following parameter values, which were derived from the bandwidth of the paramagnetic excitation and constraints based on the LT method: J_1 = -3.8 meV, J_2 = 1.52 meV, J_3 = -0.32 meV, J_{c1} = -0.38 meV, J_{c2} = 0.38 meV, and Δ_1 = 0.93. In contrast, for the J_1–$J_{\pm\pm}$–J_3 model, we adjusted the parameters as follows: J_1 = -2.73 meV, $J_{\pm\pm}$ = -0.41 meV, J_3 = 1.01 meV, J_{c1} = 0.27 meV, J_{c2} = 0.27 meV, and Δ_1 = 0.95. Fig. 6.4 displays the discrepancies between the energy-integrated scattering signatures obtained from the two models, particularly regarding the shape and intensity of the hexagonal patterns. Notably,

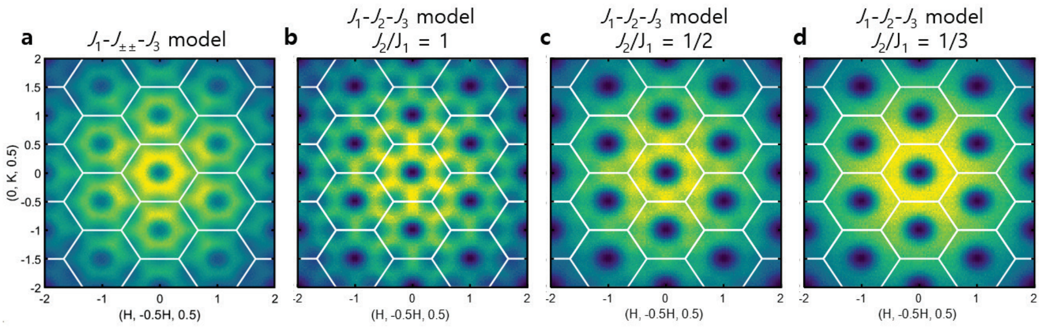

Figure 6.5 (a) Theoretical paramagnetic scattering intensity of the J_1–$J_{\pm\pm}$–J_3 model compared with that of the J_1–J_2–J_3 model. (b-d) Calculated paramagnetic intensity of the J_1–J_2–J_3 model with J_1 = -2.1 meV, and J_3 is determined from the constraint equation: $2\sqrt{2}J_3 + J_1 + (1+\sqrt{2})J_2 = 0$.

the scattering signature primarily originates from J_2 and J_3 (refer to Fig. 6. 5). Furthermore, when these two models are compared based on the energy-resolved data through cuts along the high-symmetry directions, significant distinctions emerge along the Γ–K direction, where only the J_1–$J_{\pm\pm}$–J_3 model exhibits a flat-dispersion-like behaviour. This finding again underscores the importance of bond-dependent exchange anisotropy in CoI_2, ultimately giving rise to the observed non-collinear spiral order.

6.3.2 Spin-wave spectrum

Fig. 6.6. shows the spin-wave spectrum of CoI_2 in the magnetically ordered state at $T = 4$ K. The energy-resolved data are cut along the in-plane high-symmetric points at L = -1/2 with the two-neutron incident energy. Along the (H, 0, 0) direction, we observe a gapless excitation originating from the spiral magnetic order with Q_m = (1/8, 0, 1/2). This gapless excitation can be explained using the J_1–J_2–J_3 and J_1–$J_{\pm\pm}$–J_3 models, given the emergent continuous symmetry of the latter. Although the low-energy magnon is distinct and sharp,

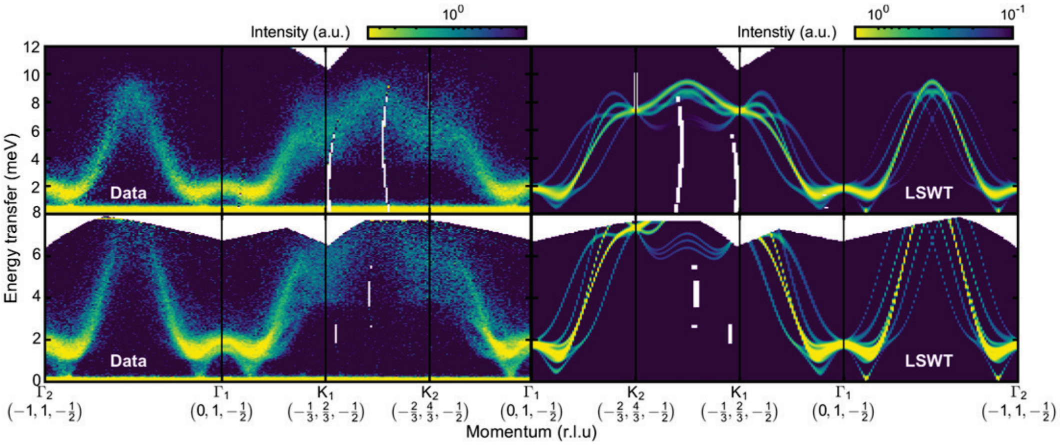

Figure 6.6 Comparison of inelastic scattering cross-section between the data (left) and theoretical calculation (right) at $T = 4$ K. The upper (lower) row data were measured with the incident energy E_i = 17(8) meV, and the data were integrated with 0.2 Å^{-1} for the L direction and 0.036 Å^{-1} for the in-plane direction. We convoluted the LSWT solution with an experimental resolution of FWHM = 0.3(0.15) meV for each incident energy.

a significant linewidth broadening of the magnon is observed at the BZ boundaries, especially along the Γ–K direction. In the 8-meV data, complex magnon band splitting appears beneath the magnon decay as the K point approaches.

We compared the data with the linear spin-wave theory (LSWT) simulation with exchange interactions from the paramagnetic phase to understand the measured spin-wave spectrum. We considered all three possible symmetrically equivalent magnetic domains in our calculations. Although the overall spectrum, such as the magnon bandwidth, is well-matched with the simulated spectrum, a significant deviation is evident between the experimental and LSWT-simulated spectra. For example, with the convolution of the instrumental resolution, the high-energy magnon branch becomes considerably broader than its simulated counterpart, especially at the BZ boundary. Moreover, an extra magnon branch, split from the dispersion, appears near 1.5 meV along the Γ–K direction; however, the LSWT cannot capture this split branch.

6.4 Magnon damping in CoI$_2$

To explain the origin of the significant magnon linewidth broadening in CoI$_2$, we calculated the two-magnon density-of-states (DOS) using our best-performing model. Fig 6.7 (a) shows the calculated two-magnon DOS with the corresponding INS data. The two-magnon DOS simulation predicts the spontaneous one-magnon decay via three boson terms [Ref. 6.6]. The two-magnon DOS is calculated using the same method presented in Chapter 5. The one-magnon branches are overlapped with the two-magnon DOS at the high-energy

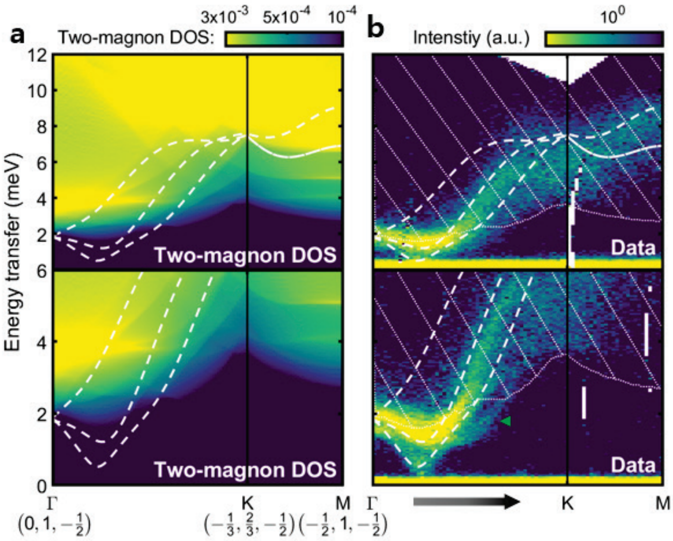

Figure 6.7 (a) Calculated two-magnon DOS based on LSWT result. The upper (lower) column shows the different energy cut-offs with E = 12 (6) meV. The white dashed lines represent one-magnon dispersion from a single magnetic domain, and the colour scale is the number of two-magnon DOS. **(b)** Real data compared to the kinematic extent of the two-magnon continuum. The dotted line indicates the two-magnon continuum boundary, and the dashed lines represent the magnon dispersion predicted by LSWT. The upper (lower) column data were measured with an incident energy E_i = 17(8) meV.

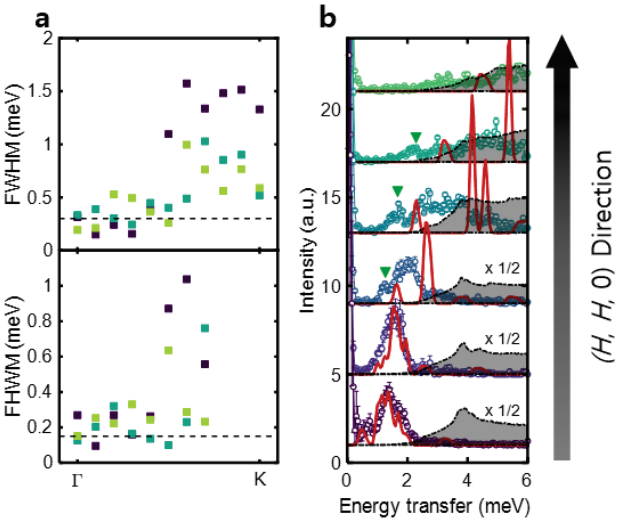

Figure 6.8 (a) Fitted FWHM of the magnon modes along the Γ–K line in Fig. 6. 7(b). The instrumental resolution of each incident energy is indicated by black dashed lines. (b) Constant-Q cut for comparison between real and theoretical data with E_i = 8 meV. Each momentum slice was cut along the same direction in (a). The red lines indicate the LSWT result, and the grey shaded area shows the two-magnon DOS. The green triangle indicates the avoided decay mode shown in Fig. 6.7(b).

region, consistent with the observed linewidth broadening region. We conducted a linewidth analysis of the magnon modes along the Γ–K direction, as shown in Fig. 6.8 (a) (corresponding to the same direction as that shown in Fig. 6.7 (a)-(b)). Interestingly, we observed a notable increase in the full width at half maxima (FWHM) of the magnon modes when the one-magnon branches entered the LSWT-calculated two-magnon continuum. Furthermore, we found that the FWHM in the decay region exceeds the instrumental resolution (0.3 meV for E_i = 17 meV, 0.15 meV for E_i = 8 meV). This significant overlap between the magnon modes and the continuum is a distinctive characteristic of CoI_2. It can be primarily attributed to gapless Goldstone modes in the anisotropic model. It is worth noting that such behaviour is uncommon, as anisotropic exchange interactions typically open an energy gap in other systems [Ref. 6.15,6.19].

We also observed that the magnon mode around 1.5 meV exists well below the region where a significant two-magnon DOS is observed (green triangle in Fig. 6.7 (b) & 6. 8(b)). However, our LSWT simulation results indicate that even the lowest-energy magnon branch largely overlaps with the two-magnon DOS as the momentum transfer approaches the K point. This observed phenomenon can be attributed to the substantial renormalization of the lowest magnon branch in the LSWT simulations; this renormalization allows it to avoid the two-magnon continuum and appear as a distinct branch, as indicated by the green triangle in Fig. 6.7 (b). Such an avoided crossing naturally arises from the strong interactions between the quasiparticles [Ref. 6.7,6.10], and as a result, both decay and avoided decay modes coexist in the spin dynamics of $\mathrm{CoI_2}$.

In the theoretical framework, a spin-1/2 TLAF system exhibits magnon decay and renormalization effects, represented by three boson terms. As a result, a magnon can decay into two magnons with specific kinematic constraints (as discussed in Chapter 2). Typically, this type of coupling is achieved in non-collinear magnetic structures, and to date, this mechanism has been demonstrated in a few real systems in some reported studies [Ref. 6.20]. However, recent research has indicated that a transverse-to-longitudinal coupling can also occur with bond-dependent anisotropy, even in collinear magnetic structures, as observed in α-$\mathrm{RuCl_3}$ [Ref. 6.21]. Interestingly, $\mathrm{CoI_2}$ exhibits both possibilities, potentially leading to a more pronounced magnon decay than in other systems, which exhibit only one mechanism. Furthermore, the non-collinear spiral order observed in $\mathrm{CoI_2}$ is stabilized by the $J_{\pm\pm}$ interactions, and we propose that the bond-dependent anisotropy plays a crucial role in this system.

6.5 Summary

The results of this study unveiled a complex and diverse range of spin dynamics in a cobalt Kitaev triangular lattice, exemplified by the non-collinear antiferromagnet CoI_2. The bond-dependent exchange anisotropy plays a pivotal role in forming a non-collinear magnetic order in CoI_2. Our investigation also revealed a substantial magnon decay, successfully selectively avoided over a large momentum space. We attribute these phenomena to strong interactions between magnons induced by the bond-dependent anisotropy and non-collinear magnetic order. Therefore, our findings are crucial for comprehending the intricate interplay between bond-dependent anisotropy and non-collinear magnetic order in quantum magnets.

References

[Ref. 6.1] Balents, L., Nature **464**, 199 (2010).

[Ref. 6.2] Kitaev, A., Ann Phys (N Y) **321**, 2 (2006).

[Ref. 6.3] Jackeli, G. and G. Khaliullin, Phys Rev Lett **102**, 017205 (2009).

[Ref. 6.4] Catuneanu, A. *et al.*, Phys Rev B **92**, 165108 (2015).

[Ref. 6.5] Aczel, A. A. *et al.*, Phys Rev B **93**, 214426 (2016).

[Ref. 6.6] Zhitomirsky, M. E. and A. L. Chernyshev, Rev Mod Phys **85**, 219 (2013).

[Ref. 6.7] Verresen, R., R. Moessner, and F. Pollmann, Nat Phys **15**, 750 (2019).

[Ref. 6.8] Ito, S. *et al.*, Nat Commun **8**, 8 (2017).

[Ref. 6.9] Ghioldi, E. A. *et al.*, Phys Rev B **106**, 064418 (2022).

[Ref. 6.10] Macdougal, D. *et al.*, Phys Rev B **102**, 064421 (2020).

[Ref. 6.11] Plumb, K. W. *et al.*, Nat Phys **12**, 224 (2016).

[Ref. 6.12] Kuindersma, S. R., J. P. Sanchez, and C. Haas, Physica B+C **111**, 231 (1981).

[Ref. 6.13] Litvin, D. B., Physica **77**, 205 (1974).

[Ref. 6.14] Kim, C. *et al*., Phys Rev B **102**, 184429 (2020).

[Ref. 6.15] Kim, C. *et al*., Journal of Physics: Condensed Matter **34**, 045802 (2022).

[Ref. 6.16] Bai, X. *et al*., Nat Phys **17**, 467 (2021).

[Ref. 6.17] Maksimov, P. A. *et al*., Phys Rev X **9**, 21017 (2019).

[Ref. 6.18] Dahlbom, D. *et al*., Phys Rev B **106**, 054423 (2022).

[Ref. 6.19] Banerjee, A. *et al*., NPJ Quantum Mater **3**, 8 (2018).

[Ref. 6.20] Kim, T. *et al*., J Physical Soc Japan **88**, 081003 (2019).

[Ref. 6.21] Winter, S. M. *et al*., Nat Commun **8**, 1152 (2017).

Chapter 7
Summary and Outlook

7.1 Summary

Through this thesis, I have presented my research on the spin dynamics of Kitaev candidates in cobalt compounds. First, I examined the existence of the spin-orbital entangled $J_{\mathrm{eff}} = 1/2$ state in the van der Waals antiferromagnet $CoPS_3$. Using inelastic neutron scattering (INS), I measured the temperature dependence of magnetic excitation in polycrystalline $CoPS_3$. The absence of an excitation signal at 20–30 meV above the Néel temperature implies that $CoPS_3$ is closer to the spin $S = 3/2$ state than the $J_{\mathrm{eff}} = 1/2$ state. Based on this observation, the spin-wave spectrum was analysed using the XXZ Heisenberg model. The XXZ Heisenberg model with anisotropy factor $\alpha = J_x/J_z = 0.6$ explained the observed spectrum better than the isotropic Heisenberg model. Therefore, I concluded $CoPS_3$ was in the spin $\mathrm{S} = 3/2$ state with a strong XXZ Heisenberg model.

Second, I investigated the spin dynamics of the cobalt honeycomb materials $Na_2Co_2TeO_6$ (NCTO) and $Na_3Co_2SbO_6$ (NCSO). By employing the INS technique with polycrystalline samples, we observed a spin-orbit exciton within the 20–30 meV energy range in both compounds. The presence of this exciton provides supporting evidence for the existence of $J_{\mathrm{eff}} = 1/2$ ground states. Our analysis of spin waves confirmed the presence of finite Kitaev interactions in both compounds, albeit with a different sign ($\mathrm{K} > 0$) than previously reported candidates. To comprehend the magnetic properties of these materials, we conducted a comprehensive examination of the magnetic phase diagrams and calculated the density of states (DOS) for two-magnon processes.

Lastly, we presented the first-ever realisation of Kitaev interactions on a triangular lattice in CoI_2. By employing the Luttinger–Tisza method, we proposed two potential minimal models to elucidate the magnetic structure of CoI_2: one incorporating a Kitaev term and the other excluding it. INS measurements conducted during the paramagnetic phase validated the suitability of the minimal model with bond-dependent anisotropy in explaining the characteristics of CoI_2. The spin-wave spectrum observed during the ordered phase exhibited large linewidth broadening across different momentum values, indicating magnon decay. To further investigate this decay process, we performed an analysis using the density of states for two-magnon interactions.

7.2 Outlook

First, recent theoretical studies [Ref. 7.1–7.3], including my review paper [Ref. 7.4], have found that previous theoretical studies were misleading in their final statement because they neglected the hopping process. Recent studies suggest instead that the Kitaev interaction in the cobalt compounds is antiferromagnetic and small compared with the isotropic Heisenberg interaction [Ref. 7.1,7.2]. These recent theories are also consistent with my results for NCTO and NCSO. Thus, an in-depth experiment is needed to confirm the ratio between the Kitaev and Heisenberg interactions. However, it would also be interesting to investigate the J_1-J_3 FM-AFM quantum phase diagram. Several theoretical studies found that the S=1/2 J_1-J_3 FM-AFM XXZ model shows novel magnetic phases, such as double zig-zag order, Ising AFM order, and spin-liquid, via quantum fluctuations [Ref. 7.5–7.7]. As the current experiments confirm that most cobalt Kitaev candidates use the J_1-J_3 FM-

AFM XXZ model, the cobalt honeycomb materials are an ideal platform to search for a novel magnetic phase stabilised by quantum fluctuations. Indeed, the other cobalt Kitaev honeycomb candidate $BaCo_2(AsO_4)_2$ shows a double zig-zag order [Ref. 7.8]. Other cobalt honeycombs such as $A_3Co_2SbO_6$ (A = Cu, Ag) [Ref. 7.9,7.10] can also be an example of this model.

Changing the subject, measuring quantum entanglement in a many-body system using INS [Ref. 7.11–7.14] is an interesting topic related to these cobalt Kitaev systems. Recent single-crystal measurements of cobalt Kitaev candidates (NCTO, $BaCo_2(AsO_4)_2$) cannot be fully explained by the linear spin-wave theory, especially the broad magnetic excitation features [Ref. 7.15,7.16]. This inconsistency between theory and experiment can be acceptable because they have effective spin $S = 1/2$ systems, so non-linear effects such as 1/S become significant. Alternatively, we can understand these broad features as the signature of the entanglement based on the quantum Fisher information [Ref. 7.12,7.13]. There are some good examples of measuring the entanglement of quantum materials using INS. Although fully quantum mechanical calculations, such as a density matrix renormalisation group or an exact diagonalisation, are needed to compare the data, I believe a quantitative INS data analysis on the cobalt Kitaev candidates would be an interesting approach to measuring entanglement in quantum materials.

Finally, the transition metal diiodide TMI_2 family (TM = V, Mn, Fe, Co, Ni) [Ref. 7.17] offers interesting new potential for exploring the Kitaev physics of the triangular lattice. This family was discovered and reported in the 1960s and 70s, but its spin dynamics are poorly studied and need urgent systematic study. Except for FeI_2, the TMI_2 family have helical magnetic order with multiferroicity [Ref. 7.17]. TM = Fe, Co already proved that they have significant Kitaev interaction [Ref. 7.18]. Although I did not cover it in my thesis, I also suspect NiI_2 can host the Kitaev interaction, as theoretically predicted [Ref. 7.19,7.20]. I also think the strong spin-orbit coupling of iodine plays an important role in hosting the Kitaev interaction, even for transition metals without a spin-orbital entangled state. Therefore, I believe investigating the spin dynamics of two other compounds, VI_2 [Ref. 7.21] and MnI_2 [Ref. 7.22], using INS would also be interesting.

References

[Ref. 7.1] Winter, S. M., Journal of Physics: Materials **5**, 045003 (2022).

[Ref. 7.2] Liu, X. and H.-Y. Kee, Phys Rev B **107**, 054420 (2023).

[Ref. 7.3] Das, S. et al., Phys Rev B **104**, 134425 (2021).

[Ref. 7.4] Kim, C., H.-S. Kim, and J.-G. Park, Journal of Physics: Condensed Matter **34**, 023001 (2022).

[Ref. 7.5] Bose, A. et al., ArXiv 2212.13271 (2022).

[Ref. 7.6] Jiang, S., S. R. White, and A. L. Chernyshev, ArXiv 2304.06062 (2023).

[Ref. 7.7] Watanabe, Y., S. Trebst, and C. Hickey, ArXiv 2212.14053 (2022).

[Ref. 7.8] Maksimov, P. A. et al., Phys Rev B **106**, 165131 (2022).

[Ref. 7.9] Roudebush, J. H. et al., Inorg Chem **52**, 6083 (2013).

[Ref. 7.10] Zvereva, E. A. et al., Dalton Transactions **45**, 7373 (2016).

[Ref. 7.11] Laurell, P. et al., Phys Rev Lett **127**, 37201 (2021).

[Ref. 7.12] Hauke, P. et al., Nat Phys **12**, 778 (2016).

[Ref. 7.13] Scheie, A. et al., Phys Rev B **103**, 224434 (2021).

[Ref. 7.14] Scheie, A. O. et al., ArXiv 2109.11527 (2021).

[Ref. 7.15] Yao, W. et al., Phys Rev Lett **129**, 147202 (2022).

[Ref. 7.16] Halloran, T. et al., Proceedings of the National Academy of Sciences **120**, 2205.15262 (2023).

[Ref. 7.17] McGuire, M., Crystals (Basel) **7**, 121 (2017).

[Ref. 7.18] Bai, X. et al., Nat Phys **17**, 467 (2021).

[Ref. 7.19] Stavropoulos, P. P., D. Pereira, and H. Y. Kee, Phys Rev Lett **123**, 37203 (2019).

[Ref. 7.20] Amoroso, D., P. Barone, and S. Picozzi, Nat Commun **11**, 5784 (2020).

[Ref. 7.21] Kuindersma, S. R., J. P. Sanchez, and C. Haas, J Magn Magn Mater **15–18**, 517 (1980).

[Ref. 7.22] Kurumaji, T. et al., Phys Rev Lett **106**, 167206 (2011).

Publication lists

[1] **Chaebin Kim**, Jaehong Jeong, Pyeongjae Park, Takatsugu Masuda, Shiichiro Asai, Shinichi Itoh, Heung-Sik Kim, Andrew Wildes, and Je-Geun Park, “Spin Waves in the two-dimensional honeycomb lattice XXZ-type van der Waals antiferromagnet $CoPS_3$”, Phys. Rev. B **102**, 184429 (2020)

[2] Seokhwan Yun, Ki Hoon Lee, **Chaebin Kim**, Junghwan Park, Min-Gyu Kim, Deok-Yong Cho, Daniel I. Khomskii, and Je-Geun Park, “Effects on Mn-substitution on the valence bond solid in Li_2RuO_3”, Phys. Rev. B **103**, 035151 (2021)

[3] Hwanbeom Cho, Choong H Kim, Yongmoon Lee, Kazuki Komatsu, Byeong-Gwan Cho, Deok-Yong Cho, Taehun Kim, **Chaebin Kim**, Younghak Kim, Tae Yeong Koo, Yukio Noda, Hiroyuki Kagi, Daniel I. Khomskii, Donghoon Seoung, and Je-Geun Park, “Pressure-induced transition from $J_{\mathrm{eff}} = 1/2$ to $S = 1/2$ states in $CuAl_2O_4$”, Phys. Rev. B **103**, L081101 (2021)

[4] Gaoting Lin, Jaehong Jeong, **Chaebin Kim**, Yao Wang, Qing Huang, Takatsugu Masuda, Shinichiro Asai, Shinichi Itoh, Gerrit Günther, Margarita Russina, Zhilun Lu, Jieming Sheng, Le Wang, Jiucai Wang, Guohua Wang, Qingyong Ren, Chuanying Xi, Wei Tong, Langsheng Ling, Zhengxin Liu, Liusuo Wu, Jiawei Mei, Zhe Qu, Haidong Zhou, Xiaoqun Wang, Je-Geun Park, Yuan Wan, and Jie Ma, “Field-induced quantum spin disordered state in spin-1/2 honeycomb magnet $Na_2Co_2TeO_6$”, *Nat. Commun.* ***12****, 5559* (2021)

[5] **Chaebin Kim**, Heung-Sik Kim, and Je-Geun Park, “Spin-orbital entangled state and realization of Kitaev physics in 3*d* cobalt compounds: a progress report”, J. Phys. Condens. Matter **34**, 023001 (2021)

[6] **Chaebin Kim**, Jaehong Jeong, Gaoting Lin, Pyeongjae Park, Takatsugu Masuda, Shinichiro Asai, Shinichi Itoh, Heung-Sik Kim, Haidong Zhou, Jie Ma, and Je-Geun Park, “Antiferromagnetic Kitaev interaction in $J_{\mathrm{eff}} = 1/2$ cobalt honeycomb materials $Na_3Co_2SbO_6$ and $Na_2Co_2TeO_6$”, J. Phys. Condens. Matter **34**, 045802 (2021)

[7] Suhan Son, Youjin Lee, Jae Ha Kim, Beom Hyun Kim, **Chaebin Kim**, Woongki Na, Hwiin Ju, Sudong Park, Abhishek Nag, Ke-Jin Zhou, Young-Woo Son, Hyeongdo Kim, Woo-Suk Noh, Jae-Hoon Park, Jong Seok Lee, Hyeonsik Cheong, Jae Hoon Kim, Je-Geun Park, “Multiferroic-enabled magnetic-excitons in 2d quantum-entangled Van der Waals antiferromagnet NiI_2”, Adv. Mat. **34**, *2109144* (2022)

[8] Heejun Yang†, **Chaebin Kim†**, Ysun Choi, Jun Han Lee, Gaoting Lin, Jie Ma, Marie Kratochvílová, Petr Proschek, Eun-Gook Moon, Ki Hoon Lee, Yoon Seok Oh, and Je-Geun Park, “Significant thermal Hall effect in the 3*d* cobalt Kitaev system $Na_2Co_2TeO_6$”, Phy. Rev. B **106**, L081116 (2022). (†: equally contributed)

[9] Youjin Lee†, Suhan Son†, **Chaebin Kim†**, Soonmin Kang, Junying Shen, Michel Kenzelmann, Bernard Delley, Tatiana Savchenko, Sergii Parchenko, Woongki Na, Ki-Young Choi, Wondong Kim, Hyeonsik Cheong, Peter M Derlet, Armin Kleibert, and Je-Geun Park, “Giant magnetic anisotropy in the atomically thin Van der Waals antiferromagnet $FePS_3$”, *Adv. Elect. Mat 2200650* (2022) (†: equally contributed)

[10] **Chaebin Kim†**, Sujin Kim†, Pyeongjae Park, Taehun Kim, Jaehong Jeong, Seiko Kawamura, Kenji Nakajima, Naoki Murai, Alexander Chernyshev, Martin Mourigal, Sung-

Jin Kim, and Je-Geun Park, “Bond-dependent anisotropy and magnon breakdown in cobalt Kitaev triangular antiferromagnet”, Accepted in Nature Physics, (†: equally contributed)

[11] A. R Wildes, B. Fåk, U. B. Hansen, M. Enderle, J. R. Stewart, L. Testa, H. M. Rønnow, **Chaebin Kim**, and Je-Geun Park, “Spin wave spectra of single crystal $CoPS_3$”, Phys. Rev. B **107**, 054438 (2023)

[12] Pyeongjae Park, Woonghee Cho, **Chaebin Kim**, Yeochan An, Yoon-Gu Kang, Maxim Avdeev, Romain Sibille, Kazuki Iida, Ryoichi Kajimoto, Ki Hoon Lee, Woori Ju, En-Jin Cho, Han-Jin Noh, Myung Joon Han, Shang-Shun Zhang, Cristian D Batista, Je-Geun Park, “Tetrahedral triple-Q ordering in the metallic triangular lattice antiferromagnet $Co_{1/3}TaS_2$”, Under review in Nature Communications

국문초록

코발트 화합물에서의 스핀-궤도 얽힘 상태와 키타에프 상호작용에 관한 연구

김채빈
물리천문학부 물리학전공
서울대학교 대학원

응집 물질 물리학의 중요한 목표 중 하나는 양자 변동과 얽힘이 강하게 존재하는 양자 위상을 가진 새로운 물질을 발견하는 것입니다. 양자 스핀 액상 (QSL)은 자기 질서가 없고 스핀간 강한 얽힘이 존재하기 때문에 이러한 이국적인 양자 위상 중 하나라고 할 수 있습니다. 지금까지 제안된 많은 이론 모델 중에서 키타에프 모델은 아마도 실제 물질에서 양자 스핀 액상 상태를 구현할 수 있는 가장 가능성 높은 모델일 것입니다. 그 이유는 이 모델이 해석적으로 해를 구할 수 있으며 비교적 간단한 조건으로 실제 물질에서 재현 될 수 있음이 이론적으로 밝혀졌기 때문입니다.

실제 화합물에서 키타에프 모델을 구현하려면 스핀-궤도 얽힘 J_{eff} = 1/2 상태와 팔면체의 모서리 공유 결합이라는 두가지 성분이 필요합니다. 스핀과 궤도의 자유도의 얽힘은 스핀 간의 교환을 비등방적이고 결합 방향에 의존하게 만들 수 있습니다. 당연하게도, 키타에프 모델에 대한 현재까지의 연구는 강한 스핀-궤도 결합을 가지고 있는 4주기나 5주기 원소들에 대해서 진행되어 왔습니다. 하지만 4주기 및 5주기 원소 기반 화합물들에는 충분한 후보 물질이 부족하고 자성 상전이를 가지고 있는 한계점들이 존재했습니다.

따라서 실제 물질에서 키타에프 모델을 구현하기 위해서는 더 많은 후보들을 탐색해야 합니다. 최근 이론에 따르면 코발트와 같은 3주기 전이 금속에서도 작은 스핀-궤도 결합에도 불구하고 J_{eff} = 1/2 상태를 가질 수 있는 것이 알려졌습니다.

본 학위논문에서 저는 비탄성 중성자 산란 기법(INS)을 사용하여 벌집형과 삼각형의 두 가지 격자를 가진 코발트 키타에프 후보들의 스핀 동역학을 연구했습니다. 먼저, 저는 세 가지 코발트 벌집 화합물인 $CoPS_3$, $Na_2Co_2TeO_6$(NCTO) 및 $Na_3Co_2SbO_6$(NCSO)에서 스핀-궤도 얽힘 상태의 증거를 조사했습니다. 자기 여기의 온도 의존성을 통해 저는 $CoPS_3$에서 J_{eff} = 1/2 상태가 존재하지 않음을 확인했습니다. 그러나 스핀-궤도 얽힘 상태를 증명하는 스핀-궤도 들뜸은 다른 벌집 화합물 NCTO와 NCSO에서 관찰되었습니다. 스핀-궤도 얽힘 J_{eff} = 1/2 상태가 없다는 것은 $CoPS_3$가 간단한 스핀 S = 3/2 상태로 설명될 수 있고, 키타에프 상호작용와 같은 결합 의존적 이방성을 가질 수 없음을 나타냅니다. 이 관찰을 바탕으로 $CoPS_3$의 스핀파 스펙트럼은 단일 이온 이방성을 가진 XXZ 타입의 해밀토니안에 의해 분석되었습니다. XXZ 모델의 이방성 비율 J_x/J_z = 0.6일 때 관측된 스핀파를 잘 설명할 수 있었습니다.

NCTO와 NCSO의 경우, 스핀파 스펙트럼은 두 가지 다른 해밀토니안, XXZ 모델 및 일반화된 키타에프-하이젠버그 모델을 기반으로 분석되었습니다. 두 화합물의 스핀파 모두 강한 키타에프 상호 작용과 다른 비 키타에프 상호 작용에 의해 잘 설명되었습니다. 여기서 발견한 한 가지 중요한 특징은 키타에프 상호작용의 부호가 양수라는 것인데, 이는 현재의 키타에프 후보들과는 다른 부호입니다. 두 키타에프 후보를 종합적으로 검토하기 위해 추가적으로 자기 상전이 도표와 2-마그논 상태 밀도가 계산되었습니다.

둘째, 저는 키타에프 모델의 아이디어를 기하학적 쩔쩔맴을 주는 삼각

격자로 확장하여 연구를 진행하였습니다. 자기 반데르발스 코발트 삼각형 반강자석 CoI_2는 이러한 조건들을 충족하는 물질이였습니다. Luttinger-Tisza 방법을 사용하여 CoI_2의 자기 구조를 밝히기 위해 두 가지 최소 모델을 제시했습니다. 이 모델 중 하나는 키타에프 항을 포함하고 다른 모델은 이를 생략합니다. 자성 상전이 위의 온도에서 측정된 자기 들뜸을 통해 결합 의존적 이방성을 포함하는 최소 모델이 CoI_2의 특성을 설명한다는 것을 확인했습니다. 자성 상전이 상태에서 관찰된 스핀파 스펙트럼은 넓은 운동량 공간에서 상당한 선폭 넓어지는 것을 보여 마그논 붕괴를 시사했습니다. 이 붕괴 과정을 더 깊이 조사하기 위해 마그논-마그논 상호 작용에 대한 상태 밀도를 활용한 분석을 수행했습니다.

주요어: 양자 자성, 스핀-궤도 얽힘 상태, 키타에프 모델, 비탄성 중성자 산란, 마그논 붕괴

학 번: 2018-28059

Acknowledgement (감사의 글)

My journey to Ph. D degree was long and not an easy path. I must say that I could not have come this far without any helps from many people around the world. First of all, I would like to thank the guidance of my supervisor Prof. Je-Geun Park. He taught me how to survive in the scientific 'jungle' and how to define exciting questions to the condensed matter physics society. He always introduced many international collaborators when I was stuck in challenging problems. It helps me not only solve the problem but also improve my poor English skills and expand my scientific insights. I also deeply thank Prof. Cheol-Hwan Park, Sug-Bong Choe, and Hongki Min for kindly reviewing my dissertation and giving fruitful comments on my research. I especially appreciate my future boss Prof. Martin Mourigal for accepting an external review of my dissertation and guiding me to the new world of SUNNY code. I am fascinated to work with you at Georgia Tech.

I need to express my appreciation to our material and scattering team members. I learned a lot of ideas and skills from them, and we traveled together worldwide for experiments. For the material team, I would like to thank senior members Dr. Hwanbeom Cho, Dr. Soonmin Kang, and Dr. Seokhwan Yun. The X-ray experiment we had together was my first big facility experience and opened the exciting research of orbital physics. Without my experience in the material team, I could not make a solid basis for the Kitaev model and spin-orbit coupling physics. For the scattering team, I appreciate Dr. Jaehong Jeong for taking me to the world of neutron scattering and MATLAB. He taught me countless tips and how to draw beautiful graphs. I also thank my friend Dr. Pyeongjae Park for his thoughtful advice and helpful discussions. He always kindly listens to my silly questions and suggests many interesting ideas. Needless to say, I thank other team members Prof. Ki Hoon Lee, Dr. Kisoo Park, Dr. Taehun Kim, Heejun Yang, Yeochan Ahn, and

Woonghee Cho. I also would like to thank my intern students, Taehun Kim and Dongeun Kim.

My Ph. D. course could be completed by worldwide collaborators, who helped both experiment and theoretical works. First, I would like to thank many beamline scientists for helping me enter the neutron-scattering world. I appreciate Prof. Takatsugu Masuda, Prof. Shinichi Itoh, and Dr. Shinichiro Asai helping with my first inelastic neutron scattering experiment at the HRC beamline. I would like to thank Dr. Kenji Nakajima, Dr. Seiko Ohira-Kawamura, and Dr. Naoki Murai for helping with my neutron experiment in ARMATERAS during the painful pandemic situation. Without their dedicated support, I could not finish my experiment about CoI_2. I also appreciate Prof. Jie Ma, Prof. Haidong Zhou, and Dr. Gaoting Lin for working with NCTO and NCSO projects. I want to thank Prof. Heung-Sik Kim for his thoughtful discussions and DFT calculations. I also give my appreciation to Prof. Sasha Chernyshev and Dr. Pavel Maksimov for helpful discussions about Kitaev physics in the triangular lattice. I want to thank Prof. Sung-Jin Kim and Dr. Sujin Kim for helping me use the Bridgman furnace.

I will never forget our EPG members who helped me a lot during my Ph. D. course: Dr. Kaixuan Zhang, Dr. Matthew Coak, Dr. Suhan Son, Dr. Youjin Lee, Inho Hwang, Junghyun Kim, Gi Ung Park, Jingyuan Cui, Hyunchol Kim, Jihoon Keum, Sangwoo Sim, Taeyoun Kim, Ysun Choi, Hangoo Lee. I want to particularly thank Dr. Suhan Son for sharing his brilliant ideas and kindly answering my questions about van der Waals studies. I also deeply appreciate Nahyun Lee, Elika Beard, Youngeun Shin, Dr. Jaena Park, and Jiyoun Choi for their devotion to our group.

I also thank my Jay-Z family, Dr. Hyeongmin Cho, Dr. SeungJung Huh, Seongwook Shin, and MoonJong Kim. We have known each other for almost ten years, since from an undergraduate student. I could not finish this long journey without our

friendship. I would like to thank the rock band GAIA family for playing songs and guitar together. It helps me to release my stress during this journey.

마지막으로, 지금까지 이 길었던 학위기간 동안 한결같이 응원하시고 지원해주신 제 가족에게 깊은 감사의 말씀을 드립니다. 학부때부터 집에서 멀리 떨어져 공부하는 동안 항상 걱정하시고 응원해주신 어머니, 아버지, 그리고 서울에서 투닥거리지만 든든하게 옆에 있어준 동생 로빈이에게 감사합니다.